UNIVERSIDADE DE LISBOA
FACULDADE DE CIÊNCIAS
DEPARTAMENTO DE FÍSICA

‘Portable lab-on-chip platform for bovine mastitis diagnosis in raw milk’

Mestrado Integrado em Engenharia Biomédica e Biofísica
Perfil em Engenharia Clínica e Instrumentação Médica

Ana Rita Sintra Soares

Dissertação orientada por:
Professora Doutora Susana Isabel Pinheiro Cardoso de Freitas
Professor Doutor José António Soares Augusto

2015

Aos Álamos,

"Que a tua vida não seja uma vida estéril.

- Sê útil. - Deixa rasto." – JE

Resumo

As medidas de prevenção e controlo da mastite bovina consistem em boas práticas de gestão aliadas à administração de antibióticos. Os conceitos actuais para uma utilização prudente de antibióticos e preocupações a nível de saúde pública têm vindo a reforçar a necessidade de um diagnóstico adequado e atempado.

Geralmente, a mastite é detectada com base em sinais clínicos evidentes de condições anormais do leite e / ou do úbere das vacas ou por testes que indicam uma reacção inflamatória. O teste Califórnia Mastite, consiste na contagem de células somáticas e kits relativamente baratos de bio marcadores estão disponíveis para o efeito, mas estes apenas fornecem informações sobre a presença / ausência de inflamação.

Nos últimos anos, a tecnologia de Lab-on-Chip teve grandes desenvolvimentos, apresentando inúmeras vantagens relativamente aos métodos tradicionais de detecção de biomoléculas: maior sensibilidade, uma resposta mais rápida, recurso a pequenas quantidades de reagentes, redução do tamanho dos dispositivos, fácil utilização e custos acessíveis. Com o crescente interesse da medicina, indústria farmacêutica, biotecnologia e controlo ambiental, a tendência será deslocar os laboratórios para mais próximo dos clientes, através desta tecnologia também designada Point- of- Care (POC).

Paralelamente, a integração da tecnologia biológica em aplicações de engenharia alimentar tem tido particular interesse na última década. A identificação precoce dos agentes patogénicos causadores da mastite bovina tem uma grande importância para a implementação de medidas de controlo adequadas, reduzindo o risco de infecções crónicas e permitindo orientar a terapêutica antimicrobiana a ser prescrita. A rápida identificação dos agentes patogénicos, como *Staphylococcus spp.* e *Streptococcus spp.* e, entre estes, a discriminação entre os principais agentes contagiosos *Staphylococcus aureus* e *Streptococcus agalactiae*, irá contribuir para um decréscimo dos danos económicos e de saúde pública consequentes da mastite bovina.

Apesar dos sistemas de citometria convencional fornecerem resultados rápidos e fiáveis, estes continuam a ser volumosos, o que dificulta a sua portabilidade, além de apresentarem custos relativamente elevados e serem de utilização complexa. Por seu lado, os sensores magnetoresistivos são micro fabricados, podem ser integrados em canais microfluídicos e conseguem detectar células marcadas magneticamente.

Os sensores magnetoresistivos utilizados neste trabalho são designados por Spin-Valve, sendo constituídos por uma camada de metal não magnético entre duas camadas de metais magnéticos. Uma das camadas magnéticas apresenta uma magnetização fixa, devido a uma camada antiferromagnética adjacente que lhe fixa a magnetização, enquanto a magnetização da outra camada se encontra livre para rodar.

Esta dissertação pretende desenvolver uma plataforma portátil que integra um magnete permanente como fonte de magnetização, vinte e oito sensores magnetoresistivos e microfluídica, tornando possível a detecção e quantificação, de forma dinâmica e em tempo real, de partículas magnéticas e células marcadas magneticamente, utilizando vários sensores. Para tal, utilizou-se como ponto de partida um protótipo já existente no INESC-MN, que embora funcional, apresentava limitações na integração do biochip com a fonte de magnetização das nanopartículas, neste caso um magnete permanente.

Como as Spin-Valves são apenas sensíveis a uma direcção no plano, se bem alinhadas na zona de homogeneidade dos campos perpendiculares criados pelo magnete, este não afecta a sensibilidade dos sensores. No entanto, uma pequena inclinação do magnete pode criar componentes de campo magnético no plano do sensor e, por conseguinte, afectar a sua sensibilidade. O magnete utilizado neste trabalho tem dimensões 20x20x3mm^3 e um campo magnético residual de 1.2-1.3T.

O sistema de microfluídica é composto por quatro canais lineares e individuais com 50 µm de altura, 100 µm de largura e 1 cm de comprimento, alinhados com cada conjunto de sensores. O chip e os microcanais são montados face-a-face e selados através de um processo químico, sendo depois montados e soldados num circuito impresso.

Neste caso particular, o biossensor é desenhado para ser capaz de detectar e quantificar pequenas variações de campo magnético causadas pela presença de marcadores superparamagnéticos que são funcionalizados com anticorpos para proteínas de parede celular específicas que estão presentes na superfície das células de interesse.

As partículas superparamagnéticas são muito utilizadas neste tipo de aplicações pelo facto de, na ausência de campo magnético externo, apresentarem magnetização nula – estão num estado superparamagnético. Quando um campo magnético externo é aplicado, provoca a magnetização destas partículas conduzindo-as a um estado paramagnético. Uma partícula magnetizada verticalmente, ao fluir no microcanal, gera um campo variável sobre o sensor. Como resultado, um pico bipolar é a assinatura da passagem de uma partícula perpendicularmente magnetizada sobre o sensor.

De forma a conseguir obter uma plataforma com as características identificadas acima, foram combinados vários componentes numa única plataforma, através de um processo faseado que incluiu:

i) A microfabricação de sensores magnetoresistivos, através de técnicas de fotolitografia, etching e lift-off;
ii) A fabricação de um sistema de microfluidica em PDMS;
iii) A integração do chip com os microcanais de PDMS através de um processo de ligação químico;
iv) desenvolver um estudo sobre os efeitos de campos magnéticos externos sobre os sensores magnetoresistivos devido à presença de magnetes permanentes;
v) O desenvolvimento de um módulo com um sensor de efeito de hall, que integrado numa plataforma de scanning permitisse quantificar os campos perpendiculares e longitudinais de magnetes;
vi) a optimização do design do biochip de acordo com os dados obtidos;
vii) O desenvolvimento de uma plataforma de suporte para a combinação do biochip com o magnete permanente;
viii) A medição do momento magnético de um conjunto de partículas magnéticas com diferentes dimensões;
ix) A validação experimental da eficiência do magnete permanente na magnetização de nanopartículas magnéticas, através de ensaios experimentais de detecção de nanopartículas de diferentes dimensões.
x) O desenvolvimento de um programa de análise e contagem de eventos magnéticos utilizando o software Matlab®;
xi) A avaliação experimental da detecção de células marcadas com partículas magnéticas.

As medições experimentais foram realizadas utilizando uma plataforma electrónica desenvolvida pelo INESC-ID, há dois anos por um aluno de doutoramento, mostraram que a plataforma já optimizada permite a detecção de nanopartículas magnéticas e células marcadas magneticamente utilizando vários sensores magnetoresistivos, o que não era possível no protótipo anterior.

Cinco tipos de partículas magnéticas, com dimensões entre os 2800 nm e os 50 nm, foram testadas nos vários canais. Foram observados picos correspondentes à passagem de partículas magnéticas em todas as amostras, excepto para as partículas com dimensões de 80 nm e 50 nm. Face a estes resultados conclui-se que, provavelmente:

- Partículas de menores dimensões não apresentam tendência para formar aglomerados e, partículas individualizadas não têm momento magnético suficiente para serem detectadas;

- Ou que a magnetização das partículas pelo magnete permanente é demasiado pequena para induzir um momento magnético significativo nas mesmas.

Contudo, como neste caso é importante diminuir a probabilidade de ocorrência de falsos positivos, é relevante que partículas magnéticas que não estejam ligadas às moléculas de interesse não sejam detectadas pelo sensor. Deste modo, determinou-se que, para este sensor, as partículas de 80 nm ou 50 nm são as mais indicadas.

Para validação da detecção de células foram realizadas experiências usando amostras de leite com *Staphyloccocus* spp. cedidas por uma colega do INESC-MN que está a desenvolver o seu trabalho de doutoramento em plataformas portáteis para análises ao leite. Estes testes com amostras biológicas foram realizados no INESC-MN, utilizando culturas de bactérias e protocolos de funcionalização e marcação magnética previamente desenvolvidos no Centro de Investigação Interdisciplinar em Sanidade Animal (CIISA).

As células foram marcadas magneticamente com partículas de 50 nm funcionalizadas com o anticorpo monoclonal anti-*Staphyloccocus* spp. e introduzidas no biochip para os testes de aquisição. Nesta fase foram utilizadas amostras de 500 µL contendo 10000 ufc e 8 x 10^8 partículas magnéticas funcionalizadas. Foram detectados picos, o que indica a capacidade desta plataforma para a detecção magnética de células marcadas. Para além disso, com o programa de contagem foi possível quantificar o número de eventos magnéticos ocorridos, tendo sido detectados 6063, para um número de colónias de 10000.

Os resultados obtidos são bastante promissores, no entanto são necessários ainda estudos futuros para que este citómetro possa quantificar com maior precisão. Nomeadamente, um dos objectivos seria a medição realizada por vários sensores em simultâneo, de forma a obterem-se resultados mais confiáveis e precisos. Para tal, optimizações ao nível da aquisição do sinal, mais propriamente ao nível da plataforma electrónica de aquisição serão necessárias para que seja possível a medição com sensores em paralelo.

Palavras-chave: magnete permanente, sensores magnetoresistivos, microfluídica, partículas magnéticas, *Staphylococcus* spp..

Abstract

Over the past decade, the drawbacks of conventional flow cytometers have encouraged efforts in microfabrication technologies and advanced microfluidics systems.

Biosensor technology has been in exponentially development as it presents huge advantages when in comparison to traditional detection methods of biomolecules, such as high sensitivity, rapid response and small amount of reagents. Unlike external fluorescent/optical detectors, magnetoresistive (MR) sensors are micro-fabricated, can be integrated within microfluidic channels and can detect magnetically labelled biomolecules.

Bovine mastitis is an economic burden for dairy farmers and control measures to prevent mastitis are crucial for dairy company sustainability.

The present work describes a platform for dynamic mastitis diagnosis through detection of magnetically labelled cells with a magnetoresistive based cell cytometer, where a permanent magnet is used as magnetic source.

A study about the effects of the magnetic fields over the MR sensors was developed in order to be possible to design and engineer a platform integrating the permanent magnet with the chip in such a way that the magnetic fields did not affect the MR sensors behaviour.

Overall, assays were performed involving magnetic nanoparticles (MNP) and cells labelled with MNP. These assays were performed with a platform mentioned above, containing a permanent magnet assembled with the chip which was integrated with an electronic platform from INESC-ID, allowing signal acquisition from magnetized nanoparticles.

In a very preliminary stage, magnetic particles between 2800 nm and 50 nm were tested flowing through a 100 µm wide, 50 µm high microchannel, with speeds around 50 µL/min being detected. Bipolar and unipolar signals with average amplitude of 15 µV – ~250 µV were observed corresponding to magnetic events. A home-made program to count magnetic events was developed in Matlab®.

In particular it is presented an example for the validation of the platform as a magnetic counter that identifies and quantifies *Staphylococcus* spp. cells magnetically labelled with 50nm particles in a milk sample. In assays using 500 µL of milk sample, cells were detected with signal amplitude of 30 µV – ~200 µV.

Key-words: cytometers, magnetoresistive sensors, permanente magnet, magnetic nanoparticles, *Staphylococcus* spp..

Contents

Resumo V

Abstract IX

List of figures XIII

List of Tables XX

List of Acronyms XXI

Introduction 23

1.1 Objectives 24

1.2 Thesis Structure 24

1.3 State of the Art 25

Theoretical Background 31

2.1 Magnetic Dipoles 31

2.1.1 Magnetic Materials Properties 31

2.2 Giant Magneto-Resistance (GMR) and Spin Valve (SV) sensors 35

2.3 Biosensors 39

Materials and Methods 41

3.1 Spin Valve Chip Design 41

3.2 Microfabrication 42

3.3. Electrical Transport Characterization of SV sensors 48

3.4 Microfluidic system: PDMS channels and permanent bonding 50

3.5 Wirebonding and Encapsulation 51

3.6 Magnetic Labelling and detection 52

3.6.1 Magnetization Method 53

3.6.2 Detection Scheme 53

3.7 Characterization of Magnetic Nanoparticles 55

Biochip Platform 61

4.1 First Platform 61

4.1.1 Electrical Transport Characterization of SV sensors with the permanent magnet 62
4.2 Design and Development of the Second Platform 64
4.2.1 Electrical Transport Characterization of SV sensors with the permanent magnet 65
4.3 Development of a Magnetic Scanning Platform 66
4.3.1 Magnetic Scanning Analysis 69
4.3.2 Microfluidic Tests performed in the Platform with the permanent magnet 70
4.4 Second Spin Valve Chip Design 71
4.4.1 Chip Re-Design 71
4.4.1.1 Electrical Transport Characterization with the Permanent Magnet 72
Integration of the Biochip Platform with a portable electronic system 81
5.1 Electronic read-out of the sensors 81
5.2 Design and Development of the Third Platform 82
5.3. Experimental Results 83
5.3.1 Counting 84
5.3.2 Validation of micro-sized and nanometer-sized magnetic particles detection 86
5.3.3 Detection of Biomolecular Recognition 95
Conclusions and Future work 101
Bibliography 103
A. Run Sheet: Magnetic Counter 111
B. Run Sheet: PDMS Microchannels 123
C. Run Sheet: PDMS permanent bonding 124

List of figures

Figure 1.1 Schematic representation of mastitis development in an infected udder. Environmental and contagious microorganisms invade the udder through the teat cistern. They multiply in the udder where they are attacked by neutrophils while damaging the epithelial cells lining the alveoli, with subsequent release of enzymes and anti-microbial components. The immune effector cells begin to combat the invading pathogens [1]. 25

Figure 2.2 Representation of the magnetic moment associated with (a) an orbiting electron and (b) a spinning electron [5]. 31

Figure 2.3 Schematics of the gradual change in magnetic dipole orientation across a domain wall [5].....32

Figure 2.4 Schematic of the mutual alignment of atomic dipoles for a ferromagnetic material, which will exist even in the absence of an external magnetic field [5]. 33

Figure 2.5 Representation of antiparallel alignment of atomic dipoles for antiferromagnetic manganese oxide [5]. 33

Figure 2.6 Representation of domains in a ferromagnetic material. Arrows represent the atomic magnetic dipoles; the direction of alignment varies from one domain to another [5].....33

Figure 2.7 Exchange interaction between the antiferromagnetic and ferromagnetic layer. Top layer: Parallel alignment of the dipoles of the free pinned ferromagnetic layer. Bottom layer: Antiparallel alignment of the dipoles of the pinned ferromagnetic layer.....34

Figure 2.8 Ferromagnetic material divides itself into magnetic domains to reduce the demagnetizing field therefore reducing the magnetostatic energy. Figure adapted from [30] 35

Figure 2.9 Schematics of the SV sensor composed by a pinned layer and a free layer with parallel anisotropies [6].....35

Figure 2.10 Typical device structure: the two ferromagnetic layers separated by a nonmagnetic spacer. The arrows define the magnetization of each layer, upon the material acquires a shape. The antiferromagnetic layer (AFM) is introduced to fix the magnetization of the adjacent layer (pinned layer).....36

Figure 2.11 a) Magnetostatic coupling between magnetic layers; b) Dipolar coupling between layers [21]. 36

Figure 2.12 a) Transfer curve corresponding to parallel induced anisotropies, upon material deposition, showing that the magnetization reversal process along easy axis is predominantly domain wall motion; b) and c) Schematics of the effects of the material shape and dimensions in the crystalline anisotropy and shape anisotropy fields. The transfer curves show that the magnetization is a reversal process along the hard axis, which produces a coherent rotation of a domain wall motion. The PL crystalline anisotropy does not change his magnetization because it is fixed by AFM layer [6]. 37

Figure 2.13 MR transfer curve principle. R(H) linear behaviour and typical magnetization orientations correspondence. The yellow arrows represent the free layer magnetization rotation and the blue arrows represent the pinned layer magnetization. 38

Figure 2.14 Resistance vs. magnetic field transfer curve of a linear spin-valve at a given sense current. Red arrows represent magnetization direction of PL and the yellow ones represent the magnetization direction of the FL. 39

Figure 3.15 Design detailed of the biochip mask in AutoCad®: chip array of 28 SVs in red displayed vertically in the centre of the chip, the contact leads are presented in blue lines and the frame for electrical contact at the end of each contact leads displayed in green lines. 41

Figure 3.16 Schematics of one SV structure used in my thesis. 42

Figure 3.17 (A) SVG autonomous coating and development tracks system; (B) Direct Write Laser (DWL) system for lithography exposures; (C) AutoCad® Mask for first lithography: sensor's definition. Chip with array of 28 SVs in red displayed vertically in the centre of the chip. 43

Figure 3.18 Ion beam system configured for the ion milling and O_2 bonding mode. In this configuration only the assist gun is activated in order to etch the substrate surface. 44

Figure 3.19 Etching process: a) Patterning of the PR by photolithography b) Etching of the non-protected thin film layer c) sample after etch and resist strip. 44

Figure3.20 AutoCad® mask for second lithography: contact leads definition. The contact leads are presented in blue. 44

Figure 3.21 Thin film deposition process. 45

Figure 3.22 Photoresist and metal lift-off in wet bench. 45

Figure 3.23 Optical verification of Si_3N_4 deposition: passivation layer. 45

Figure 3.24 Design AutoCad® of the chip with the SV displayed in red. The frame for electrical contact at the end of each contact lead is displayed in green. 46

Figure 3.25 Reactive ion etching for pads opening. a) Visual and b) microscopic verification of defined SV, vias and contacts. 46

Figure 3.26 Sample was cut into individual dies. 46

Figure 3.27 a) Resist stripping; b) Microscope observation. 47

Figure 3.28 Annealing of each individualized chips. 47

Figure 3.29 a) Transport Characterization setup; b) Schematic diagram of the setup employed for the electrical characterization. 48

Figure 3.30 Electrical Transport Characterization, MR curve of the Spin valve. 49

Figure 3.31 Top view of the microchannels in the AutoCad® mask and assembled mold and PMMA plates for PDMS casting. 50

Figure 3.32 Microscopic picture of the PDMS microchannel aligned with sensors on the chip. 50

Figure 3.33 UV-O Cleaner system and a picture of the microchannel bonding with biochip. 51

Figure 3.34 a) Wire bonding machine; b) Microscope picture of the connections between sensors contacts and the copper contacts of the PCB; c) PCB with mounted and bonded biochip. 51

Figure 3.35 superparamagnetic particles behaviour in the presence and absence to an external magnetic field. 52

Figure 3.36 Schematics of MR sensor detection of magnetically labeled targets flowing above the sensor for perpendicular magnetzation A [10] and B [4]; Perpendicular magnetization gives origin to an average field with a bipolar configuration C. 54

Figure 3.37 Picture of the VSM system used at INESC-MN and schematic illustration of the pick up coils and quartz rod. ...56

Figure 3.38 Magnetic properties of magnetic beads, measured by VSM. a) Magnetic moment per 50nm particle. b) Magnetic moment per 2800nm particles. 56

Figure 3.39 Simulation of the average of the magnetic field sensed by the sensor relative to position of the MNP over distance from the sensor. a) Magnetic field along x-direction of a 50nm particle at height z=1 and z=10; b) Magnetic field along x-direction of a 2800nm particle at height=1 and 10; c) Magnetic field along x-direction of a 50nm particle at different heights. These simulations were permormed using the MAPLESOFT 12 software. 58

Figure 3.40 Detection schematics (not to scale) of a magnetically particle, parallel magnetized, flowing over a SV sensor. The graphic represents an example of a simulated signal for 5 μm diameter cells, labelled with N= 2880 nanoparticles, parallel magnetized, at different heights [3, 7, 10] μm l. Adapted from [10]. 58

Figure 4.41 Detailed design of the biochip mask in AutoCad®: chip array of 28 SVs is displayed in red, vertically in the centre of the chip, the contact leads are presented in blue lines and the frame for electrical contact at the end of each contact leads displayed in green lines. 61

Figure 4.42 a) Assembly of the Biochip with the magnet, that is glue on the PCB; b) Schematics of the platform, showing the thicknesses of the different components of the platform. 61

Figure 4.43 MR curve of the SV a) without a permanent magnet below; b) assembled with the permanent magnet. 62

Figure 4.44 Schematics of the impact of the sensor response of each magnetic field component, set by magnet position transfer curves [4].....63

Figure 4.45 Schematics of the free and pinned layer magnetizations in the absence of a magnetic field. 63

Figure 4.46 a) AutoCad® design of the support platform; b) Schematics of the full assembled integrated platform; c) Fotography of the full assembled integrated platform with the biochip and the squared permanent magnet. 64

Figure 4.47 MR curve of the SV a) without a permanent magnet below; b) assembled with the permanent magnet at 0,5 cm distance; c) assembled with the permanent magnet at 1 cm distance; d) assembled with the permanent magnet at 2 cm distance. 65

Figure 4.48 Magnetic scanning platform. 66

Figure 4.49 Schematics of an Hall Effect sensor principle [16]. 67

Figure 4.50 Use of an Hall Effect sensor for permanent magnet measurement of: perpendicular and in-plane magnetic fields. The sensor passes above the permanent magnet and their lines of force act on the chip. 68

Figure 4.51 Schematics of the measurements of the permanent magnet. 68

Figure 4.52 LabView softawe developed for the permanent magnet scanning masurements..... 69

Figure 4.53 Perpendicular (a), b), c)) and Longitudinal (d), e), f)) magnetic field scan results from the surface of the permanent magnet at different heights from the sensor. The resolution used in the scanning was 0.25 mm, so the dimensions of the magnet are showen in the graphics multiplicated to 0.25. 69

Figure 4.54 a) Dynabeads® M-280; Photography of: b) experimental setup; c) a section of the microchannel where a sample that contains water, magnetic particles and blue dye can be observed under a microscope using a magnification of 20x. 71

Figure 4.55 Top view of the biochip in the AutoCad® mask (A); Four arrays of spin valve sensors (B); One group of spin valve sensors (C). 72

Figure 4.56 MR curve of the SVs a) without a permanent magnet below; b) assembled with the permanent magnet at 1 cm distance; c) assembled with the permanent magnet at 2 cm distance. 72

Figure 4.57 Representation of the impact of positioning of magnet in sensors transfer curve parameters: A. Magnetoresistivity; B. Effective coupling field; C. Coercive field. 75

Figure 4.58 Schematics of a non perpendicular orientation between the F layer and P layer, which promote discontinuities in sensor magnetic response to an external magnetic field. F: Free; P: Pinned (P). 75

Figure 4.59 Schematics of the linearization of the sensor due to the presence of the permanent magnet. F: Free; P: Pinned (P). 76

Figure 4.60 (A) AutoCAD® design of the chip; (B) Array of SVs is zoomed showing the location of SVs number 15 and 23, refered below. 76

Figure 4.61 Tranfer curves of SV number 15 and 23 obtained when: a) there is no permanent magnet below; b) a permanent magnet is placed at 1 cm from the SVs; c) a permanent magnet is placed at 2cm below the SVs. The graphics show the influences on the tranfer curves caused by the permnent magnet presence below the sensors. 77

Figure 4.62 Tranfer curves of four SVs, localized in each one of microchanels, obtained when: a) there is no permanent magnet below; b) a permanent magnet is placed at 1 cm from the SVs; c) a permanent magnet is placed at 2cm below the SVs. The graphics show the influences on the tranfer curves caused by the permanent magnet presence below the sensors. 78

Figure 5.63 Setup used in the experiments: 1) Biochip platform; 2) batteries for power supply and portability; 3) acquisition board, which encrypts the data collected from sensors; 4) Digital to analogue converter (DAC), it is responsible for the data conversion and transition to the device for user interface (computer); 5) Syringe pump to impose flowrates; 6) User interface (computer)..... 81

Figure 5.64 AutoCad® PCB design. 82

Figure 5.65 Assembly of the platform with the SV chip and permanent magnet to PCBs and data acquisition electronic platform. 83

Figure 5.66 Acquisition setup assembly. 83

Figure 5.67 Statistical analysis of the noise measured from a sample containing non-magnetic material. The standard deviation is ~ 3.86 μV and for counting calculations (in this case) was considered to be between ± 4σ. So, in this case, the threshold should be 4 x (±3.86 x10^{-06}) = ± 1.54x10^{-05} V. 85

Figure 5.68 Example of data acquired (10^4 points) by one sensor when a buffer with magnetic particles flow inside the microchannel. The counting peaks software counts just the peaks above the threshold defined by the noise to the noise background. 85

Figure 5.69 Data acquired by the SV 7: a) No sample inside the microchannel; b) When a buffer pass through the microchannel, corresponding to the noise background. 86

Figure 5.70 Statistical analysis of the noise measured from a sample containing non-magnetic material. The standard deviation is ~ 8 μV and for counting calculations (in this case – SV 7) was considered to be between ± 5σ. The threshold should be 5 x (±8.02 x10^{-06}) = ± 4.05x10^{-05} V. 87

Figure 5.71 Representative figure of three single peak detection response of one sensor to one trial of 30 second run of the sample M-280 Streptavidin magnetic particles. The peak amplitude values are displayed in μV. 87

Figure 5.72 Number of peaks counted and their amplitude. 88

Figure 5.73 Data acquired by the SV 3: a) No sample inside the microchannel; b) When a buffer passes through the microchannel, corresponding to the noise background. 88

Figure 5.74 Statistical analysis of the noise measured from a sample containing non-magnetic material. The standard deviation is ~ 2 μV and for counting calculations (in this case – SV 3) was considered to be between ± 5σ. The threshold should be 5 x (±2.26 x10^{-06}) = ± 1.13x10^{-05} V. 89

Figure 5.75 Representative figure of two single peak detection response of SV 3 to one trial of 30 second run of the sample 250nm magnetic particles. The peak amplitude values are displayed in μV. 89

Figure 5.76 Number of peaks counted and their amplitude. 90

Figure 5.77 Data acquired by the SV 10: a) No sample inside the microchannel; b) When a buffer flow through the microchannel, corresponding to the noise background. 90

Figure 5.78 Statistical analysis of the noise measured from a sample containing non-magnetic material. The standard deviation is ~ 2 μV and for counting calculations (in this case – SV 10) was considered to be between ± 4σ. The threshold should be 4 x (±3.86 x10^{-06}) = ± 1.54x10^{-05} V. 91

Figure 5.79 Representative figure of peak detection response of one sensor to one trial of 30 second run of the sample 130 nm magnetic particles. A zoom is applied to four single peaks. The peak amplitude values are displayed in μV. 91

Figure 5.80 Number of counted peaks and their amplitude. 92

Figure 5.81 Data acquired by the SV 12: a) No sample inside the microchannel; b) When a buffer flow through the microchannel, corresponding to the noise background. 92

Figure 5.82 Statistical analysis of the noise measured from a sample containing non-magnetic material. The standard deviation is ~ 0.5 μV and for counting calculations (in this case – SV 12) was considered to be between ± 4σ. The threshold should be 4 x (±3.86 $x10^{-06}$) = ± 1.54$x10^{-05}$ V. 92

Figure 5.83 Representative figure of non-peak detection response of one sensor to one trial of the sample 80 nm magnetic particles. A zoom of the date showed that values are above the defined threshold. 93

Figure 5.84 Data acquired by the SV 8: a) No sample inside the microchannel; b) When a buffer flow through the microchannel, corresponding to the noise background. 93

Figure 5.85 Statistical analysis of the noise measured from a sample containing non-magnetic material. The standard deviation is ~ 0.3 μV and for counting calculations (in this case – SV 8) was considered to be between ± 4σ. The threshold should be 4 x (±3.86 $x10^{-06}$) = ± 1.54$x10^{-05}$ V..... 94

Figure 5.86 Representative figure of non-peak detection response of one sensor to one trial of 30 second run of the sample 50 nm magnetic particles..... 94

Figure 87 Schematics of immuno-magnetic functionalization of cells. a) 50 nm Superparamagnetic particle; b) Protein A; c) anti-staphylococci spp. monoclonal antibody; d) Staphylococcus Cell; e) Staphylococci immunogenic protein. 95

Figure 5.88 Acquired signal: a) sensor base noise level ; b) raw milk blank sample; c) raw milk with functionalized nanoparticles (control sample). 96

Figure 5.89 Statistical analysis of the noise measured from a sample containing non-magnetic material. The standard deviation is ~13 μV and for counting calculations (in this case – SV 4) was considered to be between ± 6σ. The threshold should be 6 x (±5.16 $x10^{-06}$) = ± 3.1$x10^{-05}$ V..... 97

Figure 5.90 Raw milk sample with Staphylococcus cells. The peak amplitude values are displayed in μV. 98

Figure 5.91 Number of peak counts of the sample measured and the amplitude. 98

Figure A92 Spin Valve layers. 111

Figure A93 Overall Process of the third step. 112

Figure A94 AutoCad® Mask for first lithography: sensor's definition. Chip with array of 28 SVs in red displayed vertically in the centre of the chip. 113

Figure A95 Schematics of physical etching. 114

Figure A96 Schematics of resist stripping. 115

Figure A97 Second lithography process. 115

Figure A98 AutoCad® mask for second lithography: contact leads definition. The contact leads are presented in blue. 116

Figure A99 Schematics of Thin film deposition process. 118

Figure A100 Photoresist and metal litf-off process. 118

Figure A101 Schematics of Si_3N_4 deposition: passivation layer. 119

Figure A102 Third lithography process. 119

Figure A103 Design AutoCad® of the chip with the SV displayed in red. The frame for electrical contact at the end of each contact lead is displayed in green. 120

Figure A104 Schematics of reactive ion etching for pads opening. 121

Figure A105 Sample was cut into individual dies. 122

Figure A106 Resist stripping. 122

List of Tables

Table 1.1 Diagnostic overview of bovine mastitis [1, 2]. 27

Table 3.2 Simulations of the average magnetic field sensed by the sensor relative to position of the MNP at a certain height (z). 57

Table 3.3 Simulations of the voltage output measured by the sensor relative to position of the MNP at a certain height (z). 57

Table 4.4 Important parameters taken from SVs transport characterization 65

Table 4.5 Important parameters taken from the MR curve of the SVs without a permanent magnet below. 73

Table 4.6 Important parameters taken the MR curve of the SVs with a permanent magnet below at 1 cm. 73

Table 4.7 Important parameters taken the MR curve of the SVs with a permanent magnet below at 2 cm. 73

Table 4.8 Values obtain from the equation above, showing the impact of the contribution of the permanent magnet field components in saturation field sensors transfer curve. 77

Table 4.9 Values obtained from the equation above, showing the impact of the positioning of the magnet below the sensors due to the contribution of the permanent magnet field components in saturation field sensors transfer curve. 79

Table 5.10 Statistical analysis of the noise measured from a sample containing non-magnetic material. 85

Table 5.11 Statistical parameters of the SV 7 signal without sample flowing inside 87

Table 5.12 Statistical parameters of the SV 3 signal without sample flowing inside 89

Table 5.13 Statistical parameters of the SV 10 signal without sample 91

Table 5.14 Statistical parameters of the SV 12 signal without sample flowing 93

Table 5.15 Statistical parameters of the SV 8 signal without sample 94

Table 5.16 Statistical parameters of the SV 4 signal without sample flowing inside microchannel, from a milk sample, milk sample with functionalized MNPs and a milk sample with bacteria's labelled with functionalized MNPs. 97

List of Acronyms

Ab	Antibody
AFM	Antiferromagnetic
CIISA	Centro de Investigação Interdisciplinar em Sanidade Animal
DC	Direct Current
DWL	Direct Write Laser
ELISA	Enzyme-Linked Immunoabsorbent Asay
FL	Free Layer
FM	Ferromagnetic
GMR	Giant Magnetoresistance
GPIB	General Purpose Interface Bus
IBD	Ion Beam Deposition
IBM	International Business Machines Corporation
INESC-MN	Instituto de Engenharia de Sistemas e Computadores – Microsistemas e Nanotecnologias
INESC-ID	Instituto de Engenharia de Sistemas e Computadores – Investigação e Desenvolvimento
MNPs	Magnetic Nanoparticles
MR	Magnetoresistance
PBS	Phosphate Buffer Saline
PCB	Printed Circuit Board
PDMS	Poly(dimethylsiloxane)
PECVD	Plasma Enhanced Chemical Vapour Deposition
PL	Pinned Layer
PMMA	Poly-methyl-methacrylate
POC	Point-of-Care
PR	Photoresist
SCCs	Somatic cell counts
SV	Spin Valve
UHV II	Ultra-High Vacuum II
UV - O	Ultraviolet and Ozone
VSM	Vibrating Sample Magnetometer

Chapter 1

Introduction

Regarding milk production, bovine mastitis continues to be an economically important disease being difficult to estimate the losses associated with clinical mastitis, which arises from the costs of treatment, culling, death and decreased milk production.

Beside financial implications of mastitis, the importance of this disease in public health should not be overlooked. The extensive use of antibiotics in its treatment and control has possible implications for human health through the increased risk of antibiotic resistance strains of emerging bacteria that may then enter in the food chain.

Diagnostic methods have been developed to check the quality of the milk through detection of mammary gland inflammation and diagnosis of the infection and its pathogens, but these methods have their limitations and there is a need of new, rapid, sensitive and reliable assays.

Since 2000, INESC-MN has pioneered research and development on spintronic based lab on chip platforms for biomolecular recognition events. These are recognized by integrated spintronics transducers: Spin Valves or Magnetic Tunnel Junctions.

At INESC-MN, Point-of-Care platforms have already been designed, fabricated and tested for: DNA based assays (gene expression chips-CF mutation detection), proteins and cell assays (*Salmonella*, *E. coli*) and lateral immune assays (antibiotics in meat). The control electronics acquisition setup was also developed leading to two prototypes: one for static biomolecular recognition, where probes are immobilized over sensor sited and the signal is recorded as labelled targets hybridized with the probes, and another that is a dynamic cell counter for labelled cells as they pass over sensors, while flowing inside microfluidic channels.

This thesis focuses on an optimization of the dynamic cell counter prototype for the identification and quantification of bacteria, *Staphylococci.*

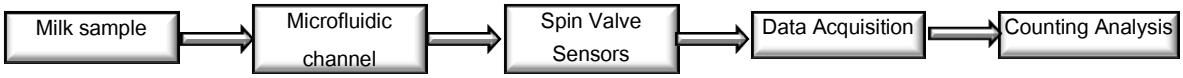

Hopefully, this device will contribute as an integrated part of a magnetoresistive Point-of-Care system, serving as an efficient tool.

1.1 Objectives

The present work follows the research done at INESC-MN on a biosensor system based on antibody recognition of mastitis pathogen, which uses a permanent magnet as magnetization source. This avoids the need of an external power source, enabling a more compact device and portable tests, which provides additional flexibility on their employment and also lowers the production costs of tests.

The detection scheme used in this platform relies on magnetoresistive (MR) sensor's sensitivity to count cells in flow, detecting bacterial cell events as these pass over the sensor. However, the external permanent magnet, which is placed below the sensor, creates a strong field gradient that causes changes in sensor's behaviour and also magnetic nanoparticles agglomeration at microchannels. A more homogeneous magnetic field needs to be implemented in order to minimize this effect.

The main goal of this thesis relies on the optimization of the integration of the chip that contains an array of sensors, with a permanent magnet, making possible to have more than one sensor functional to be used in measurements of four different samples simultaneously. In this way, this thesis supports a device capable of performing the counts of bacteria cells in an accurate, quantitative, easy and fast way.

To achieve these objectives there are some main tasks:

I. Fabrication of Spin Valve (SV) sensors and their assembly with a microfluidic module.

II. Biosensor system optimizations to allow the use of a permanent magnet as magnetization source without affecting the sensors, in order to be possible to use more than one sensor measuring at the same time.

III. Connection of the biosensor to an acquisition setup.

IV. Validation of the assembled device's ability to detect different magnetic particles and, further on, magnetically labelled bacteria.

1.2 Thesis Structure

This thesis is organized as explained below.

After a brief introduction that includes a state of the art on systems for mastitis detection, chapter 2 includes a theoretical background. Chapter 3 is focused on the material and methods for the fabrication of the biochip, its assembly in the platform and the description of microfluidic system.

The experimental chapters are then divided into chapter 4 that comprises the integration of the biochip with permanent magnets, results and respective conclusions and chapter 5 which contains the integration of the

biochip platform, developed and fabricated (Chapter 3) at INESC-MN, with a portable electronic system developed in association with INESC-ID, assessing the detection of magnetic particles and cells in a Biochip.

Finally, chapter 6 closes the project with general conclusions and future perspectives.

1.3 State of the Art

Bovine mastitis (*mast* = breast; *it is* = inflammation) is defined as an inflammation of the mammary gland. Organisms as diverse as bacteria, mycoplasmas, yeasts and algae have been implicated as causes of the disease. Fortunately, the vast majority of mastitis is of bacterial origin, being related with only five species of bacteria: *Echerichia coli*, *Streptococcus uberis, Staphylococcus aureus, Streptococcus agalactiae* and *Streptococcus dysgalactiae*.

The potential spread of zoonotic organisms via milk, though it is rare in the era of pasteurisation, remains a risk especially in the niche markets of unpasteurised dairy products and during pasteurisation failures.

The traditional concept of environmental mastitis is that organisms live in the environment and contaminate the teats.

Invasion of the udder is considered to occur when the teat orifice is open. Usually, the teat canal is tightly closed by sphincter muscles, preventing the entrance of pathogens. However, when fluid accumulates within the mammary gland as parturition approaches, it results in an increased intramammary pressure and mammary gland becomes vulnerable due to dilatation of the teat canal leakage of mammary secretions. In addition, during the milking there is a distention of the teat canal and the sphincter requires ~2h to return back to the constricted position, Figure 1.1, [1].

Following rapid bacteria multiplication in the milk, an inflammatory response is mounted. The severity of the disease is then thought to be influenced in part by the speed of the immune response, in particular polymorphonuclear cell migration into the udder.

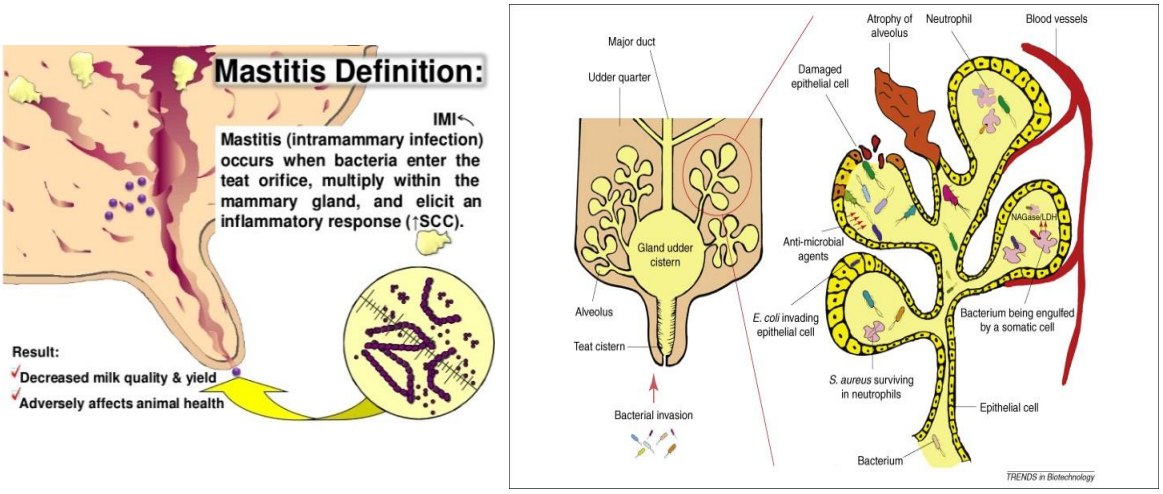

Figure 1.1 Schematic representation of mastitis development in an infected udder. Environmental and contagious microorganisms invade the udder through the teat cistern. They multiply in the udder where they are attacked by neutrophils while damaging the epithelial cells lining the alveoli, with subsequent release of enzymes and anti-microbial components. The immune effector cells begin to combat the invading pathogens [1].

Early diagnosis is of the utmost importance due to the high costs of mastitis. Currently, milk quality payments are based on somatic cell counts (SCCs), and elevated levels result in reduced payments [1].

In Europe, elevated SCCs above 200 000 cells/mL are widely used as an indicator of mastitis and are determined using haemocytometers or cell counters [1]. Measurements of SCC lower than 1×10^3 cells/mL indicates normal milk while during the infection it can rise to above 1×10^6 cells/mL [2].

Currently measurement of SCCs and alternative methods for detection of mastitis have been developed such as:

Table 1.1 Diagnostic overview of bovine mastitis [1, 2].

		Advantages	Disadvantages
California Mastitis Test (CMT)	Simple cow-side indicator test for subclinical mastitis by somatic cell count estimation of milk. The measurement in milk samples uses a test reagent which reacts with the DNA in those cells, forming a gel. The viscosity achieved by the aggregation of nucleic acids is proportional to the leukocyte number.	- Cost effective - Rapid - User friendly - Portable	- Results are difficult to interpret - Low sensitivity
Portacheck	This method uses an esterase-catalysed enzymatic reaction to determine the SCC in milk.	- Cost effective - Rapid - User friendly	- Low sensitivity at low SCCs
Fossomatic SCC	Fluorometric assay that uses ethidium bromide that penetrates and intercalate with the nuclear DNA and a fluorescent signal is generated and used to estimate the SCC in milk.	- Rapid	- Expensive - Complex to use
Delaval Cell Counter	This counter operates on the principle of optical fluorescence, where propidium iodide is used to stain nuclear DNA to estimate the SCC in milk.	- Rapid - Portable	- Expensive
R-mastitest (Electrical conductivity test)	This is an indirect test for cow's mastitis diagnosis and as it measures the increase in conductance in milk caused by the elevation in levels of ions during inflammation.	- Portable	- Non-mastitis related variations in Electrical conductivity can present problems in diagnosis.
pH test	Colorimetric assay. The rise in milk pH, due to mastitis, is detected using bromothymol blue	- Cost effective - Rapid - User friendly	- Low sensitivity

***In vitro* culture based diagnosis**	Milk samples can be taken for bacterial, viral and fungal culture in a specific media and further microbiological/biochemical tests are used to identify different microorganisms involved in mastitis cause.	-	Identifies specific pathogens causing mastitis	-	A laboratory is needed to perform the tests - Time consuming - Culture is capable of detecting only viable cells
PCR based diagnosis	Multiplex PCR: can identify multiple pathogens in a single reaction at the same time. Real time PCR: Circulating miRNA:	-	PCR based detection from mastitis milk samples are less time consuming - PCR assay is based on DNA and thus no matter of live or dead organisms	-	A laboratory is needed to perform the tests - PCR detects lower number of organisms - Costly instruments and consumables
Immune assay	ELISA: enzyme-linked immunosorbent assay is a test that uses antibodies and colour change to identify a substance.	-	Rapid - Antigens of very low or unknown concentration can be detected	-	A laboratory is needed to perform the tests - Only monoclonal antibodies can be used as matched pairs - Negative controls may indicate positive results if blocking solution is ineffective.
Proteomics based detection	Proteomic tools as two-dimensional gel electrophoresis and mass spectroscopy helped to identify various proteins expressed during mastitis.	-	It is the only technique that can be routinely applied for parallel quantitative expression profiling of complex protein mixtures such as whole cell and tissue lysates - It is the most widely used method for efficiently separating proteins, their variants and modifications	-	the complexity of biological structures and physiological processes - Proteins expressed at low abundance may be missed -
Biosensors	Biological sensors which use bio-receptors like antibody, nucleic acid, enzymes, and produce a signal after combination with transducers.	-	Rapid - Portable - User friendly - Cost effective	-	Results are difficult to interpret - Low sensitivity

At present, control of the disease is centred on reducing environmental challenges around parturition and during lactation and ensuring strict hygiene both at and after milking. The biggest challenge facing the modern industries is the pressure to reduce the use of antibiotics in food producing animals, coupled with the dramatic increase in organic milk production in recent years [3].

For the past three decades, advances in sample pre-treatment, flow handling, precision technologies and bioinformatics have allowed the introduction of some sophisticated analytical tools in the cell/molecular biology areas, industrial bioprocesses, disease diagnostics, and so many other fields. In addition to detection and enumeration, some flow cytometers have the ability to sort cells at high speeds based on detected signals.

Over the past years, the drawbacks of conventional flow cytometers have triggered efforts to take advantages of microfabrication and microfluidics technologies to achieve smaller, simple, low-cost instrumentation and enhanced portability for in-situ measurements.

The Lab-on-Chip approach has been making use of inexpensive polymers and detection techniques integrated with electronics, for example optical fibres, diode lasers, electrodes and magnetoresistive sensors. Some platforms present a static detection, where labels complementary to the target are immobilized on the sensors surface. However these platforms are limited by the sensors surface area and number of immobilized labels/targets.

This project addresses the optimization of permanent magnet integration on a biochip, which comprises MR sensors and microfluidics, as magnetic source for magnetic nanoparticles that flow inside microchannels. The ultimate goal is the to detect and count *Staphylococci* and *Streptococci* cells in milk samples in collaboration with a colleague at INESC-MN doing a PhD on veterinary and portable platforms for milk analysis.

Chapter 2

Theoretical Background

Magnetism is the phenomenon by which material assert an attractive or repulsive force or influence on other materials.

Iron, some steels and the mineral iodestone are examples of materials that exhibit magnetic properties. However all substances are influenced by the presence of a magnetic field.

2.1 Magnetic Dipoles

Magnetic forces are generated by moving electrically charged particles. Imaginary lines of force may be draw to indicate the direction of the force at positions in the vicinity of the field source.

Magnetic dipoles are found to exist in magnetic materials and can be compared to electric dipoles. Magnetic dipoles may be seen as small bar magnets composed of north and south poles instead of positive and negative electric charges. These dipoles are influenced by the magnetic field in a manner similar to the way in which electric dipoles are affected by electric fields.

2.1.1 Magnetic Materials Properties

Macroscopic magnetic properties of materials are a consequence of magnetic moments associated with individual electrons. Each electron in an atom has magnetic moments being originated from two sources:

I. Related to its orbital motion around the nucleus. An electron being a moving charge may be considered to be a small current loop that generates a very small magnetic field and has a magnetic moment along its axis of rotation, Figure 2.2a).
II. Related to its spinning movement around an axis. Spin magnetic moments may only be in an up direction or down direction, and thus each electron in an atom may be perceived as a small magnet having permanent orbital and spin magnetic moments, Figure 2.2b).

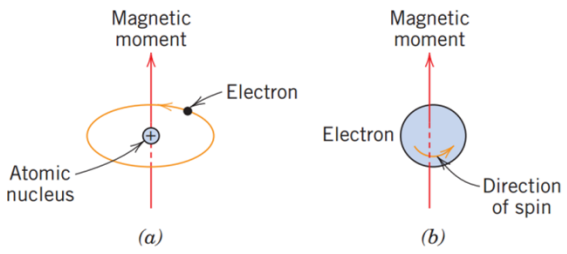

Figure 2.2 Representation of the magnetic moment associated with (a) an orbiting electron and (b) a spinning electron [5].

In each individual atom, orbital moments of some electron pairs cancel each other. The net magnetic moment for an atom is just the sum of the magnetic moments (both orbital and spin contributions) of each of the constituent electrons.

For an atom which has completely filled electron shells or subshells, when all electrons are considered, there is a total cancellation of both orbital and spin moments. Thus, materials composed by atoms with completely filled electron shells are not capable of being permanently magnetized, such as the inert gases and some ionic materials.

All materials exhibit some type of magnetism, whose behaviour depends on the response of electron and atomic magnetic dipoles to the application of an external applied magnetic field. According to their magnetic properties, the materials can be classified into five distinct groups: diamagnetic materials, paramagnetic materials, ferromagnetic materials, antiferromagnetic materials and ferrimagnetic materials.

In this study it was used some of these materials, which are described below:

Paramagnetic material

The atoms of paramagnetic materials have a permanent magnet moment in absence of a magnetic field, due to the unpaired electrons on their partially filled shell, Figure 2.3. Since these atoms, as magnetic dipoles, poorly interact with each other they get random orientation due to thermal agitation. In the presence of an external magnetic field, the moments increasingly align with the field as the intensity of the field increases. Paramagnetic materials have positive and small susceptibility [5].

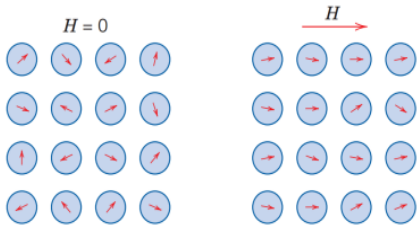

Figure 2.3 Schematics of the gradual change in magnetic dipole orientation across a domain wall [5].

Ferromagnetic material

This material exhibits a large permanent magnetization even when a magnetic field is not present. The atoms of ferromagnetic materials have unpaired electrons, so the electron spins are not cancelled. Furthermore, coupling interactions cause spin magnetic moments of adjacent atoms to align with one another. When a magnetic field rises the individual moments tend to align with the field, Figure 2.4. The saturation magnetization (Ms) is achieved when all the magnetic dipoles are mutually align with the external field. Ferromagnetic materials have positive and large susceptibility [5].

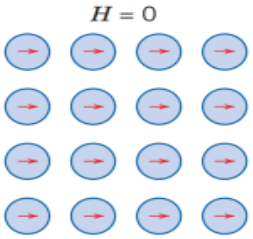

Figure 2.4 Schematic of the mutual alignment of atomic dipoles for a ferromagnetic material, which will exist even in the absence of an external magnetic field [5].

Antiferromagnetic material

In antiferromagnetic materials, the interaction between their atoms results in individual magnetic moments with antiparallel alignment, Figure 2.5. Manganese oxide (MnO) is an example of such material, having Mn^{2+} and O^{2-} ions. No net magnetic moment is associated with O^{2-}, since there is a total cancelation of both spin and orbital moments. However, Mn^{2+} ions have a net magnetic moment that is predominantly of spin origin and they are arrayed in the crystal structure such that the moments of adjacent ions are antiparallel. Since the opposing moments cancel one another with equal magnetic magnitude, the net magnetic moment in the absence of magnetic field is zero [5]. Antiferromagnetic materials have positive and small susceptibility.

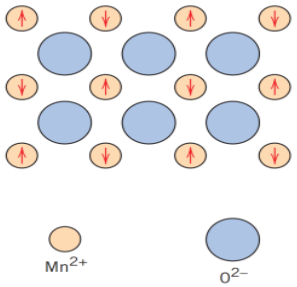

Figure 2.5 Representation of antiparallel alignment of atomic dipoles for antiferromagnetic manganese oxide [5].

Exchange energy

Any ferromagnetic or ferrimagnetic material is composed of small volume regions in which there are mutual alignments of all magnetic dipole moments in the same direction, Figure 2.6. Such region is called a domain, and each domain is magnetized to its saturation magnetization.

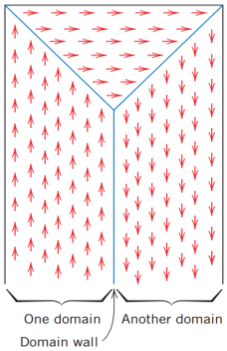

Figure 2.6 Representation of domains in a ferromagnetic material. Arrows represent the atomic magnetic dipoles; the direction of alignment varies from one domain to another [5].

According to the theoretical model of atomic dipoles for ferromagnets, each permanent dipole interacts strongly with its nearest dipoles.

Dipoles are aligned in a parallel or antiparallel way depending if the material is ferromagnetic or antiferromagnetic, respectively. Exchange interaction between the antiferromagnetic and ferromagnetic layers determines the magnetization of the adjacent ferromagnetic layer, Figure 2.7.

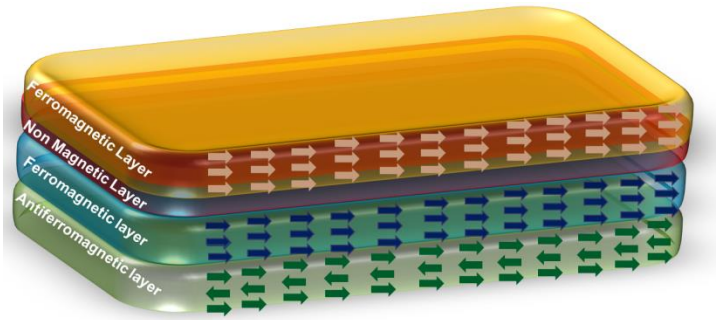

Figure 2.7 Exchange interaction between the antiferromagnetic and ferromagnetic layer. Top layer: Parallel alignment of the dipoles of the free pinned ferromagnetic layer. Bottom layer: Antiparallel alignment of the dipoles of the pinned ferromagnetic layer.

In order to keep a minimum value of energy, the magnetic dipoles have a preference to remain aligned with each other.

Magnetocrystalline energy

Crystalline materials are magnetically anisotropic as the main crystallographic axis of the structure provides for a preferential direction for orientation of the dipoles . This direction is called easy direction.

In this way, the magnetocrystalline anisotropy energy, E_k, corresponds to the work that is necessary to rotate the sample magnetization to a certain direction different of easy axis direction. This energy has a minimum value for an angle of zero between the magnetization and the easy axis, which means that when the magnetic field decreases to zero, the material will tend to align their dipole with easy axis.

Shape anisotropy

As mentioned above, crystalline materials have a preferential direction for orientation of the dipoles along the main crystallographic axis of the structure.

However, when a shape is given to the material, a magnetization is induced by reorientations of the dipoles in order to minimize energy and it is called demagnetizing field or self-demagnetizing field, Figure 2.8

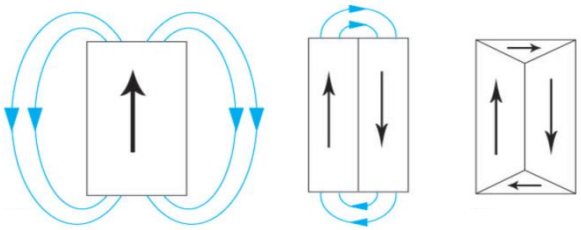

Figure 2.8 Ferromagnetic material divides itself into magnetic domains to reduce the demagnetizing field therefore reducing the magnetostatic energy. Figure adapted from [30]

2.2 Giant Magneto-Resistance (GMR) and Spin Valve (SV) sensors

A GMR structure is composed essentially by four thin films: a free layer (sensing layer) (FL), a conducting spacer, a pinned layer (PL) and an antiferromagnetic magnetic layer. The pinned, free and conducting layers are very thin, allowing the electrons to be frequently conducted back and forward the spacer. The magnetic orientation of the pinned layer is fixed and held in place by the adjacent antiferromagnetic layer. The magnetic orientation of the sensing layer changes in response to the magnetic field (H) [6,7].

The interaction among the layers normally aligns the magnetization of adjacent layers in opposite directions and electrons of both spins are scattered equally. If an external field is applied it aligns all the layers in one direction and it leads to a reduction of electrons scattering of one of the spins. As a consequence, the resistance of the sensor drops [7].

2.2.1.1 Macroscopic model for coherent rotation

Upon material deposition, both FL and PL have a configuration where their uniaxial induced anisotropy axes are parallel (parallel anisotropies), Figure 2.9.

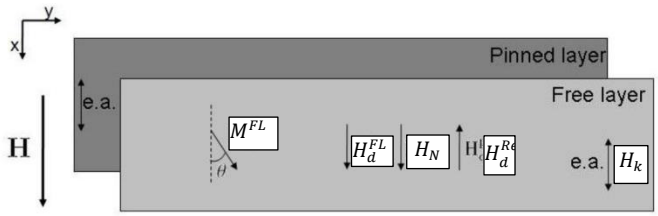

Figure 2.9 Schematics of the SV sensor composed by a pinned layer and a free layer with parallel anisotropies [6].

For the linearization of magnetoresistive (MR) sensors with micrometric dimensions, is considered that layers have a magnetic single-domain so edge effects can be neglected. The magnetization of a single ferromagnetic layer, M, can be described as a single collective vector, whose magnitude (saturation magnetization - Ms)

remains constant and orientation may vary in space and time,. The total energy associated with sensing layer has some contributions [6]:

$$\mathbf{E^{Fl}} = \mathbf{E_H} + E_d^{FL} + \mathbf{E_k} + E_d^{PL} + \mathbf{E_N} \qquad \textbf{Equation 1}$$

Where:

- $\mathrm{E_H}$ is the Zeeman energy or external field energy.

- E_d^{FL} is the demagnetization field energy or shape anisotropy energy of the free layer. The demagnetization energy, E_d measures the interaction between the magnetic film and demagnetizing field. When the material acquires a shape, a magnetization - self-demagnetizing field - is induced by reorientation of the dipoles in order to minimize its energy, Figure 2.10.

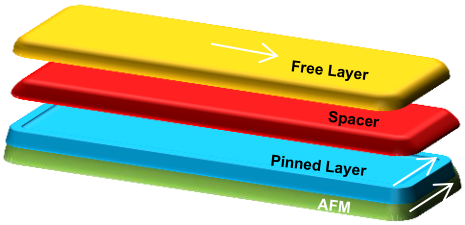

Figure 2.10 Typical device structure: the two ferromagnetic layers separated by a nonmagnetic spacer. The arrows define the magnetization of each layer, upon the material acquires a shape. The antiferromagnetic layer (AFM) is introduced to fix the magnetization of the adjacent layer (pinned layer).

- $\mathrm{E_k}$ is the crystalline anisotropy term. The minimum E_k is obtained when Ø is 0º or 180º, i.e, when the domains are orientated along the easy axis.

- E_d^{PL} is the demagnetizing field energy of the pinned layer.

- $\mathrm{E_N}$ is the Néel energy. The Neél coupling field (H_N), induced by correlation between interface roughness at the spacer interfaces with ferromagnetics. In spintronic multilayers, magnetostactic fields largely arise from roughness-induced surface poles. As device dimensions are reduced, the magnetic layers within stacks are more likely to become a single-domain, and then structural magnetostactic fields become more important, Figure 2.11.

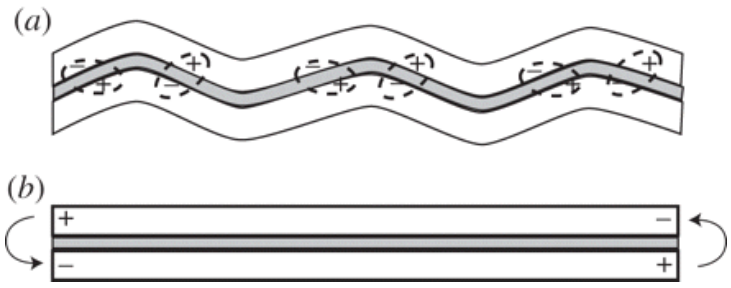

Figure 2.11 a) Magnetostatic coupling between magnetic layers; b) Dipolar coupling between layers [21].

To understand the conditions required for the linear behaviour of the MR device, Figure 2.12, one can consider the energy balance of the sensing layer with the following structure PL/Spacer/FL where the system is considered to be under the influence of an external field low than 500 Oe for the PL to have its magnetization fixed [6].

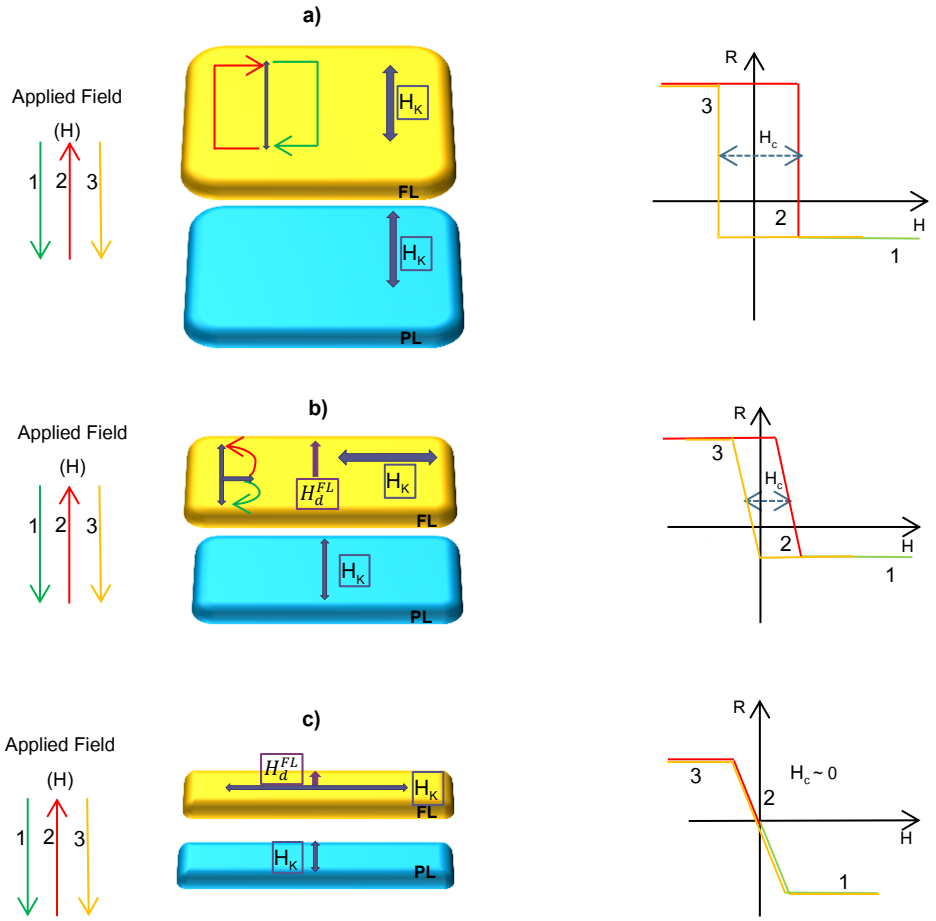

Figure 2.12 a) Transfer curve corresponding to parallel induced anisotropies, upon material deposition, showing that the magnetization reversal process along easy axis is predominantly domain wall motion; b) and c) Schematics of the effects of the material shape and dimensions in the crystalline anisotropy and shape anisotropy fields. The transfer curves show that the magnetization is a reversal process along the hard axis, which produces a coherent rotation of a domain wall motion. The PL crystalline anisotropy does not change his magnetization because it is fixed by AFM layer [6].

Figure 2.12a) represents the magnetization anisotropy, H_K, for the FL defined in parallel orientation with respect to the PL. In this configuration, the SV shows a step response from a maximum high resistance state to low resistance state, near the zero applied magnetic fields, reflecting the fact that the magnetization reversal process along easy axis is predominantly domain wall motion.

Figure 2.12b) shows schematics of the magnetization anisotropy of the FL defined in the transverse orientation with respect to the pinned layer due to the shape anisotropy effects. This allows the rotation of the magnetization of the FL when a magnetic field is applied, translating into a linear response of the SV between a high and low plateaus, reflecting the fact that the magnetization reversal process along the hard axis produces a coherent rotation instead of a domain wall motion. The uniaxial anisotropy can be obtained by applying a magnetic field during the film deposition or annealing process (Section 3). The origin of the induced anisotropy is the short range directional ordering, in which atomic pairs in a film tend to align with the local magnetization [6].

Carefull patterning and dimensioning of the SV is needed to manipulate the demagnetizing field of the FL, H_d^{FL}, Figure 2.12c).For the parallel anisotropy it is crucial that the FL induces a demagnetizing field along the easy axis direction, which is promoted by the shape anisotropy.

The easy axes for stable magnetization direction are 0 and π radians. If one cycle of magnetic field is applied in the perpendicular direction to the easy axis in ferromagnetic films, the magnetization direction changes from 0 to $\frac{\pi}{2}$ radians as the magnetic field increases, and $\frac{\pi}{2}$ to π radians as he magnetic field decreases, Figure 2.13.

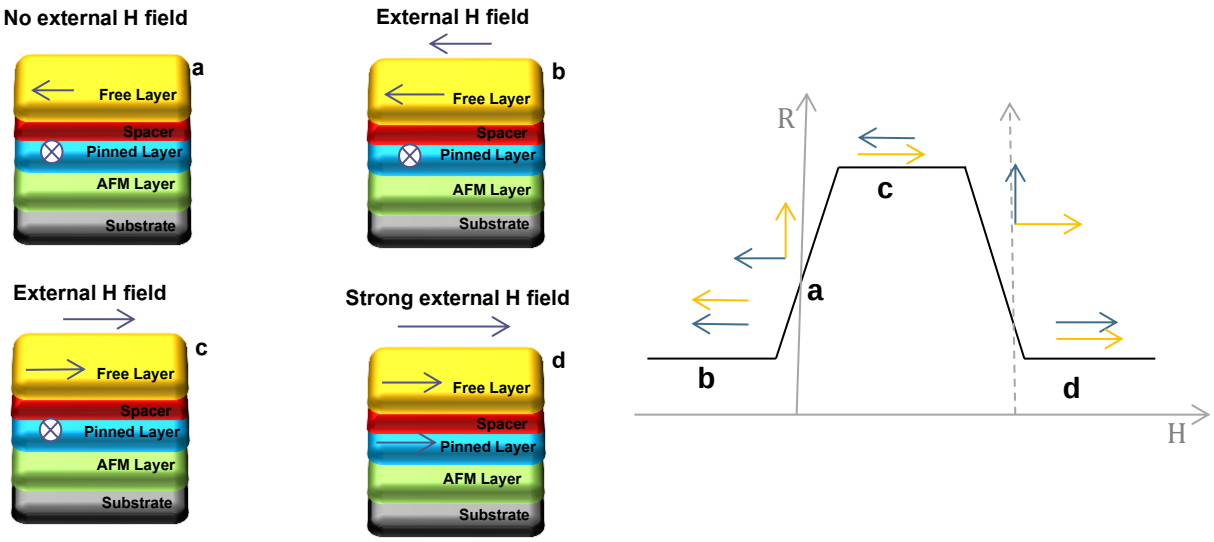

Figure 2.13 MR transfer curve principle. R(H) linear behaviour and typical magnetization orientations correspondence. The yellow arrows represent the free layer magnetization rotation and the blue arrows represent the pinned layer magnetization.

The magnetization direction of the PL can only be reversed at fields above the exchange bias field which can be as high as 500 Oe for pinned layers comprising a single ferromagnetic and anti-ferromagnetic layers.

2.2.1.2 Sensor Transfer Curve

The sensor behaviour is characterized by its transfer curve, which represents directly the output resistance dependence on field signal.

The name SV appears because if an external field is applied, this sensor acts as a valve for one of the electron spins. SV are sensitive not only the magnitude but also to the direction of the field in the plane [8].

A magnetoresistive device is a transducer which converts an external field into a resistance given a DC bias current supply.

The devices have a minimum (R_{min}) and a maximum (R_{max}) resistance plateau and the path from one level to the other should to be linear, allowing them to work as magnetic field sensors, Figure 2.14.

The magnitude of magnetoresistance effect is defined as follows:

$$\mathbf{MR}(\%) = \frac{\mathbf{R_{max} - R_{min}}}{\mathbf{R_{min}}} \times \mathbf{100} \qquad \textbf{Equation 2}$$

The GMR materials typically have MR ratios about 10-50% [9].

Saturation fields define the ideal linear range of the device, where a dR variation corresponds to a single dH value. The key feature of a magnetic sensor response is its field sensitivity, which represents how the sensor is reactive to a field variation. It can be measured experimentally from the slope of the transfer curve.

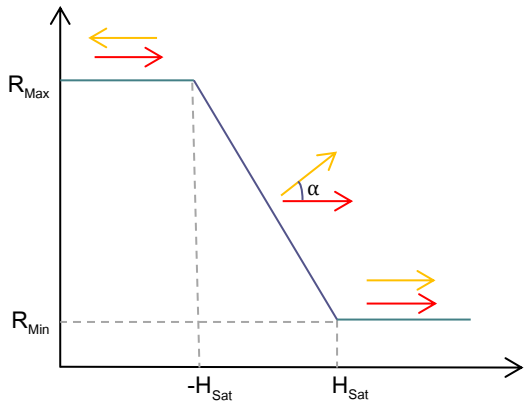

$$S = \frac{MR}{\Delta H_{linear}} \qquad \textbf{Equation 3}$$

Figure 2.14 Resistance vs. magnetic field transfer curve of a linear spin-valve at a given sense current. Red arrows represent magnetization direction of PL and the yellow ones represent the magnetization direction of the FL.

The sharp magnetization reversal near zero magnetic field is due to the switching of the FL in the presence of its weak coupling to PL. The relative orientations of two magnetic layers were indicated by the pairs of arrows in each region of the MR curve, where the resistance is larger for antiparallel alignment of the two magnetic layers [9].

2.3 Biosensors

The ability of magnetoresistive sensors to detect weak magnetic fields is present in many different applications. New and promising areas are biomedicine and biotechnology. In the last decade, biomolecular recognition plays an important role in areas such as health care, pharmaceutical industry and environmental analysis.

The main idea behind magnetoresistive biochips is to provide a good alternative to the traditionally used fluorescent marker devices. These devices use an expensive optical or laser-based fluorescence scanning system to detect fluorescent labelled biomolecules that recognize a known biomolecule which is previously immobilized on the sensor surface.

Among the variety of affinity biosensor systems based on biomolecular recognition and labelling assays, magnetic labelling and detection is emerging as a promising new approach. In magnetic biochips, the fluorescent markers are replaced by nanoparticles, and a magnetic sensor detects the stray field produced by the label giving an electrical signal. Magnetic labels can be non-invasively detected by a wide range of methods, are physically and chemically stable, relatively inexpensive to produce, and can easily be made biocompatible.

A typical magnetoresistive biochip owns the following features:

I. An array of magnetoresistive sensors in which biomolecules are immobilized. These immobilized biomolecules are called probes.
II. A hybridation chamber, usually based on microfluidic channel arrangements.
III. A target arraying mechanism. This part consists on focusing the target elements on the probe sites using an electric field for charged molecules, a magnetic field generating lines for targets with magnetic particles or simply be based on diffusion.

The targets are the biomolecules to be detected and they are incubated in the chip in order to the biomolecular recognition occur. The labelling of the targets can be executed before or after the recognition step. Typically, the magnetic labels are superparamagnetic particles and can be attached to the target biomolecule. Under a small magnetic field, these particles acquire a magnetic moment which produces a fringe field over the sensor. This induces a change in the MR sensor resistance that can be detected with an acquisition setup

The advantages of this biochip are the fast response and the high sensitivity, the easy integration and automation, being a good approach of a Point- of-Care system.

In this work, magnetic labelling and detection were applied to biosensing. This work aims at an optimization of a platform cell cytometer-based for in-flow detection of magnetically labelled cells with magnetoresistive sensors [4]. In particular, it is presented an example for the validation platform, a magnetic counter platform that identifies Staphylococcus in milk, although this platform can be used for several other biological detections.

Chapter 3

Materials and Methods

Sensitive Spin Valve sensors can be combined with microfluidics and biochemistry in a miniaturized biosensor that is suitable for detection of magnetic beads [7].

3.1 Spin Valve Chip Design

In this project, SV sensors are used and it is required they possesses linear response and a low noise level.

When this project started at INESC-MN, the sensor array, whose mask is represented below in Figure 3.15, comprises 28 individual spin valves arranged in 7 by 4 sensor arrays. The active sensor area of each individual sensor is 100 μm x 3 μm and the 28 sensors occupy a total area of 8,86 mm by 2,59 mm.

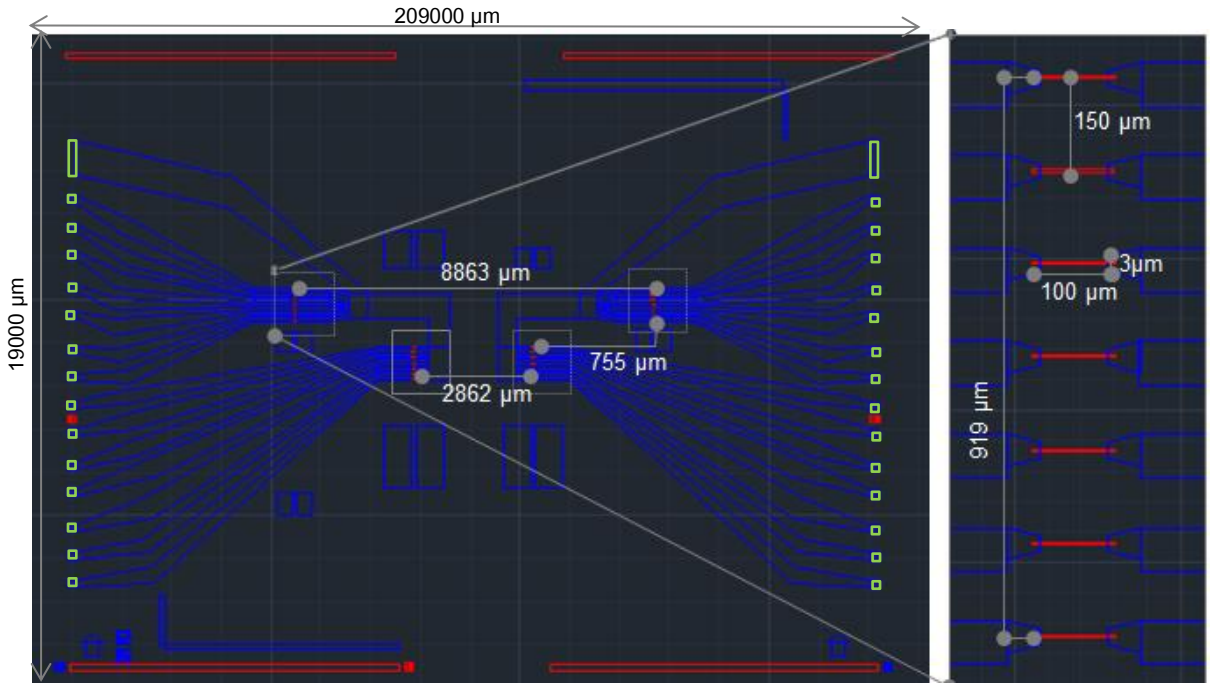

Figure 3.15 Design detailed of the biochip mask in AutoCad®: chip array of 28 SVs in red displayed vertically in the centre of the chip, the contact leads are presented in blue lines and the frame for electrical contact at the end of each contact leads displayed in green lines.

3.2 Microfabrication

Fabrications of micrometre size magnetoresistive sensors require a clean environment, as the dimensions of the device's structures are smaller than most dust grains, airborne microorganisms, aerosol particles and other impurities presents in the atmosphere. A cleanroom has a controlled level of contamination that is specified by the number of particles per cubic meter at a specified particle size.

The microfabrication of the devices used along this thesis is achieved by combining photolithography, etching and lift-off techniques. It is a standard process at INESC-MN, which was optimized and used over the past years by several colleagues.

It comprises fourteen steps which are briefly discussed below. The Appendix A includes the run sheet for more detail.

STEP 1 - Deposition of Alumina (Al_2O_3): The Si wafer was cleaned and then a layer of Al_2O_3 was deposited. This layer prevents current leakage from the device, as the Si wafer is a semi-conductor.

Sputtering systems are used to deposit thin films. Sputter deposition is a type of physical vapour deposition (PVD), achieved by the condensation of a vaporized from the desired film material onto a silicon wafer. This is accomplished by plasma near the target using a magnetron in a vacuum chamber and an inert gas, Argon (Ar). The Ar is ionized to Ar^+ and will bombard the target, because the target is being negatively biased.

STEP 2 – Spin Valve Deposition: The Spin Valve stack was deposited by ion beam deposition in the Nordiko 3000 ion beam deposition and milling system. The Ion Beam Deposition (IBD) employs ions to sputter one of the six targets, which can be individually selected for deposition. These ions are accelerated and converged into a beam on the deposition gun. The material sputtered from the target is deposited onto a substrate. The substrate table has a permanent magnet array producing 40 Oe magnetic field that defines the easy axis of the films during the deposition.

One of the SV stacks deposited at INESC-MN was composed of 15Å Ta/ 25Å NiFe/20Å CoFe/ 21Å Cu/ 20 Å CoFe/ 60 Å MnIr/ 20Å Ta, Figure 3.16, and it was used in this thesis.

Test sample showed magnetoresistance of MR ~5-6%.

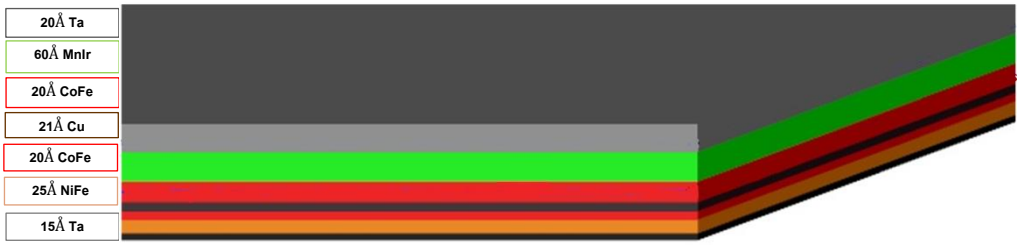

Figure 3.16 Schematics of one SV structure used in my thesis.

STEP 3 – Spin Valve Definition: This consists on a photolithography procedure that is the definition of the mask with the desired shape into a photosensitive material called photoresist (PR). Some steps, described below are required:

STEP 3.1 – Vapor Prime pre-treatment and coating: The pre-treatment is made in vapor prime machine and consists on the deposition of an organic compound HDMS (Hexamethyldisilane, $C_6H_{18}Si_2$) under a temperature of 130ºC and in vacuum.

After this pre-treatment, the sample is coated (Figure 3.17A) with 1,5 µm thick photo sensitive polymer - photoresist (PR) – being the SV shape patterned by photolithography (Figure 3.17B) according to the design draw in AutoCad® mask (Figure 3.17C). The spin coating is performed in Silicon Valley Group (SVG) coating system at a rotation speed of 3200 rpm during 30 seconds, being baked afterward at 85 ºC during 1 min to evaporate the solvents and improve PR uniformity.

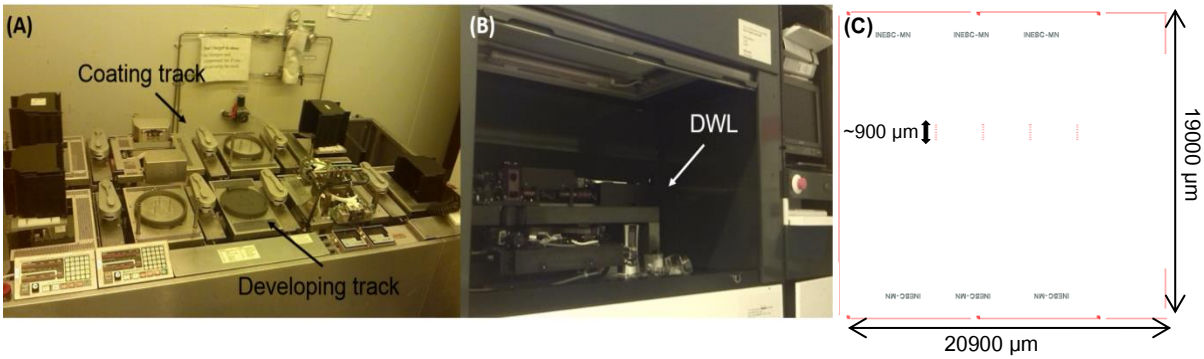

Figure 3.17 (A) SVG autonomous coating and development tracks system; (B) Direct Write Laser (DWL) system for lithography exposures; (C) AutoCad® Mask for first lithography: sensor's definition. Chip with array of 28 SVs in red displayed vertically in the centre of the chip.

STEP 3.2 – Lithography: The mask design transfer is performed by Direct Write Laser System (Heidelberg DWL, Figure 3.17B) which uses a diode laser (405 nm wavelength) to write over the sample. Under such exposure, irradiated areas of the resist undergo structural/chemical modifications such that they have differential solubility in a developing solution with respect to exposed areas. This structural modification may reduce or enhance solubility (referred to as negative or positive resists, respectively), by cross-linking or scission of polymeric chains.

A positive PR is used, which means that exposed areas become more soluble due to the break of the polymer connections. The only areas which are not exposed are the ones delimited by the SV shape borders.

To develop the patterned design, the sample is baked at 110ºC, during 1 min, to finish the incomplete PR reactions and then a solution is poured over it to dissolve the exposed regions while the non-exposed areas remain intact. The development is made in the SVG developing system.

The coating, exposer and development procedure remain the same for all the following lithographyies performed during the sensors fabrication.

STEP 4 – Spin Valve Etch – Nordiko 3600: The etching process removes the material that is not protected by the PR until the substrate is reached, Figure 3.19. The process involves high energy Ar^+ ions bombardment of the sample, provided by assist gun, Figure 3.18.

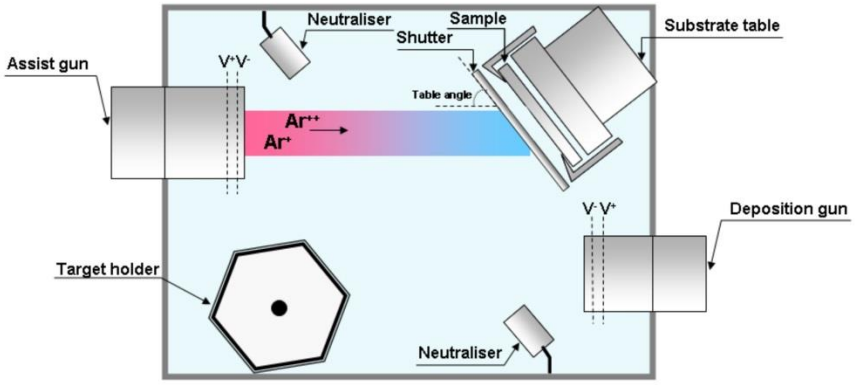

Figure 3.18 Ion beam system configured for the ion milling and O_2 bonding mode. In this configuration only the assist gun is activated in order to etch the substrate surface.

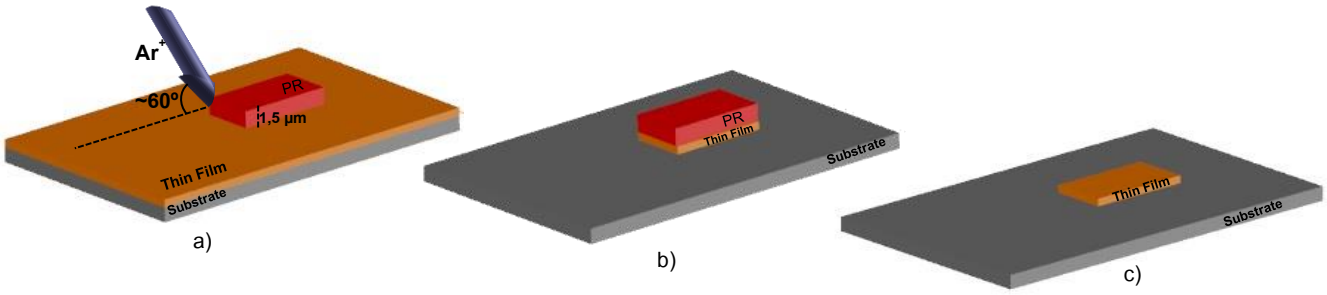

Figure 3.19 Etching process: a) Patterning of the PR by photolithography b) Etching of the non-protected thin film layer c) sample after etch and resist strip.

STEP 5 – Resist Stripping: The resist is stripped by immersing the sample in Microstrip 2003 solution and applying ultrasounds. It will remove the non-etched PR on top of the patterned structure, and in result the film remains outside the PR defined area.

STEP 6 – Contacts leads definition (similar to STEP 3 – Spin Valve Definition): The sample is coated with PR, the designed mask (Figure 3.20) for the contact leads pattern is exposed in the DWL and then developed. The difference lies in a non-inverted mask exposure, that allows the PR to remain outside the structure area designed.

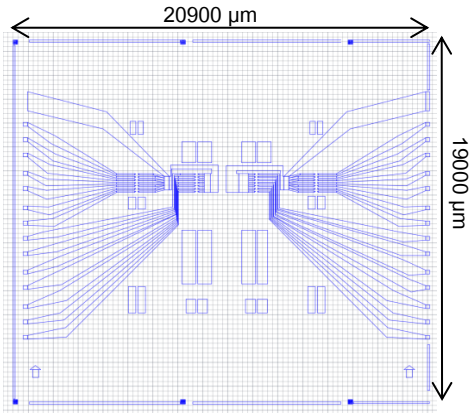

Figure3.20 AutoCad® mask for second lithography: contact leads definition. The contact leads are presented in blue.

STEP 7 – Deposition of Aluminium: In this step, 3000 Å of Al and 150 Å of $TiWN_2$ are deposited over the sample by sputtering deposition in Nordiko 7000, Figure 3.21.

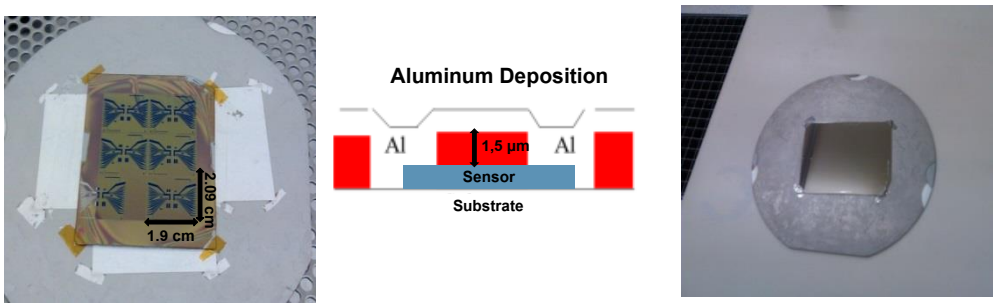

Figure 3.21 Thin film deposition process.

STEP 8 – Lift-Off of Aluminium: The lift-Off process is performed for removal of remaining material over PR shape, Figure 3.22.

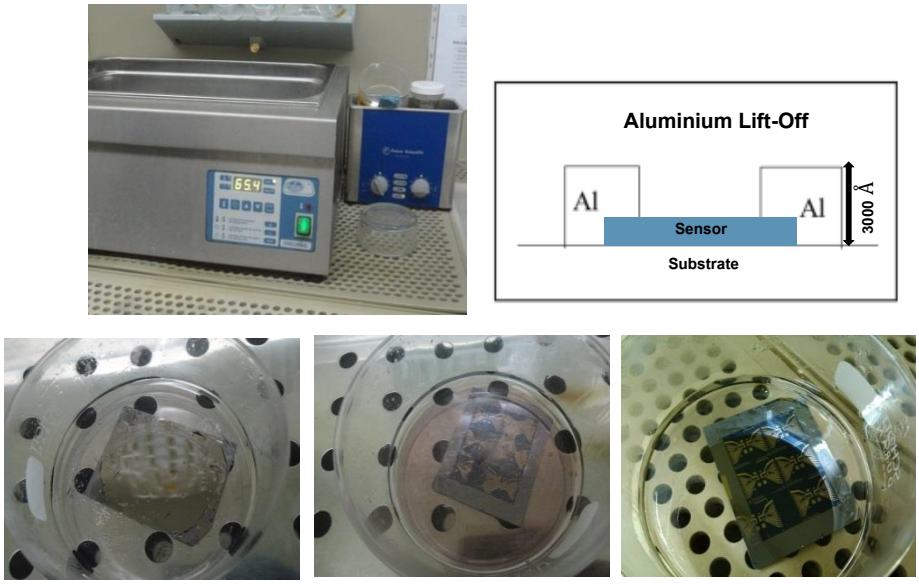

Figure 3.22 Photoresist and metal lift-off in wet bench.

STEP 9 – Deposition of Silica Nitrite (Si_3N_4): The deposition of a thin film of Si_3N_4 is performed for electrical insulation and passivation, Figure 3.23.

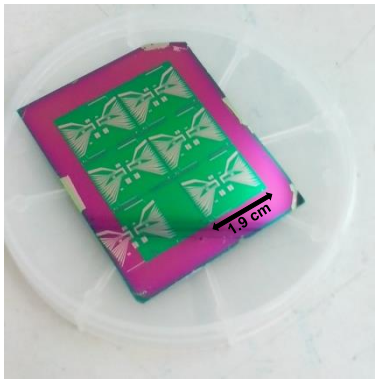

Figure 3.23 Optical verification of Si_3N_4 deposition: passivation layer.

STEP 10 – Vias definition (similar to STEP 3 and 6 – Spin Valve Definition and Contacts leads definition): The sample is coated with PR and the design mask, Figure 3.24, is exposed in the DWL system and developed.

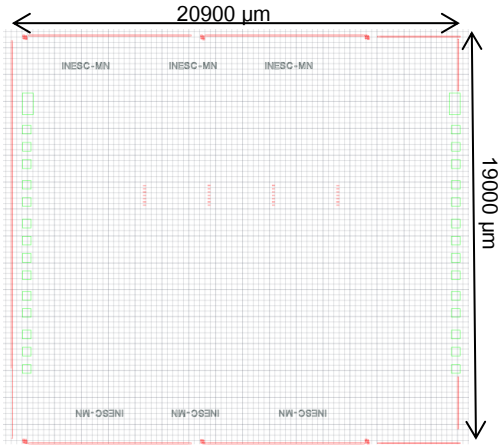

Figure 3.24 Design AutoCad® of the chip with the SV displayed in red. The frame for electrical contact at the end of each contact lead is displayed in green.

STEP 11– Reactive ion etching – pads opening: Deposition of a passivation of Si_3N_4 layer is performed on LAM Rainbow Plasma Etcher 4400 for accessing the Al metal lines, Figure 3.25.

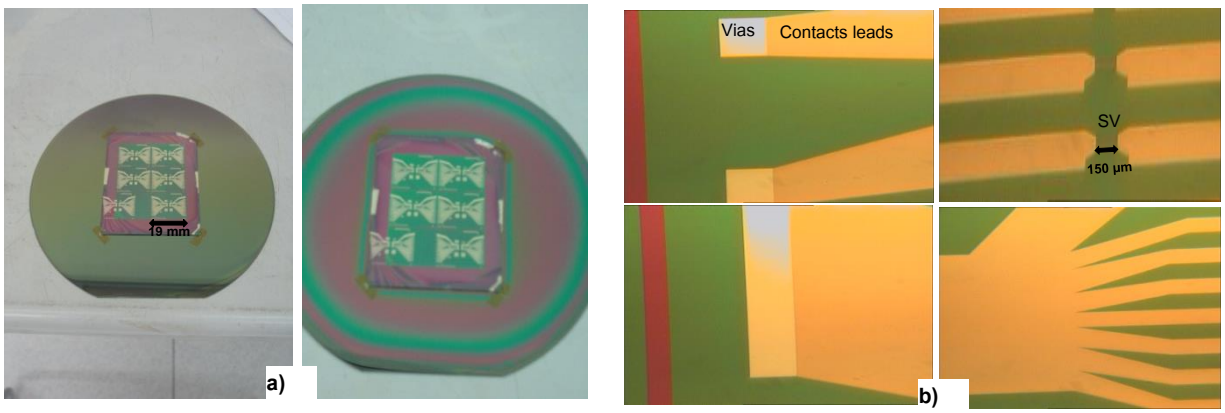

Figure 3.25 Reactive ion etching for pads opening. a) Visual and b) microscopic verification of defined SV, vias and contacts.

STEP 12 – Wafer Dicing: Usually, several dies of chips are fabricated on a silicon wafer, thus it is necessary to cut each die. The dicing is done by an automatic dicing saw, Disco DAD 321 machine, in order to individualize the chips for the encapsulation, Figure 3.26.

Figure 3.26 Sample was cut into individual dies.

STEP 13 – Resist Strip (similar to STEP 8): The resist strip will remove only the material over the PR remains, Figure 3.27.

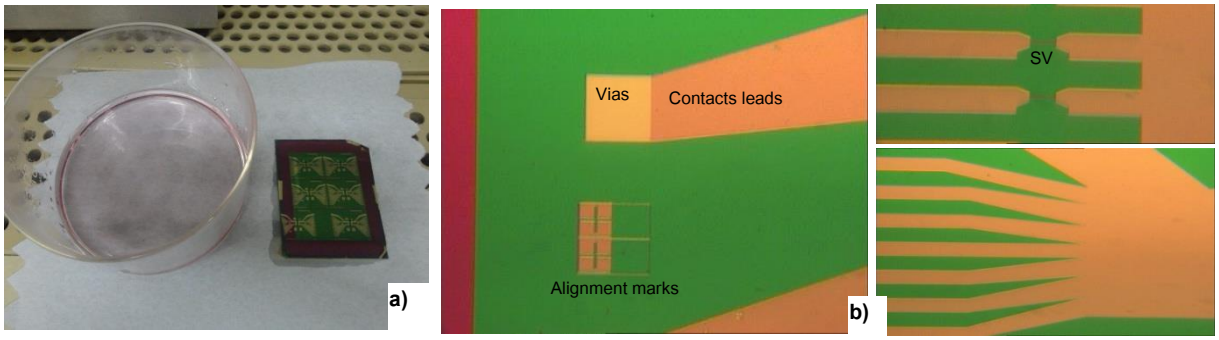

Figure 3.27 a) Resist stripping; b) Microscope observation.

STEP 14 – Annealing: The annealing of the individualized chips were performed in the 21100 Tube Furnace (BL Barnstead Thermolyne) at 250ºC for 15 min and naturally cooled with constant magnetic field of 1 KOe in vacuum environment.

It is a heat treatment wherein material properties are changed. Annealing is used to induce homogeneous orientation for the magnetization that occurs in the interface of the PL and AFM layer. The samples are heated up to a temperature above the blocking temperature, maintaining this suitable temperature for 15 min and then cooling down in the presence of an aligning 1 T magnetic field.

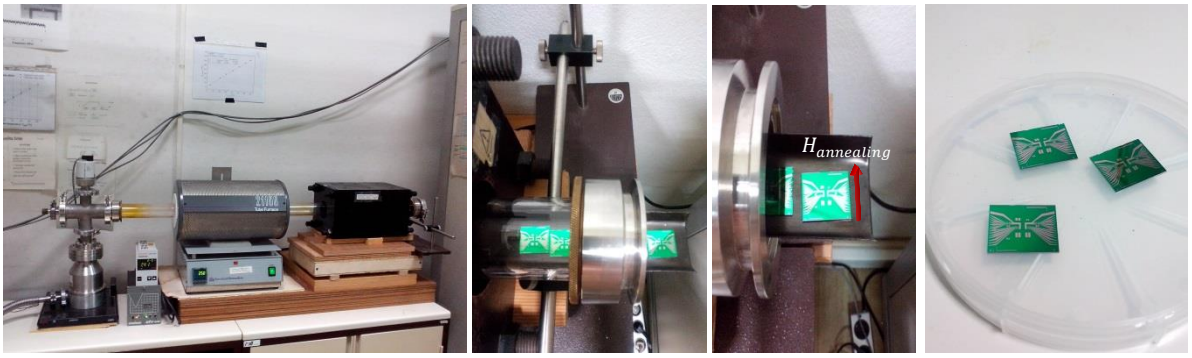

Figure 3.28 Annealing of each individualized chips.

A full detailed run sheet for the biochip fabrication process is found in the Appendix A.

3.3. Electrical Transport Characterization of SV sensors

The system used for electrical characterization of SV sensors comprises two pairs of micro-positioning probes with TiW needles, a voltmeter, two current sources (one for the sensors biasing and other to create the applied magnetic field) and two Helmoltz coils, Figure 3.29.

The probes were placed in contact with the electrical leads of the sensors (pads) by scratching the surface of the pads in order to make sure that the contact was made with the AlSiCu contacts. The probes supplied the contact with a bias current, a current of 1mA was used (applied by a Keithley 220 current source), measuring at the same time the output voltage (measured by voltemeter Keithley 182).

The external magnetic field is generated by two Helmholtz coils connected in series and the sample is placed between them with the easy axis parallel to the generated field. The magnetic field is created by two coils and varies between -140 and 140 Oe. All the setup components are connected to a computer through a GPIB connector, where a custom software controlled the current source and acquires and interprets the signal received [10].

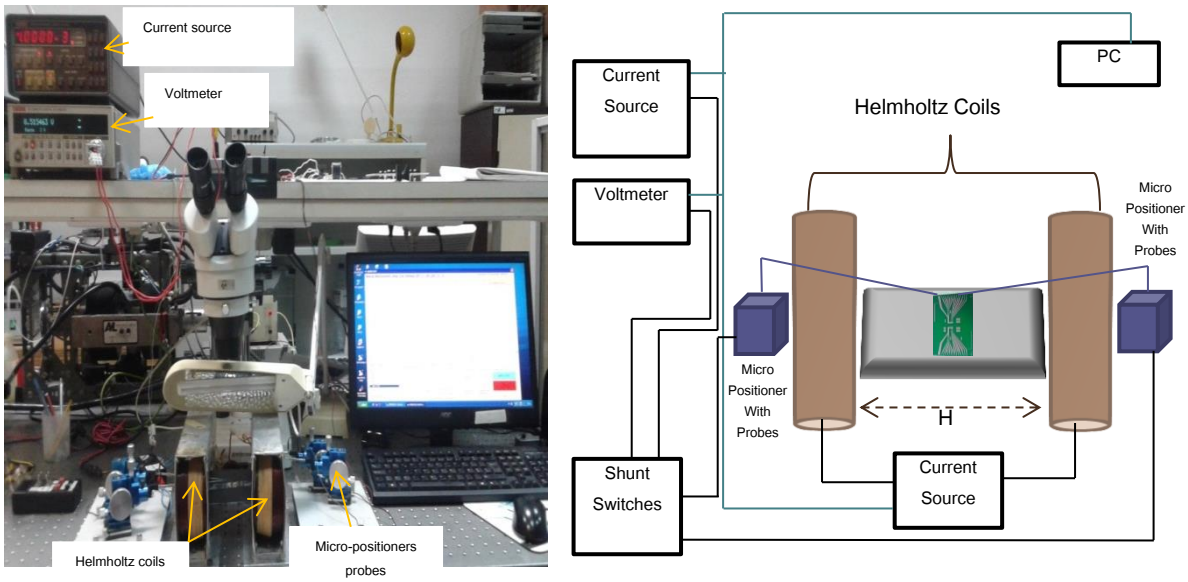

Figure 3.29 a) Transport Characterization setup; b) Schematic diagram of the setup employed for the electrical characterization.

Transfer curves (curve of Resistance vs external DC magnetic field) were measured in this setup, Figure 3.30.

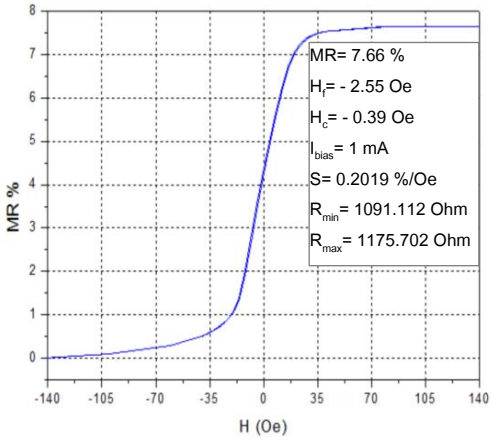

Figure 3.30 Electrical Transport Characterization, MR curve of the Spin valve.

Figure 3.30 shows an example of one SV transfer curve, centred for zero applied field, with resistance varying between 1091 Ω and 1174 Ω when applying 1 mA biasing current.

The quality and performance of a SV for detection purposes can be evaluated by some parameters:

I. Magnetoresistance ratio (MR), which gives the relative variation in the sensor resistance between the parallel and antiparallel magnetic orientation of the PL and FL, such that, the maximum resistance variation that sensor can suffer.

II. Bias point/effective coupling field (H_f), which gives information about the deviation that the sensor transfer curve suffer from the zero field. This is a very important parameter, since sensing application is performed by detecting a resistance change according to a variation of the magnetic field from its 'resting' state in zero field. This value should not exceed 10-20 Oe (~1592 A/m) [15].

III. Coercive field (Hc), which measures the intensity of the magnetic field required to reduce the magnetization of the material to zero field after the magnetization of the sample has been driven to saturation.

IV. Sensitivity (S): The sensor's sensitivity is the capability for the sensor to detect small magnetic fields. For the sensor to have a high sensitivity it needs to have a significant variation of resistance for very small fields in order to detect even the smallest field whether it is coming from magnetic particles. The sensitivity can be related with the sensor's transfer curve (Figure 2.14).

3.4 Microfluidic system: PDMS channels and permanent bonding

A system that portraits 4 microchannels were designed (Figure 3.31) in a previous work by A. Fernandes [4] and used in this thesis, in order to use each group of seven sensors independently.

The microfluidic channels are fabricated with Poly(dimethylsiloxane) (PDMS), which is one of the most widely used materials and it was chosen to replicate the channels since it uses cheap and fast techniques and it is biocompatible.

PDMS is composed of cross-linked siloxanes with backbone (-Si(Ch_3)$_2$-O-) and is typically produced by adding a curing agent in 1:10 weight ratio, forming a material which is intrinsically hydrophobic but can be treated to become hydrophilic.

The microfluidic system has 4 pairs of inlet and outlet holes, as illustrated in AutoCad® mask (Figure 3.31), where the channels have 50 µm height.

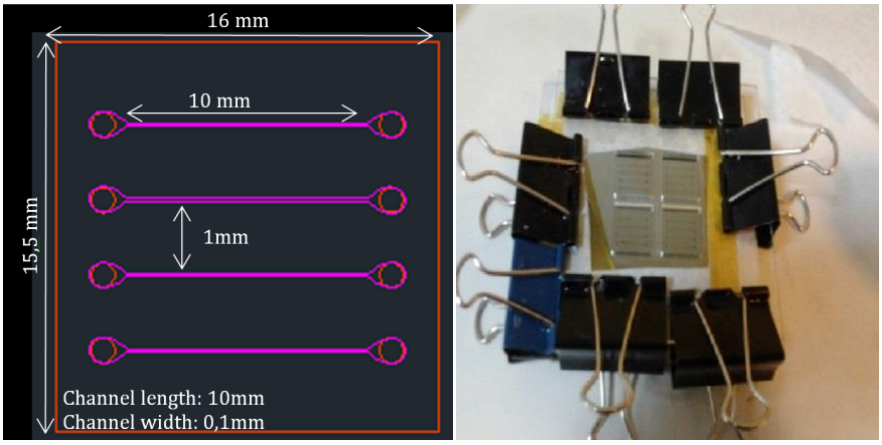

Figure 3.31 Top view of the microchannels in the AutoCad® mask and assembled mold and PMMA plates for PDMS casting.

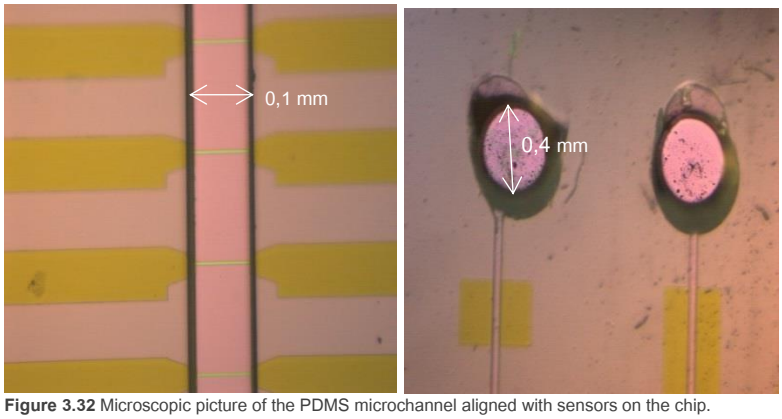

Figure 3.32 Microscopic picture of the PDMS microchannel aligned with sensors on the chip.

The width of the channels (100 µm) was chosen in agreement with the sensor's size to maximize the contact between the particles and the sensors. In order to have particles as close as possible to the sensor without blocking the channel, the channels height was design to be 50 µm.

The microfluidic channel directly interfaced the biosensor array, Figure 3.32, with its opening void and magnetic particles flow at a constant flowrate over the magnetic sensor surface.

The integration of microfluidic system in the biochip surface is achived by permanent chemical bonding, sealing PDMS and chip surfaces to each other after Ultraviolet and Ozone (UV-O) treatment of both pieces. To seal the microchannels on the chip an irreversible chemical bonding between both surfaces was performed, when they are submitted to oxygen plasma activation, Figure 3.33.

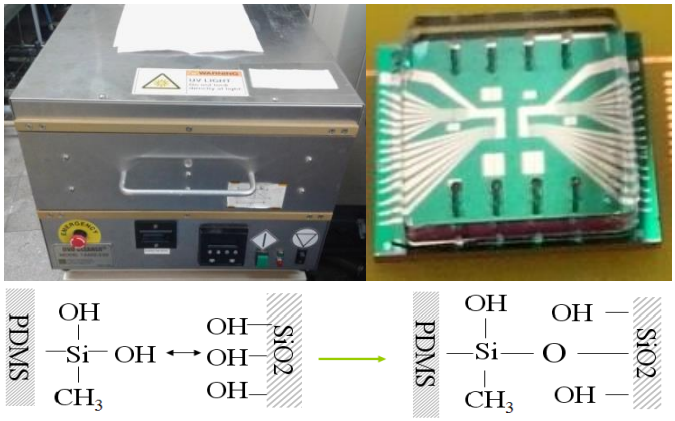

Figure 3.33 UV-O Cleaner system and a picture of the microchannel bonding with biochip.

A detailed run sheet for microfluidic fabrication process and permanent bonding is found in the Appendix B and C.

3.5 Wirebonding and Encapsulation

For better handling, each biochip is firstly glued to a printed circuit board (PCB), Figure 3.34c).

Then, a technique known as wirebonding connects the metal contacts on the chip to designed contact pads, by thin aluminium wires. Electrical pads and wires are then covered with a silicon layer, protecting them from corrosion during biological experiments, Figure 3.32b).

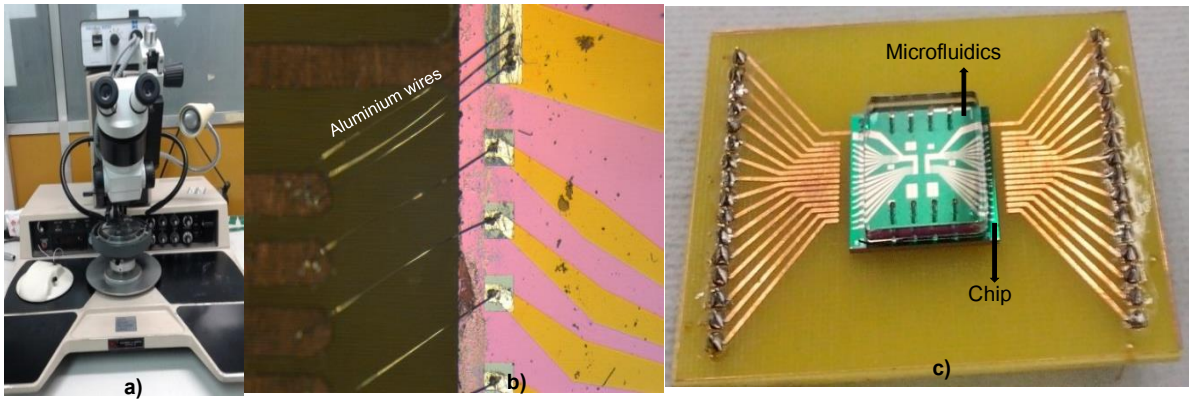

Figure 3.34 a) Wire bonding machine; b) Microscope picture of the connections between sensors contacts and the copper contacts of the PCB; c) PCB with mounted and bonded biochip.

After performing the wirebonding, the SV chip is characterized once more to ensure that all connections were made appropriately. Sometimes, at this stage, it is noticed that some sensors are impossible to characterize. There are two reasons for this to happen:

i. The wirebonding is a manual process that is error prone and due to the flexible nature of the axon cable it ‘s frequent to break the connection while handling the platform, even with the silicon protection cover;

ii. The flexibility of the axon cable leads to unstable connections among components.

3.6 Magnetic Labelling and detection

Magnetic nanoparticles (MNPs) can be used as a labelling method for biomolecules and cells and it is desirable to use superparamagnetic beads, i.e. small ferromagnetic particles.

In contrast to bulk ferromagnetic material that has multiple magnetic domain structures, superparamagnetic particles just have a single magnetic domain bellow a critical size, where all magnetic spins align unidirectionally and its magnetic coercivity is zero, Figure 3.35, [12].

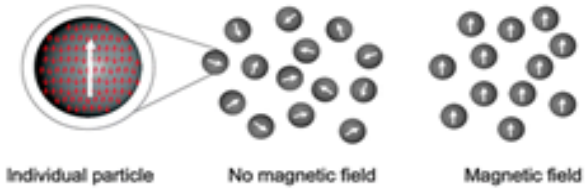

Figure 3.35 superparamagnetic particles behaviour in the presence and absence to an external magnetic field.

These particles quickly lose their magnetic moment in absence of an external magnetic field, because the dipole moment of a single domain fluctuates rapidly in the core due to thermal excitation, so there is no magnetic moment for macroscopic time scales. This property avoids particle clustering.

However, in the presence of an external field, they can be readily magnetized to large magnetic moments, facilitating detection. This can be achieved by two sources:

- A permanent magnet;
- A magnetic field induced by a coil.

In this thesis, a permanent magnet, placed under the chip, is used to superimpose an external magnetic field to magnetize the magnetic beads.

As MNPs will label biomolecules it is important to ensure that they are:

i. Biocompatible, in order to not react or degrade the biological samples;

ii. Hydrophilic, to ensure monodispersing over the sample;
iii. Spherical surface which benefit the monodispersing over the sample;
iv. Be able to functionalize by antibodies.

The biosensor's real time readout gives instantaneous feedback of the particle's that pass over the sensor at the given flowrate.

The size of magnetic particles is an important factor for the particle's magnetic moment and forces since larger particles generally have larger magnetic moments [13].

3.6.1 Magnetization Method

If the MR sensors lie in XY plane, the sensors detect only the X and Y components of the magnetic field. Therefore, to detect a superparamagnetic bead resting on a MR sensor, a magnetic field is externally generated in the Z direction, causing the bead to produce a magnetic field in x direction, as the detectable component, Figure 3.36A,B [14].

The bead creates a magnetic fringe field $|\vec{H}(\vec{r})|$ at position $\vec{r}$, from the position of the dipole (bead) centre, that can be approximated by the field of an induced magnetic dipole $\vec{m}$ situated at the centre of the bead, assuming a spherical bead.

$$\vec{H}(\vec{r}) = \frac{1}{4\pi}\left(\frac{3(\vec{m}.\vec{r})\vec{r}}{\vec{r}^5} - \frac{\vec{m}}{\vec{r}^3}\right) \qquad \text{Equation 4}$$

The field produced by the bead is sensed at the sensing layer and consequently, the sensor response depends on the position of the magnetic bead with respect to the sensor.

3.6.2 Detection Scheme

The principle of detection employed by the magnetic sensors for magnetic bioassays involves a magnetic transduction mechanism. Magnetic biosensors detect the stray field of magnetic particles that are bound to biological molecules, by a biomolecular recognition mechanism, such as antigen-antibody affinity [9].

Since the biological environment is usually non-magnetic, the possibility of false signals being detected is negligible. Superparamagnetic nanoparticles make ideal labels in bio applications using magnetic sensors, because they can be readily magnetized to large magnetic moments.

There are two relevant directions for applying the external magnetizing field: parallel or perpendicular to the sensor plane. Depending on the configuration, different pulse shapes will be measured using the dynamic mode.

For parallel magnetization, the average field, over the sensor FL, has a polar configuration while the perpendicular magnetization gives origin to an average field with a bipolar configuration [22].

Magnetizing the beads in the sensitive directions of the sensor (x and y directions) limits the magnetizing field since the sensor should not be saturated. As the sensors are only sensitive to in-plane fields (x and y components of the field), it is thus advantageous to apply the magnetizing field perpendicular to the sensor plane (z direction) [13].

During this thesis, a permanent magnetic was used to magnetize the nanoparticles. This field can be applied in one of the three directions: x, y, z. It is important to notice that magnetoresistive sensors will only be sensitive to the x direction.

In this case, it is applied a perpendicular field (z-direction), Figure 3.36 A. In this configuration, a high magnetic field H_z can be applied, since in the z direction the demagnetized field of the FL is very high.

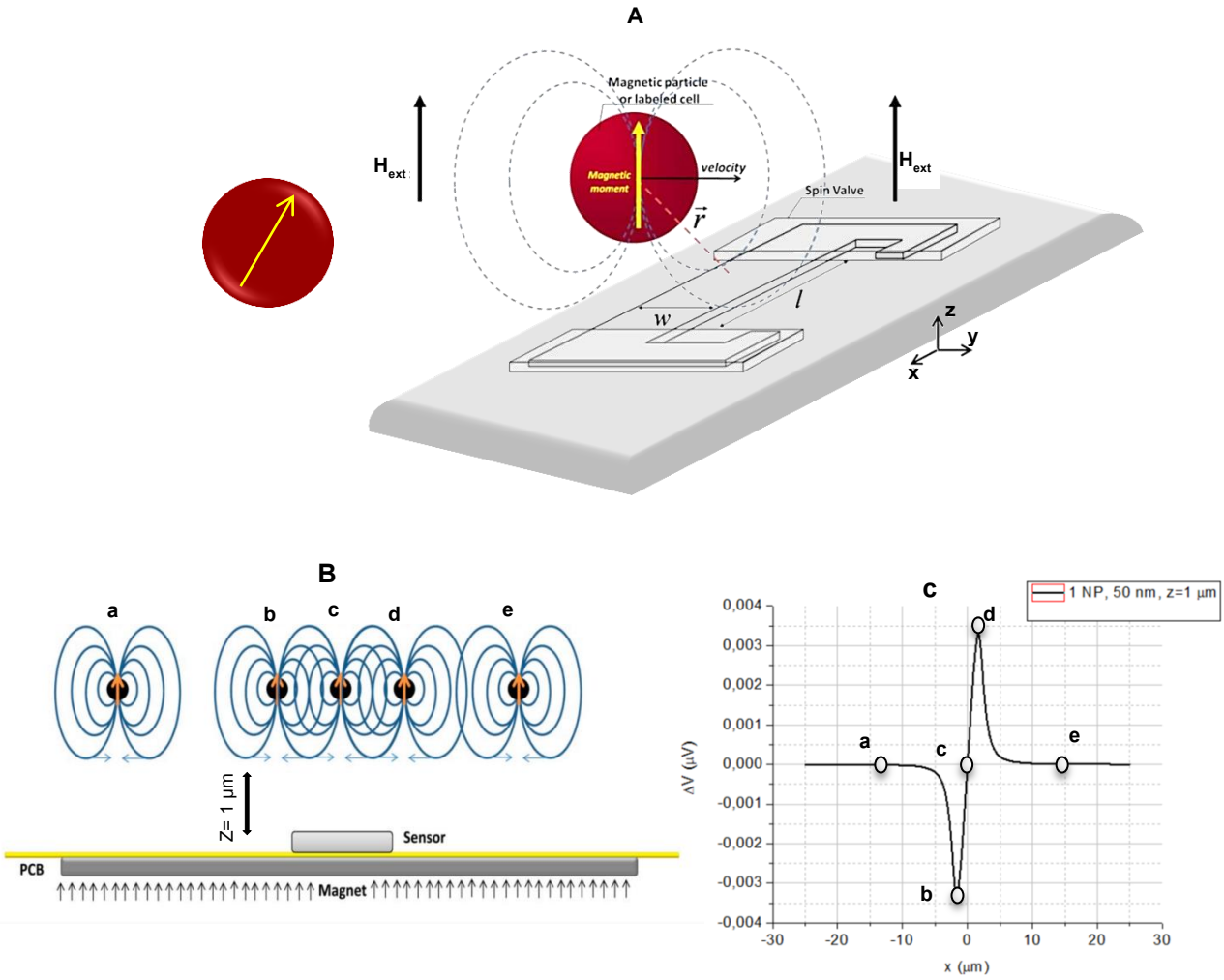

Figure 3.36 Schematics of MR sensor detection of magnetically labeled targets flowing above the sensor for perpendicular magnetzation A [10] and B [4]; Perpendicular magnetization gives origin to an average field with a bipolar configuration C.

When a perpendicularly magnetized particle (Figure 3.36A) passes over the sensor (Figure 3.36B), it produces a voltage in the sensor which has a typical bipolar shape (Figure 3.36C), as the fringe field of a particle is spherically symmetric. As the particle approaches the sensor, it starts detecting the horizontal component of the

particle's fringe field. Assuming that the sensor's PL is oriented to the right, the first horizontal field component that the sensor detects is oriented to the left, and it leads that the first magnetic field measured by the sensor is negative (Figure 3.36C, b). When the particle is centred over the sensor, the right and left field components of the fringe field will cancel themselves which translates in a zero magnetic field (Figure 3.36C, c). When only the right horizontal field component of the fringe field is over the sensor, another maximum will be observed before the particle lows away from the sensor (Figure 3.36C, d) [4].

The sensor transforms the nanoparticles induced magnetic field change into a resistance change, which can be electrically read out. The acquisition is performed by converting its analogic signal into a digital one capable of being processed by a computer. This change in the resistance can be translated into a variation in potential, which will be the setup's output signal. To calculate the average potential changes read as the output of the sensor, Ohm's law is used:

$$\Delta \mathbf{V} = \Delta \mathbf{R} \ \mathbf{x} \ \mathbf{I}, \qquad \textbf{Equation 5}$$

knowing that the sensor sensitivity is proportional to the slope of its transfer curve and the changes in resistance is given by:

$$\Delta \mathrm{R} = \mathrm{sensitivity} \ \mathrm{x} \ \mathrm{H}_{\mathrm{MNP}}. \qquad \textbf{Equation 6}$$

The amplitude of the signal is dependent on the height of the label and the time span is dependent on speed on label velocity.

3.7 Characterization of Magnetic Nanoparticles

The moment of the bead, which depends on the magnetic composition and content, is related to the applied magnetic field. The moment increases with an increase in the applied field, with a linear response, until the field becomes saturating and the moment no longer increases [15].

The Vibrating Sample Magnetometer (VSM) system (Figure 3.37) measures the magnetic moment of some material. It allows the magnetic moment measurement of magnetic particles as a function of the applied magnetic field.

In order to evaluate the magnetic characterization of Dynabeads® 2800 nm and Micromod® 50 nm MNPs, 20 µL of each sample stock concentration was measured. The measured moment corresponds to the sum of the magnetic moment of the sample. To evaluate the magnetic moment *per* particle, this value was divided by the number of particles in the sample:

$$\frac{\text{Magnetic moment of all beads in solution } (\mathrm{Am}^2)}{\text{Number of beads in solution}} = \text{Magnetic moment per bead} \qquad \textbf{Equation 7}$$

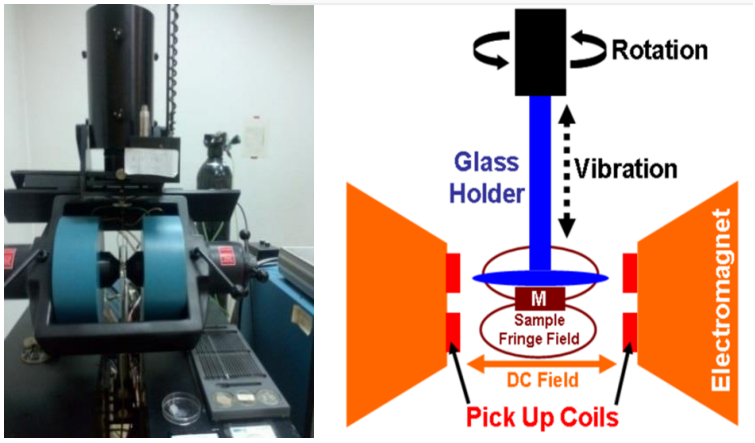

Figure 3.37 Picture of the VSM system used at INESC-MN and schematic illustration of the pick up coils and quartz rod.

Two large coils are responsible for the creation of the magnetic field which defines the sample magnetization. The sample is assembled onto a quartz rod that is connected to piezoelectric crystal, which under excitation makes the sample vibrate. In the region between the large coils, near the sample, two smaller coils were placed. Being a magnetic material, the sample creates a magnetic field collected by the smaller coils. Because the sample is moving the magnetic flux crossing the plane of inner coils is not constant and a current, proportional to the variation rate of the flux, will be induced on them. That current depends on the magnetic moment of the sample.

The goal of this procedure is to determine the magnetization of saturation of nanoparticles in order to verify if the permanent magnet that it is being used to magnetize the beads has a sufficient high magnetic field for beads detection.

Figure 3.38 shows two typical magnetization curves obtained from VSM measuremets. In this particular case, Micromod® 50 nm particles and Dynabeads M-280 (2800 nm) particles were measured in the range of -1400 Oe and 1400 Oe.

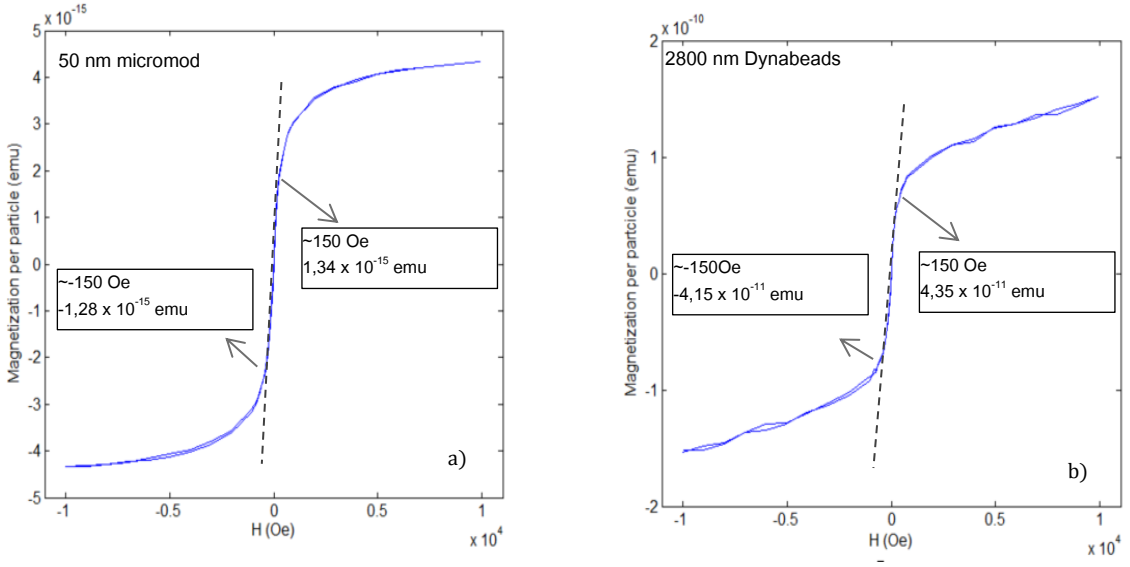

Figure 3.38 Magnetic properties of magnetic beads, measured by VSM. a) Magnetic moment per 50nm particle. b) Magnetic moment per 2800nm particles.

In the biochip detection system later described, it is verified that the permanent magnet has a perpendicular magnetic field near the sensors area of ~150 Oe, which is used to magnetize the magnetic particles.

Taking into account this value of perpendicular field, it is possible to know by VSM transfer curves that for a 50 nm particle at ~150 Oe, the magnetic moment measured was 1,34 x 10^{-15} emu. On the other hand, for a 2800 nm particle the magnetic moment measured was 4,35 x 10^{-11} emu. As expected, the 2800 nm particles have higher magnetic moment saturation and also higher magnetic moments for a certain value of magnetic field than those obtained by the 50 nm particles.

According with the values measured in VSM for the magnetic moment of a particle, sensor output simulations for particles detection was performed by a colleague at INESC-MN, using the MAPLESOFT 12 software.

The parameters used for simulations are described below:

Table 3.2 Simulations of the average magnetic field sensed by the sensor relative to position of the MNP at a certain height (z).

Sensor dimensions	Sensor sensitivity	Bias current	MNP diameter	Magnetic moment at ~150 Oe
100 µm x 3 µm	0.39 Ohm/Oe	1 mA	50 nm; 2800 nm	1,34 x 10^{-15} emu (50 nm) 4,35 x 10^{-11} emu (2800 nm)

To analyse the magnetic field along x-direction of a 50 nm particle, simulations were developed for different heights relative to the sensor sensing layer surface: [1, 2, 3, 4, 6, 8, 10, 15, 20] µm. Figure 3.39c) depicts the results.

To understand the effects of magnetic moment/size of nanoparticles in SV voltage output, simulations were developed for two different sizes of nanoparticles: 2800 nm and 50 nm. Figure 3.39a) and Figure 3.39b) depict the results.

Table 3.3 Simulations of the voltage output measured by the sensor relative to position of the MNP at a certain height (z).

d (nm)	m (emu)	ΔV (µV) z=1µm	ΔV (µV) z=10µm
50	1.47x10^{-15}	3.30x10^{-03}	7.33x10^{-05}
2800	4.32x10^{-11}	51.18	2.17

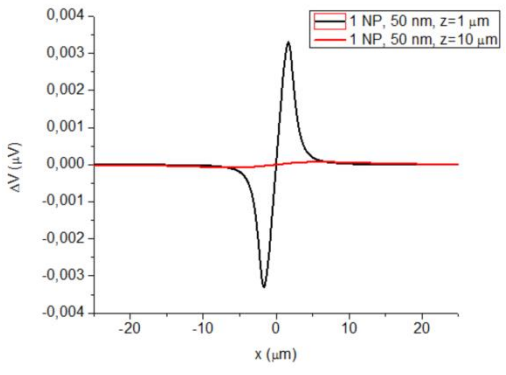

a)

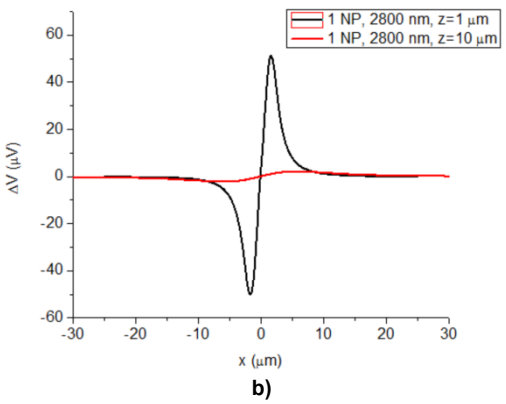

b)

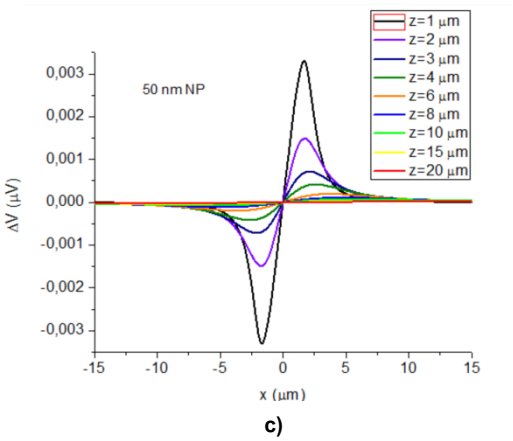

Figure 3.39 Simulation of the average of the magnetic field sensed by the sensor relative to position of the MNP over distance from the sensor. a) Magnetic field along x-direction of a 50nm particle at height z=1 and z=10; b) Magnetic field along x-direction of a 2800nm particle at height=1 and 10; c) Magnetic field along x-direction of a 50nm particle at different heights. These simulations were permormed using the MAPLESOFT 12 software.

Figure 3.39 shows some results of simulations performed for the variation of the magnetic field measured by the sensor as the particle flows over the length of the sensor and along its width. It can be observed that the higher the particle flows along the channels the lower is the magnetic field intensity and lower the output signal.

Note that at 10 µm distance between the MNP and the sensor, the output signal from 50nm MNP is $7{,}14 \times 10^{-5}$ µV and the value obtained for 2800nm is around 2 µV, Figure 3.39 a) and b) and Table 3.3.

When observing the values obtained for the signal voltage output of a 50nm particle, Figure 3.39c), it can be concluded that is not possible the detection of a 50nm single bead, even when the particle flows 1 µm distance to the sensor.

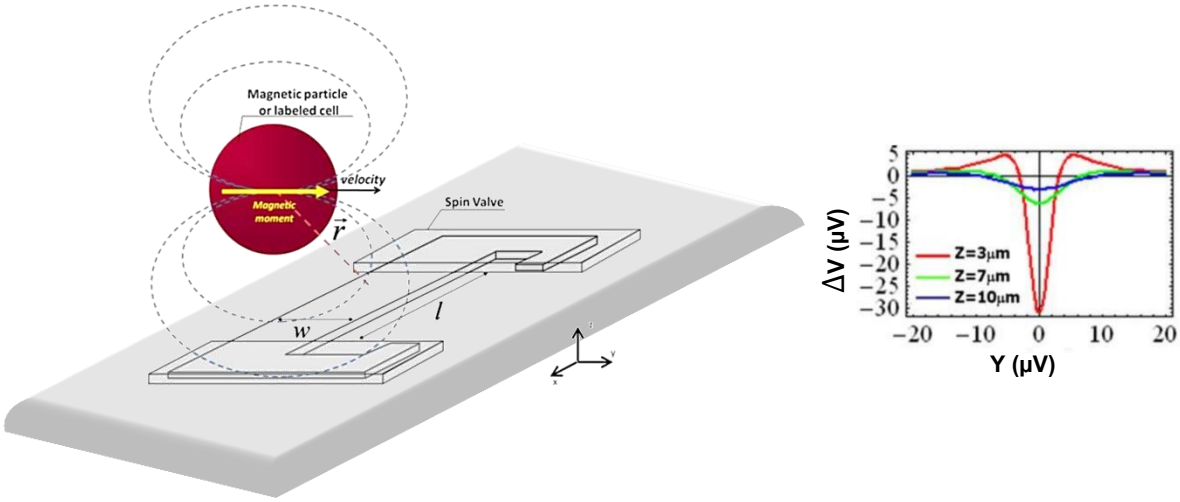

Figure 3.40 Detection schematics (not to scale) of a magnetically particle, parallel magnetized, flowing over a SV sensor. The graphic represents an example of a simulated signal for 5 µm diameter cells, labelled with N= 2880 nanoparticles, parallel magnetized, at different heights [3, 7, 10] µm l. Adapted from [10].

As could be expected, in each flow, a large number of MNPs are involved. Consequently, the average magnetic field sensed by the sensor in each instant is given by the sum of the sensed magnetic field of all MNPs travelling over the sensor.

Another important detail consists that it was assumed that the MNPs travelled with a constant height relative to the sensor surface and in a straight direction assumed at the centre of the sensor. In fact, the MNPs may be suffering rotation due the flow and it will have influence on the observed signal peak shape, Figure 3.40. For parallel magnetization, the average fringe field has a polar configuration.

Chapter 4

Biochip Platform

4.1 First Platform

The first design, fabrication and microfluidic integration of the biochip was already described in section 3.1, and the resulting mask is presented in the Figure 4.41.

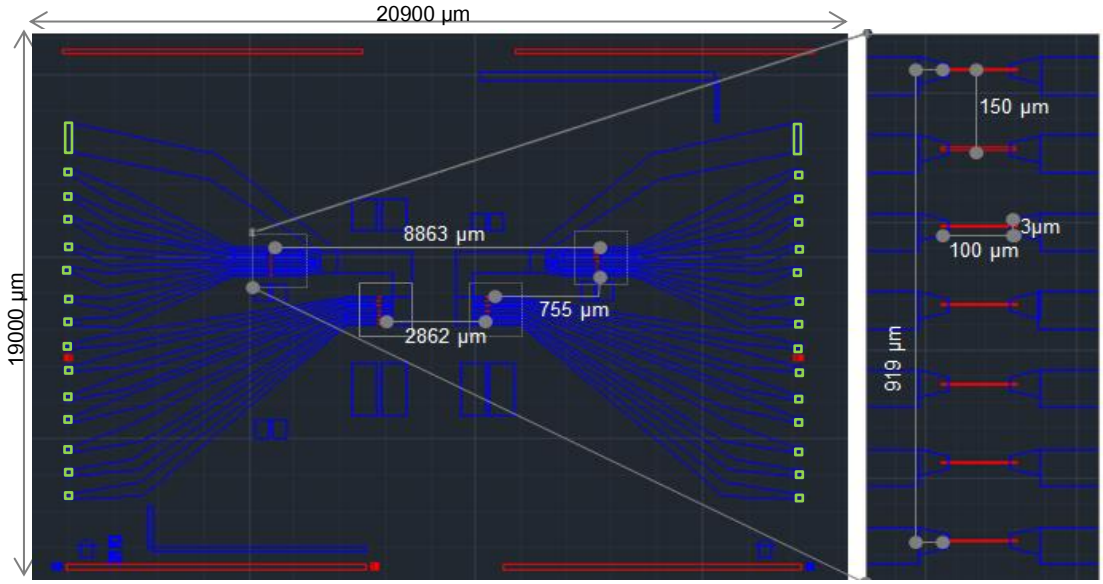

Figure 4.41 Detailed design of the biochip mask in AutoCad®: chip array of 28 SVs is displayed in red, vertically in the centre of the chip, the contact leads are presented in blue lines and the frame for electrical contact at the end of each contact leads displayed in green lines.

In Figure 4.42a) and 4.42b) is represented the strategy used, in the previous platform developed by C. Duarte [4], to place the permanent magnet in the PCB. It is glued below the PCB with the SV chip. The permanent magnet used is composed of Neodymium, N35, nickel-plated and it sizes 20 x 10 x 1 mm, having 8,83 N of strength and a residual magnetic field of 1,17 T-1,21 T.

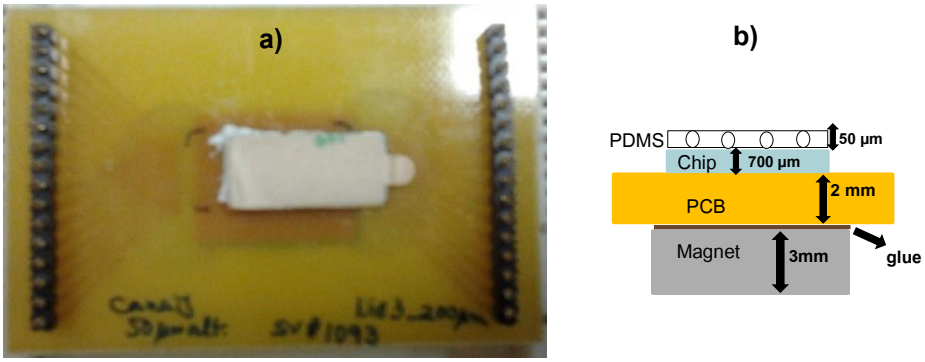

Figure 4.42 a) Assembly of the Biochip with the magnet, that is glue on the PCB; b) Schematics of the platform, showing the thicknesses of the different components of the platform.

4.1.1 Electrical Transport Characterization of SV sensors with the permanent magnet

In order to characterize the change of resistance as a function of the external field, the measurement setup previously described in section 3.3 was employed.

The platform chip/permanent magnet that was subjected to electronic transport characterization with bias current of 1 mA is illustrated in Figure 4.42.

Figure 4.43a) shows the results of transfer curves of 100 x 30 μm^2 sensors without the permanent magnet below and Figure 4.43b) when a magnet is placed below the chip. All sensors were characterized and the results for two sensors of each array are shown in the Figure 4.43.

The measurement setup and conditions were previously described in section 3.3

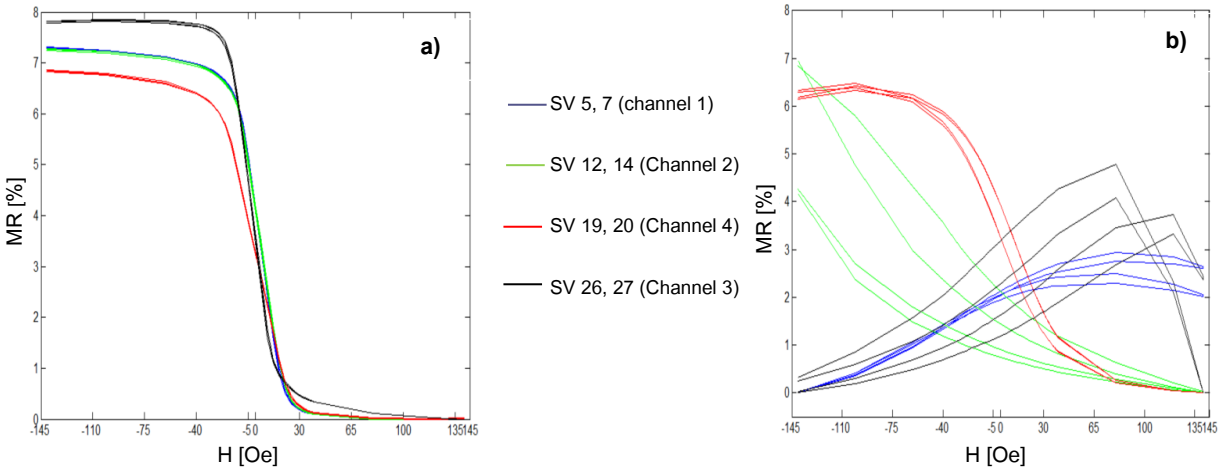

Figure 4.43 MR curve of the SV a) without a permanent magnet below; b) assembled with the permanent magnet.

It is important to notice that the calibration of the magnet position was performed by reading the resistance of one SV while moving the magnet, which is a time consuming process. When the position where the resistance value of a SV suffers less variation was achieved (in this case SV 19 and SV 20, Figure 4.43, b)) for the zero field conditions, the magnet was fixed. However, when characterizing all the sensors it was verified that only these two SVs were not affected by the magnet. For a total of 28 measured sensors, a low MR ratio was obtained and was observed a nonlinearity in the region centred at the zero applied field.

Figure 4.44 shows a schematic of the linearized transfer curve for the underbiased SV and a properly biased sensor.

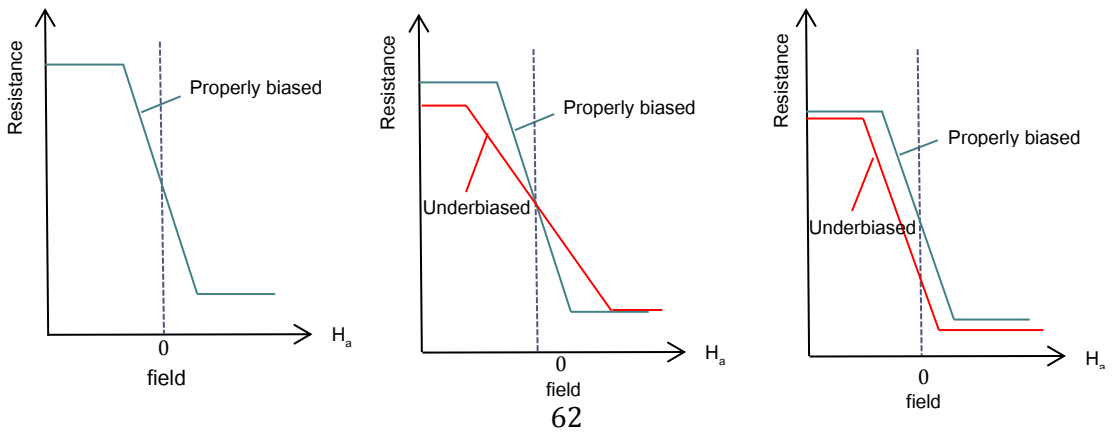

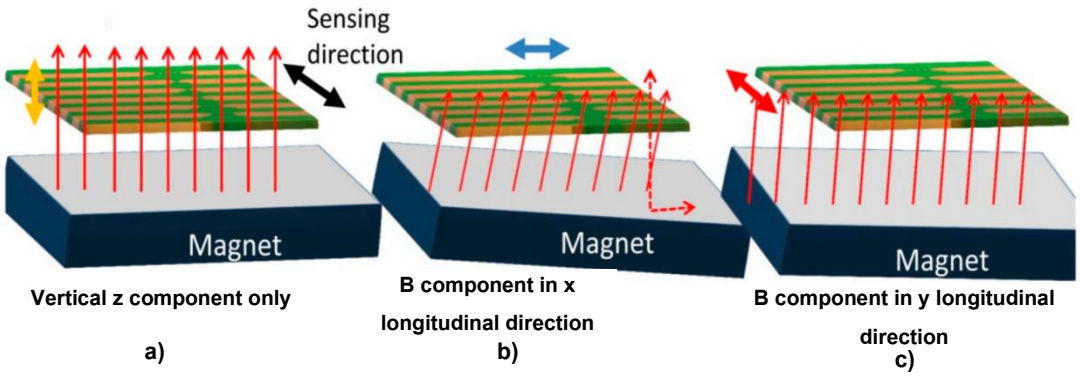

Figure 4.44 Schematics of the impact of the sensor response of each magnetic field component, set by magnet position transfer curves [4].

If a well alignment between magnet and sensors is achieved, the sensor transfer curve should be centred around zero external fields, as it evidenced in Figure 4.44a), what means values of H_f near zero, with maximum sensitivity. A slight tilt of the magnet can create fields in the y direction, Figure 4.44c), shifting the sensor transfer curve, and resulting in bigger values of H_f, and/or fields in x direction, Figure 4.44b), which decrease the sensor sensitivity.

From the Figures 4.43 and 4.44, it can be concluded that the magnet placed below the sensor is changing the magnetization direction of the PL and FL, $\theta^{PL} \neq \frac{\pi}{2}$ and $\theta^{FL} \neq 0$, so it is not possible to achieve a linear behaviour of the sensor.

To understand the conditions required for a MR device to have a linear behaviour, it can be considered the energy balance of the sensing layer composing the following structure “PL/Spacer/FL” where the system is considered to be under the influence of an external field low enough for the PL to have its magnetization fixed.

When no external field is applied the magnetization of the PL and FL have a perpendicular direction between each other, as it is represented in Figure 4.45.

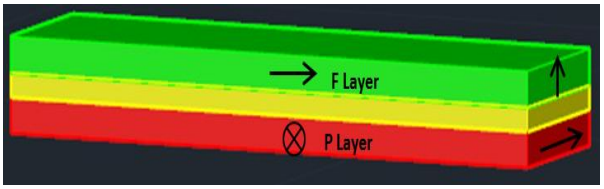

Figure 4.45 Schematics of the free and pinned layer magnetizations in the absence of a magnetic field.

When the magnet was placed below the chip, there are perpendicular magnetic field components (z direction), which do not affect the magnetization of the magnetic layers, but also field components in x and y directions, which rotate the FL magnetization.

This consisted in a motivation for developing a second platform in which the magnet does not affect the sensors.

4.2 Design and Development of the Second Platform

As mentioned previously, a new platform was designed to reduce problems of non-uniformity of the permanent magnet which affects the SV behaviour.

The strength of a magnetic field drops off exponentially over distance, so it is possible to decrease the x and y field components by increasing the distance between the chip and the permanent magnet.

Pursuing the idea of a hand held device, the whole system was designed to be assembled in an external packing based on plastic capsules pressed together by means of screws (Figure 4.46).

This novel packaging was designed by a computer design tool (AutoCad®) and fabricated in polylactic acid (PLA) using a 3D Printer. The combination of these two tools provides a versatile, easy and cheap way to fabricate different package prototypes.

The bottom capsule acts as a support for the permanent magnet, whereas the top one acts as a support for the printed circuit board (PCB) with the sensor.

Another permanent magnet block (dimensions 20 x 20 x 03 mm^3, NdFeB, Supermagnete, Gottmadingen, Germany) with residual magnetic field of 1,32 T-1,37 T was chosen in order to achieve a larger area of uniformity.

The PCB contains metal pins, which are the connection between the electrodes for the sensor and the pads of the PCB. The pieces of the packing are aligned and held together with plastic screws, allowing the positioning of the permanent magnet at a certain distance of the PCB with the sensor and also an easy replacement of the device. The package allows the user to insert the sample through external flexible tubes with a simple syringe.

Figure 4.46b), depicts the whole assembly of the second prototype.

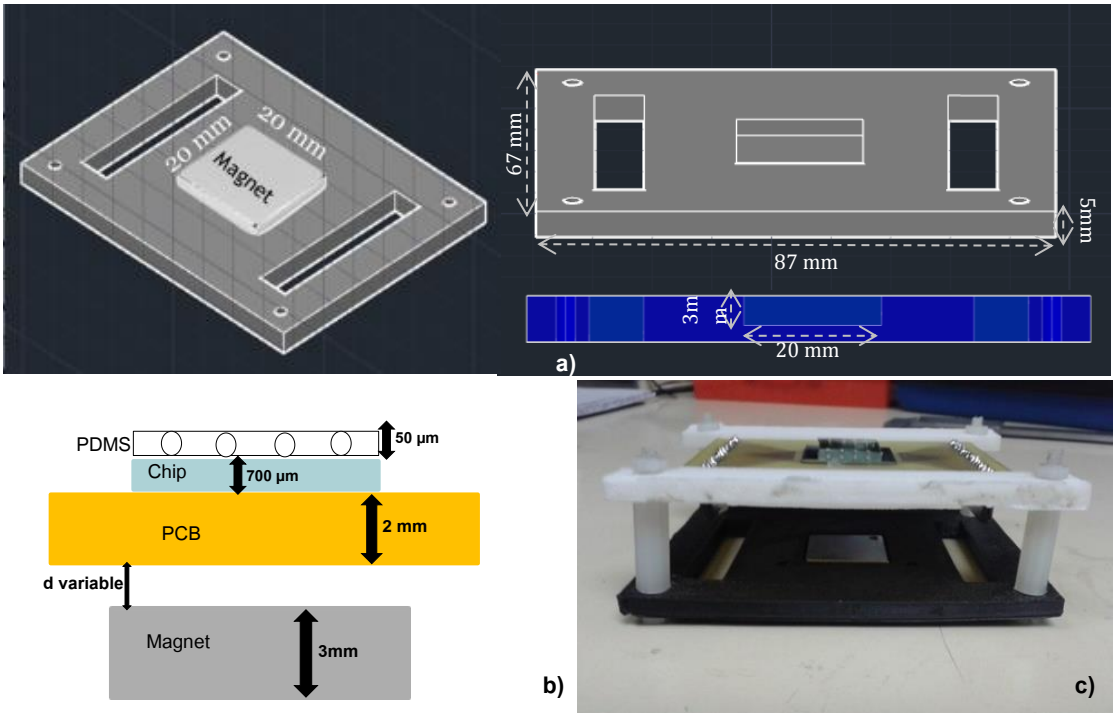

Figure 4.46 a) AutoCad® design of the support platform; b) Schematics of the full assembled integrated platform; c) Fotography of the full assembled integrated platform with the biochip and the squared permanent magnet.

4.2.1 Electrical Transport Characterization of SV sensors with the permanent magnet

As the SV are only sensitive to in-plane fields (x and y components), if well aligned with the area of the magnet where these fields are lower than 10 Oe, the magnet will not affect the sensitivity of the sensor.

The chip used was the same described in section 4.1.The impact of the magnet positioning on the sensor transfer curve is illustrated in Figure 4.47.

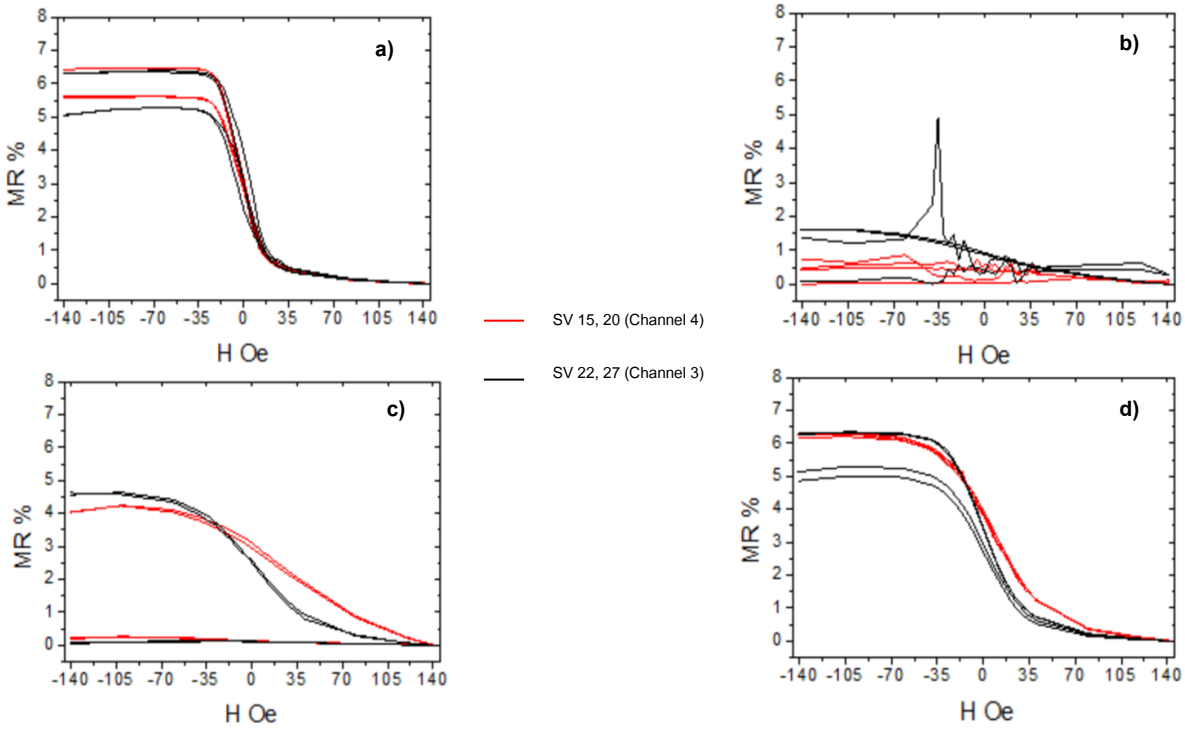

Figure 4.47 MR curve of the SV a) without a permanent magnet below; b) assembled with the permanent magnet at 0,5 cm distance; c) assembled with the permanent magnet at 1 cm distance; d) assembled with the permanent magnet at 2 cm distance.

Table 4.4 Important parameters taken from SVs transport characterization

	Number of SV	MR [%]	Rmin [Ω]	Rmax [Ω]	H_f [Oe]	H_c [Oe]	S [%/Oe]
No Magnet	9	6,21±0,4	386±19,2	410±19,1	-0,92±1,1	1,77±1,0	-0,18±0,1
Magnet at 0.5 cm	8	1,75±1,4	511±236,5	520±239,1	-	-	-
Magnet at 1 cm	8	3,24±2,4	497±224,9	510±219,3	2,67±21,6	2,98±3,6	-0,11± 0,1
Magnet at 2cm	8	5,71±1,4	386±18,3	407±18,7	-3,47±8,1	0,48±0,4	-0,13±0,1

Figure 4.47a) shows a representative example of four sensors transfer curves measured without the magnet above.

Figure 4.47b) shows the results for the same array of sensors but when a magnet is placed at 0,5 cm distance from the sensors. At this distance, the in-plane fields are very high and change the orientation of the magnetization of the FL and also the PL.

Figure 4.47c) presents the sensors response when a magnet is placed at 1 cm distance. It was expected more uniformity of perpendicular fields at this distance and lower in-plane fields. However observing the transfer curves it can be seen a significant decrease in sensitivity and a huge shifting of the curves to high values of MR at zero fields. This means that in-plane fields are high and rotate the FL magnetization.

Figure 4.47 d) shows the results when a magnet is placed at 2 cm distance. It is observed higher values of sensitivity and good values of MR. However, at this distance, I expected, a more uniform magnetic perpendicular fields and longitudinal fields in x and y directions. As it can be seen by the obtained transfer curves, the permanent magnet is degrading the behaviour of the sensors.

Comparing the results from different distances between the magnet and the chip, it can be concluded that the magnet placed at 2 cm distance from the chip corresponds to a better sensor response.

These results were the starting point to the development of a magnetic scanning platform to find the area of the permanent magnet where the x longitudinal field components are as lower as possible in order to position the magnet with a minimum impact on the sensor response.

4.3 Development of a Magnetic Scanning Platform

As mentioned previously, a module with a Hall Effect sensor, showed in Figure 4.48, was developed and assembled in a magnetic scanning platform.

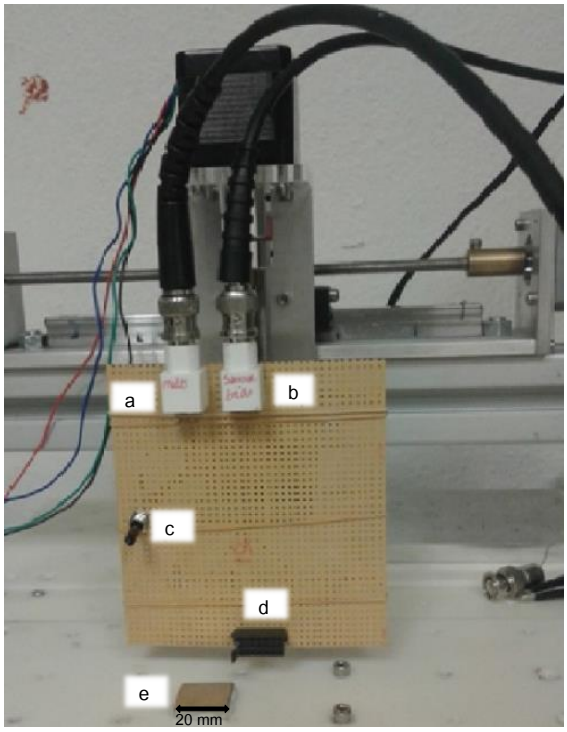

a. Multimeter connection
b. Sensor bias connection
c. Switch
d. Hall Effect Sensor
e. Permanent magnet

Figure 4.48 Magnetic scanning platform.

The platform consists of: a Hall Effect sensor (SS495A Series, Honeywell), d, to detect the variation in the magnetic field, a switch bottom, c, to be able to change between perpendicular field or x longitudinal direction field detection, and two BMC connectors for the bias, b, and multimeter, a, connections. The sensor bias is performed by an Agilent 32310A function generator, being the operating voltage 5V, while the output is read by a 6 1/2 digits digital multimeter HP34401A.

It is important to notice that this sensor will be used due to the need to measure a wide range of magnetic fields, which the MR sensors cannot provide.

The Hall Effect is a property that conductive materials exhibit when a magnetic field perpendicular to the current flow is applied. When it occurs, a voltage is generated and it is called Hall voltage. This voltage is perpendicular and proportional to the magnetic field and current applied [16], Figure 4.49.

When a beam of charged particles passes through a magnetic field, forces act on the particles and the beam is deflected from a straight path. The flow of electrons through a conductor is a beam of charged particles. When a conductor is placed in a magnetic field perpendicular to the direction of the electrons, they will be deflected from a straight path. Therefore, an accumulation of electrons will occur on one site wall of the conductor leading to a ΔV between the two sidewalls. The voltage between these sidewalls is called Hall voltage.

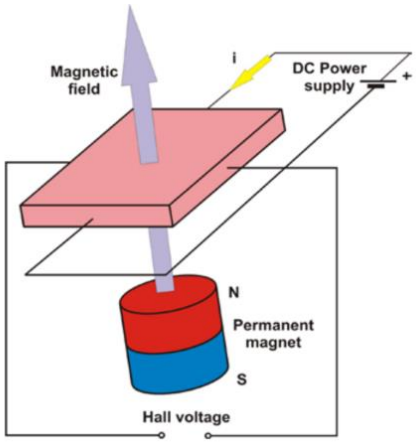

Figure 4.49 Schematics of an Hall Effect sensor principle [16].

Linear Hall Effect sensors give a continuous voltage output that increases as the strength of the magnetic field increases until it begins to saturate by the limits imposed on it by the power supply [16].

The Hall Effect sensor SS495A under test is a linear Hall Effect sensor of the type ratiometric, which means that it has a quiescent output voltage that is half of the supply voltage: Vsensor [H=0] ~ $\frac{5V}{2}$. This sensor has typically magnetic range -67 mT to 67 mT (-670 Oe to 670 Oe) and a sensitivity around 0,033 V/Oe, while the response time is better than 3 µs [17].

During the measurement, the magnet passes above the sensor and its lines of magnetic force act on the chip, Figure 4.50.

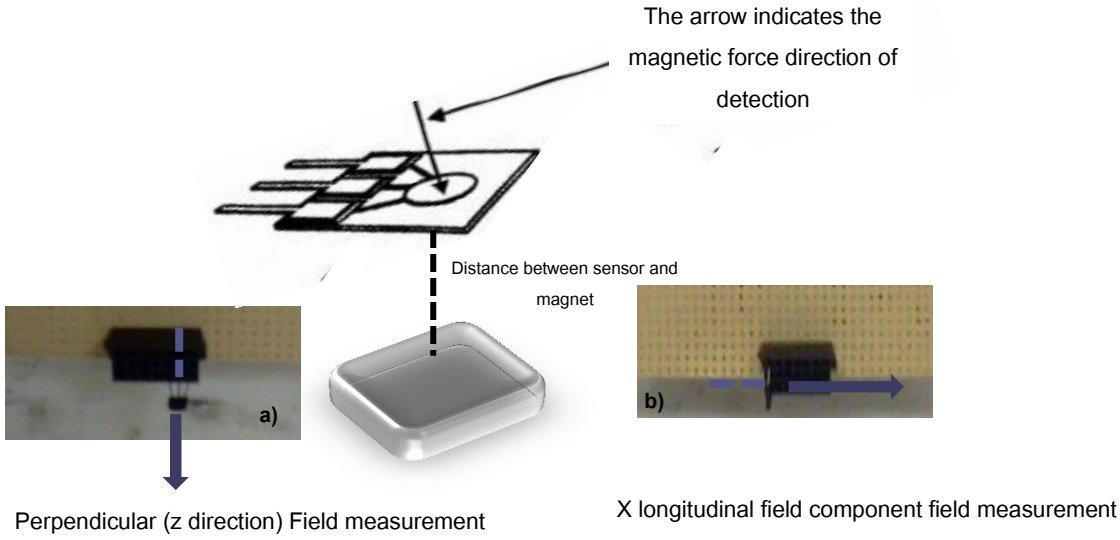

Figure 4.50 Use of an Hall Effect sensor for permanent magnet measurement of: perpendicular and in-plane magnetic fields. The sensor passes above the permanent magnet and their lines of force act on the chip.

The following results were obtained when performing tests with the same permanent magnet (20 x 20 x 03 mm^3, NdFeB Supermagnete, from Gottmadingen, Germany) with a residual magnetic field of 1,32 T - 1,37 T , Figure 4.51.

A homemade LabVIEW program was developed by colleagues from INESC-MN and INESC-ID, to register each measurement for this application. The Figure 4.51 shows schematics of the scanning for these tests.

Permanent magnet is placed on a XY automated positioning table system using stepper motors and the sensor is placed on the metallic structure with micrometric screw adjusting mechanism z axis.

The first step consists on measuring the voltage when applying no magnetic field, $V_{H=0}$, in order to cancel the offset voltage of the Hall Effect sensor.

Measurements were performed along the total area of the permanent magnet.

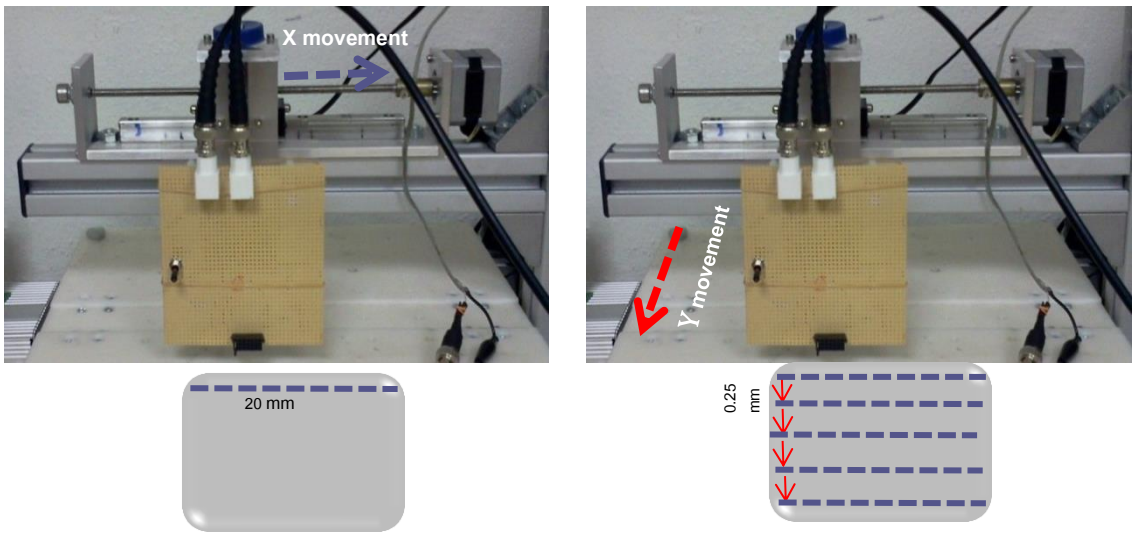

Figure 4.51 Schematics of the measurements of the permanent magnet.

In scanning measurements were used as parameters:

i. x resolution and y resolution of 0,25 mm, a compromise between a good resolution and a reasonable time of scanning;

ii. x span and y span of 20 mm, which corresponds to the dimensions of the magnet.

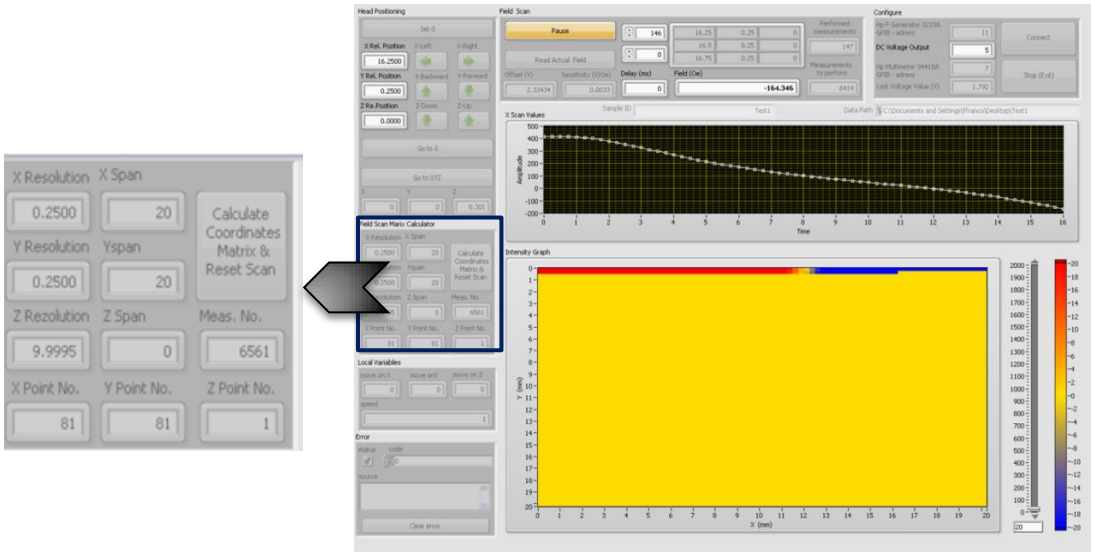

Figure 4.52 LabView softawe developed for the permanent magnet scanning masurements.

4.3.1 Magnetic Scanning Analysis

In magnetic scanning, the relevant x and z components of magnetic field exerted by the magnet on the sensor were measured and shown in Figure 4.53, presenting the three distances tested between the sensor and the permanent magnet: 0,5 cm, 1 cm, and 2 cm.

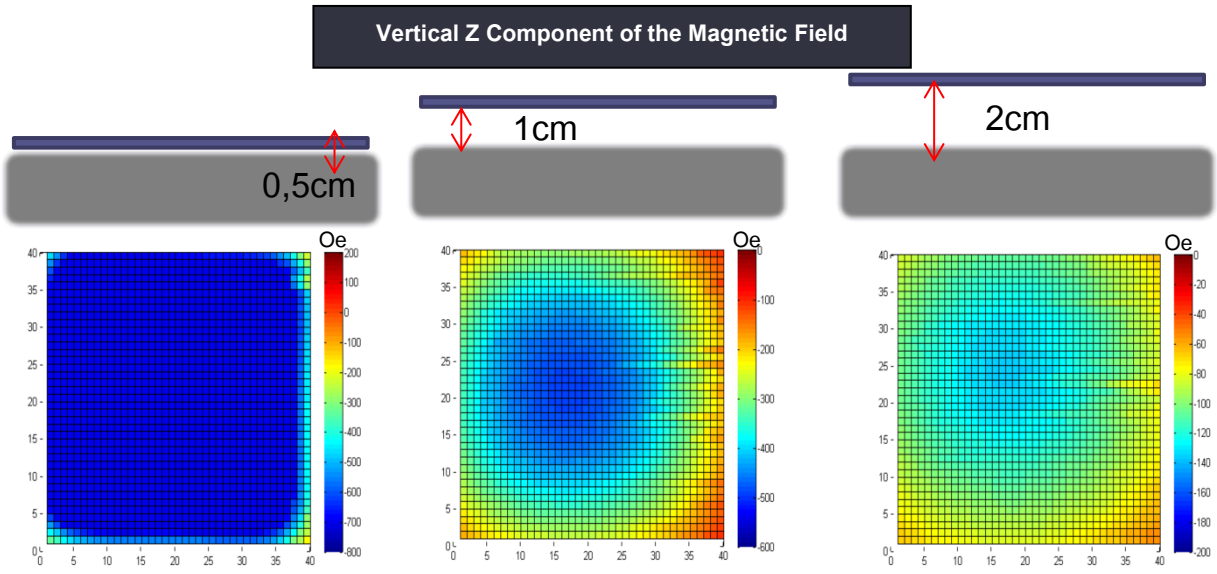

a) 0,5 cm distance magnet/sensor b) 1 cm distance magnet/sensor c) 2 cm distance magnet/sensor

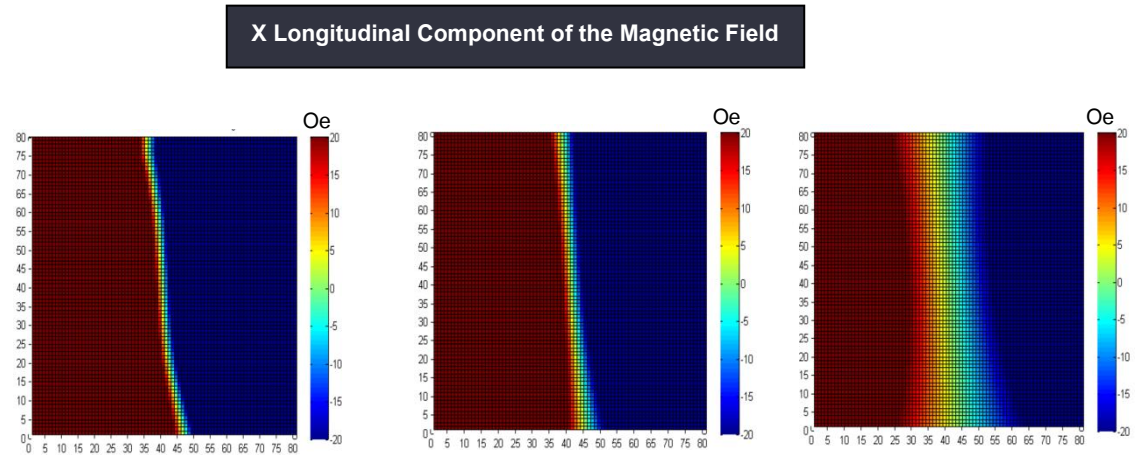

d) 0,5 cm distance magnet/sensor e) 1 cm distance magnet/sensor f) 2 cm distance magnet/sensor

Figure 4.53 Perpendicular (a), b), c)) and Longitudinal (d), e), f)) scan results from the surface of the permanent magnet at different heights from the sensor.

The values obtained from the magnetic scanning for the magnet at 0,5 cm distance from the sensor, show:

i. A majority of perpendicular fields in a range between -700 Oe and -600 Oe, Figure 4.53a);
ii. Little spots distributed in the middle of the magnet, where the x longitudinal component of the field is lower than 10 Oe, as illustrated in Figure 4.53 d).

It can be concluded that it is quite impossible to set the magnet below the PCB at 0,5 cm distanc..

The results obtained for magnet at a distance of 1 cm from the sensor showed:

i. Perpendicular field in a range between -500 Oe and -300 Oe, Figure 4.53 b);
ii. An area of 0,25 x 9,25 mm where the x longitudinal component of the field $\leq$10 Oe.

When the permanent magnet is placed at a distance of 2cm from the sensor:

i. The Perpendicular fields vary between -150 Oe and -100 Oe, Figure 4.53 c);
ii. It is possible to achieve an area of 2,75 x 20 mm, where x longitudinal component of the field is lower than $\leq$ 10 Oe.

It can be concluded that the best option is to place the magnet at 2 cm distance from the sensor.

Another conclusion that can be taken from this study is the importance of changing the design of the chip in order to place the four sensor arrays along a line to be easier their alignment with the area of the magnet where the values of lower x longitudinal fields were found.

4.3.2 Microfluidic Tests performed in the Platform with the permanent magnet

The clogging of channels is a problem specially observed in bead-based microfluidic assays [18].

The interaction of the MNPs with the permanent magnet was also experimentally studied to evaluate the attraction effect of the permanent magnet over 2800 nm MNPs that flow inside the microchannel. The attraction of the beads was observed under a microscope and periodic images were taken, Figure 4.54.

The 2800 nm diameter sized magnetic beads were used to allow optical verification of the particle position with respect to the sensor using a visible light microscopy. The experimental setup is composed by the platform with the chip and the permanent magnet above, a syringe pump to inject the fluid with beads though the microchannel and a microscope.

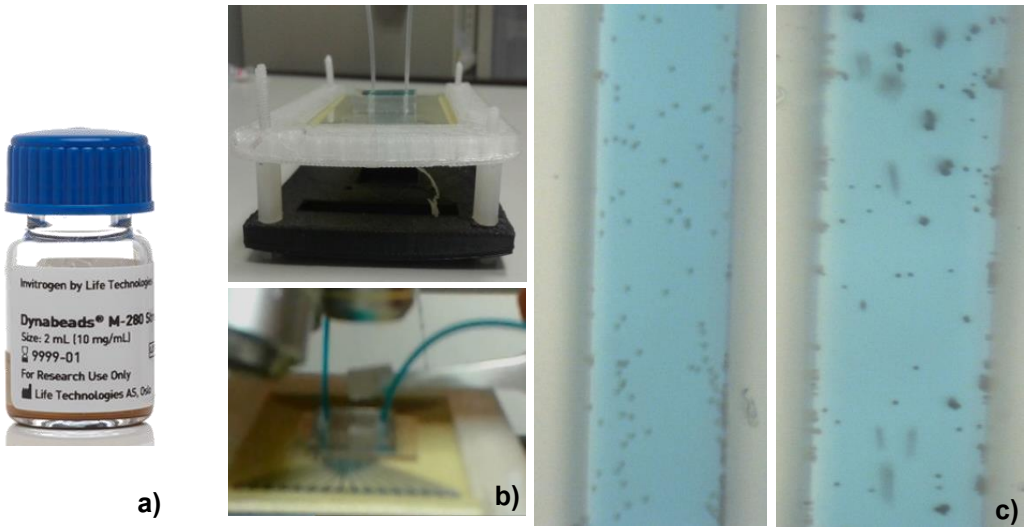

Figure 4.54 a) Dynabeads® M-280; Photography of: b) experimental setup; c) a section of the microchannel where a sample that contains water, magnetic particles and blue dye can be observed under a microscope using a magnification of 20x.

It was verified that the permanent magnet does not attract the particles that flow inside the microchannel, which means that the x and y components of the magnetic field are not strong enough to change the direction of the particles. During these experiments, it was also possible to observe beads aggregates.

No significant attachment of nanoparticles to PDMS or the sensors was observed during sample flow.

4.4 Second Spin Valve Chip Design

4.4.1 Chip Re-Design

Based on the previous chip, another design was developed in order to have the array of sensors positioned in line, above the area where the z component of the magnetic field is more uniform.

The biochip comprises 4 areas with four columns of 7 sensors. The sensors of the same column are separated from each other by 150 µm, and sensors from different areas are separated by 2870 µm.

Figure 4.55 presents an illustration in AutoCad® of the biochip design (A). One group of seven sensors (red) is zoomed in (C).

Colours of CAD masks represent different layers: spin valves (red), electrical contacts (blue) and pad contacts (green).

The sensors from the two areas at right have the same common contact, which corresponds to the top right (green), and the two areas at left side have the same common contact to the top left (green), rectangular pad. All the other square pads (green) are used to address each sensor, Figure 4.55 A.

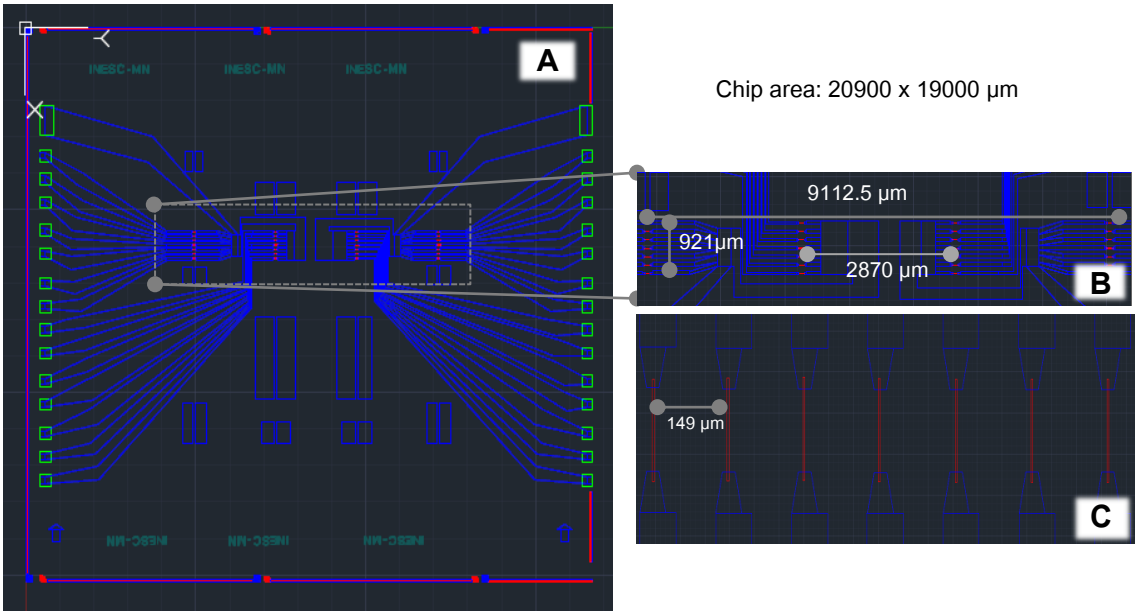

Figure 4.55 Top view of the biochip in the AutoCad® mask (A); Four arrays of spin valve sensors (B); One group of spin valve sensors (C).

The procedures which were followed to develop the new chip were the same described in chapter 3.

4.4.1.1 Electrical Transport Characterization with the Permanent Magnet

The 28 sensor's transfer curves were characterized.

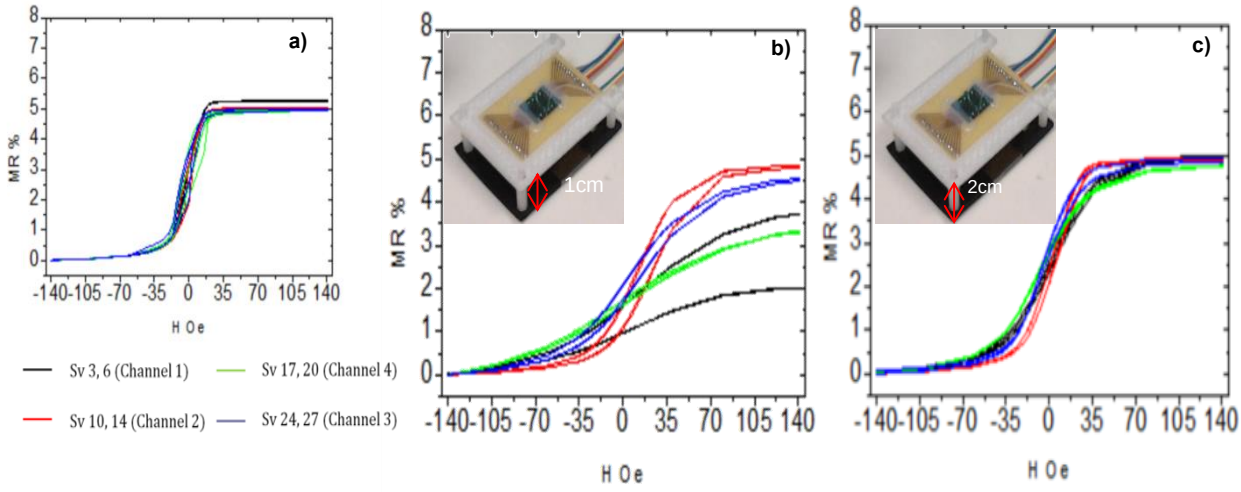

Figure 4.56 MR curve of the SVs a) without a permanent magnet below; b) assembled with the permanent magnet at 1 cm distance; c) assembled with the permanent magnet at 2 cm distance.

A summary of the dispersion obtained over the 28 sensors measured (Figure 4.56 a)) is depicted in Table 4.5.

Table 4.5 Important parameters taken from the MR curve of the SVs without a permanent magnet below.

	Number of SV	MR [%]	Rmin [Ω]	Rmax [Ω]	H_f [Oe]	H_c [Oe]	S [%/Oe]
Channel 1	7	5,26±0,01	424,5±13,20	446,9±13,92	-3,48±0,52	0,82±0,37	0,196±0,023
Channel 2	7	4,99±0,07	443,95±13,03	466,09±13,64	-1,58±1,94	3,07±1,6	0,230±0,039
Channel 3	7	4,94±0,09	413,3±49,06	433,7±51,79	-2,66±2,85	3,67±1,23	0,22± 0,054
Channel 4	7	4,99±0,07	443,95±13,03	451,13±11,04	-3,58±1,9	4,67±1,3	0,244±0,056

The chip was assembled in the platform described in section 5.2 and the permanent magnet was placed below at 1 cm. Sensors transfer curves were characterized (Figure 4.56 b)) and a summary of the dispersion obtained over the 28 sensors measured on the chip is depicted in Table 4.6.

Table 4.6 Important parameters taken the MR curve of the SVs with a permanent magnet below at 1 cm.

	Number of SV	MR [%]	Rmin [Ω]	Rmax [Ω]	H_f [Oe]	H_c [Oe]	S [%/Oe]
Channel 1	7	3,62±0,71	425 ±12,16	440 ±12,26	3,99 ±8,82	0,44±0,11	0,141 ±0,03
Channel 2	7	4,78±0,04	446 ±13,46	467 ±14,14	16,27 ±4,79	0,63±0,15	-0,12 ±0,01
Channel 3	7	4,38±0,14	415,6 ±52,15	433,87 ±54,81	8,59 ±4,14	0,77±0,52	0,17 ± 0,02
Channel 4	6	3,41±0,31	418 ±35,86	432,12 ±36,02	-0,61 ±4,72	0,37±0,24	-0,12 ±0,01

Then the permanent magnet was placed below at 2 cm (Figure 4.56 c)), and its results are summarized in the table 4.7.

Table 4.7 Important parameters taken the MR curve of the SVs with a permanent magnet below at 2 cm.

	Number of SV	MR [%]	Rmin [Ω]	Rmax [Ω]	H_f [Oe]	H_c [Oe]	S [%/Oe]
Channel 1	4	4,98±0,03	424±13,88	445±14,64	-0,22±1,64	0,47±0,31	0,110±0,009
Channel 2	4	4,94±0,06	445,5±11,57	467,5±12,06	-1,28±1,75	0,19±0,12	0,093±0,003
Channel 3	4	4,84±0,05	419,8±45,32	440,12±47,63	2,03±4,24	0,28±0,19	0,083± 0,006
Channel 4	4	4,75±0,02	445,04±8,33	466,17±8,76	7,8±0,94	0,25±0,19	0,091±0,0015

Comparing these results with the previous ones (section 4.2.2), the new pattern brought improvements such as allowing that the 28 sensors stay unaffected by the presence of the magnet below.

From a practical point of view, the alignment of the permanent magnet with the chip will never be perfect and some unwanted components in x directions and y directions are present.

Table 4.7 shows the sensors output parameters from MR transfer curves, and it is possible to verify that for this platform the sensors minimum resistance varies between 419 Ω and 445 Ω, the maximum resistance varies between 440 Ω and 467 Ω, leading to an effective device magnetoresistance that vary between 4,75% e 4,98%. Notice that the sensors are linear in excitation field range of ±35 Oe with a corresponding sensitivity that varies between 0,08%/Oe and 0,1%/Oe.

In the following graphics, Figure 4.57, it can be compared the impact of the positioning of the magnet in sensors transfer curve.

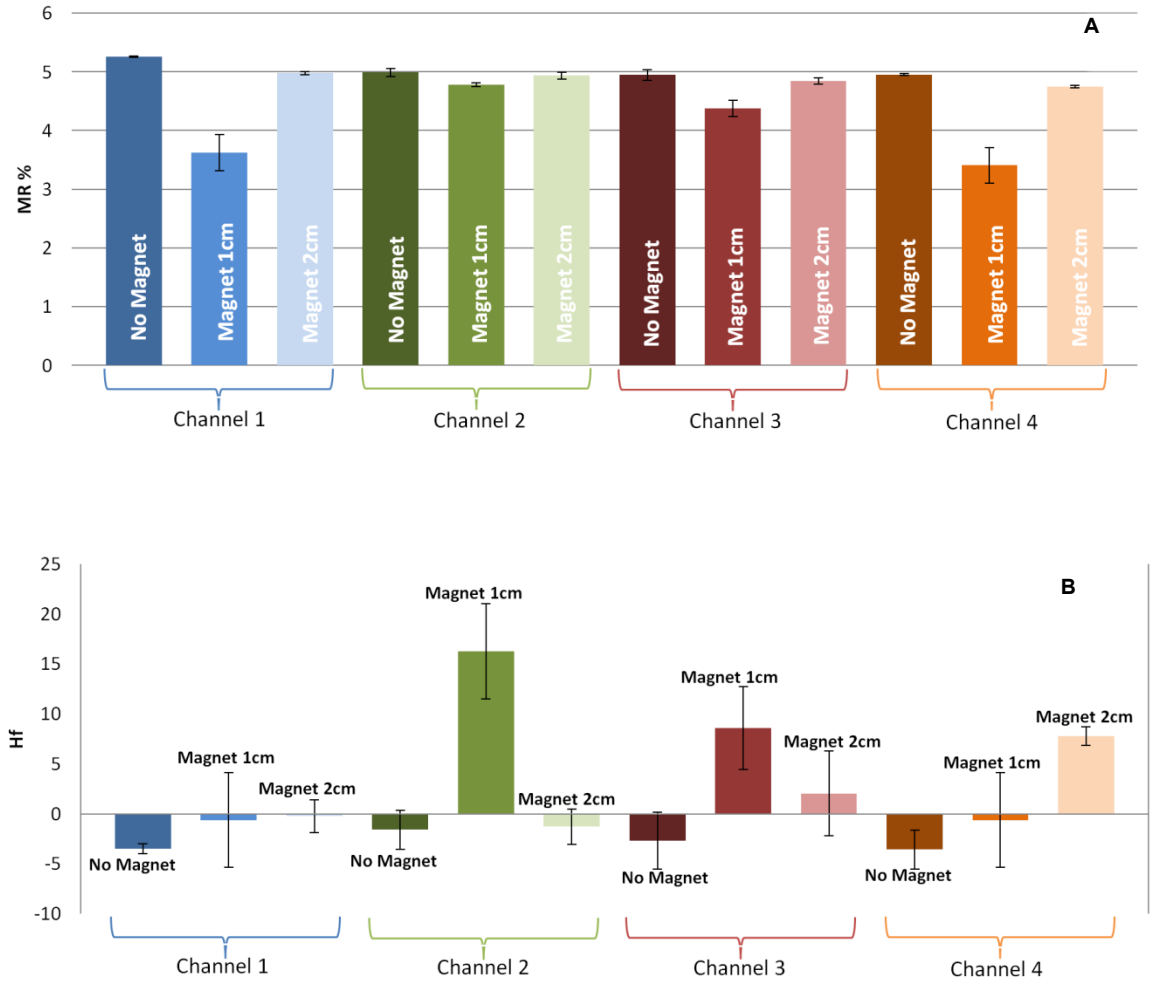

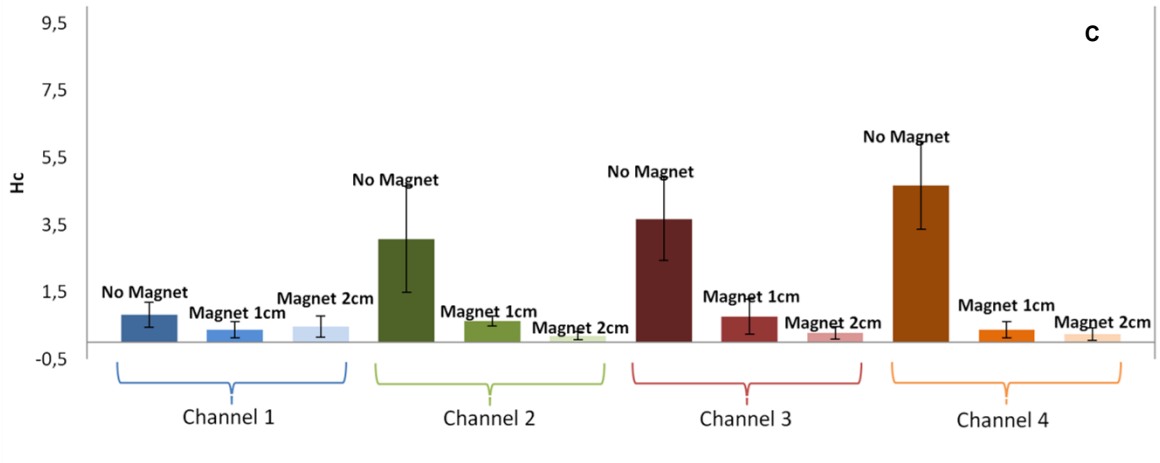

Figure 4.57 Representation of the impact of positioning of magnet in sensors transfer curve parameters: A. Magnetoresistivity; B. Effective coupling field; C. Coercive field.

Through Figure 4.57A, and comparison of Tables 4.5 and 4.7, it can be observed that the values of MR [%] obtained when the magnet is positioned at 2 cm below the chip are quite similar with the ones obtained without the presence of the permanent magnet. At this distance, the in plane field components of the permanent magnet are lower and not affect the sensor response, significantly.

As it can be observed in Table 4.5 and its schematization in Figure 4.57B, the sensors have a considerable deviation of the linear region (higher values of H_i), which could affect the sensor's performance.

Another interesting aspect is the fact that the permanent magnet promoted linear sensor behaviour, Figure 4.57C.

In order to obtain a linear magnet response, the FL magnetization must rotate coherently with the PL magnetization between the parallel and antiparallel states. In the absence of an external magnetic field, the PL magnetization direction is defined by setting the exchange coupling direction through annealing in an uniformly strong magnetic field. FL magnetization is defined in the transverse direction by shape anisotropy. When a perpendicular orientation between the FL and the PL magnetizations is not achieved, the sensor magnetic response exhibits discontinuities, Figure 4.58.

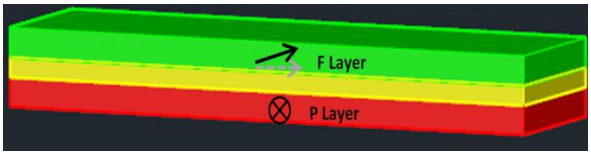

Figure 4.58 Schematics of a non perpendicular orientation between the F layer and P layer, which promote discontinuities in sensor magnetic response to an external magnetic field. F: Free; P: Pinned (P).

The non-perpendicular orientation between the FL and the PL magnetizations can be solved by the x longitudinal component of the magnetic field created by of the permanent magnet, which can rotate the magnetization of the FL in order to acquire an orientation perpendicular to PL magnetization, Figure 4.59.

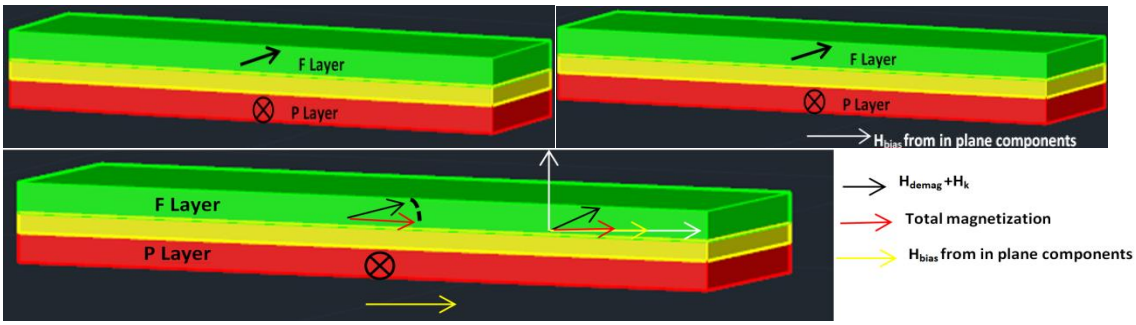

Figure 4.59 Schematics of the linearization of the sensor due to the presence of the permanent magnet. F: Free; P: Pinned (P).

As can be verified in Figure 4.57C, when the magnet is placed at 2 cm, in-plane field components of the permanent magnet shift the transfer curve and can suppress these effects reducing the coercivity, H_c. Comparing the Tables 4.5 and 4.7, and observing the Figure 4.57C, it is visible a reduction in H_c. On the other hand, a change in the slope of the transfer curve reduces the sensitivity of the SVs.

In the following paragraphs is performed an analysis of the first chip, whose design is show in Figure 4.41, versus the last chip, whose design is show in Figure 4.55. Transfer curves are in accordance with the developed magnetic scan.

In the figure below is represented the old mask (A) and also it is indicated the location of the SVs (B), whose transfer curves will be compared and discussed.

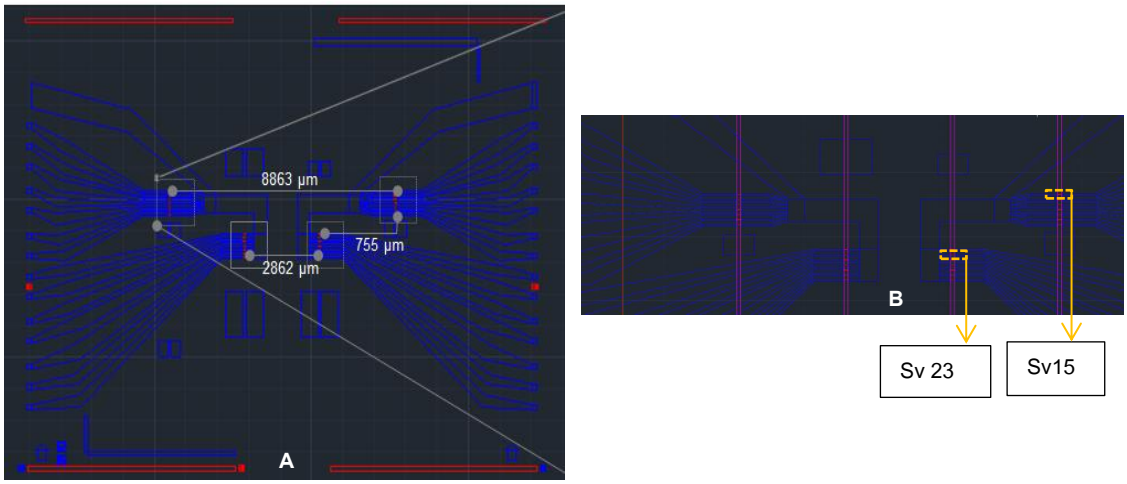

Figure 4.60 (A) AutoCAD® design of the chip; (B) Array of SVs is zoomed showing the location of SVs number 15 and 23, refered below.

As can be observed in Figure 4.60A, the area of the chip occupied by SVs is 8,8 x 1,655 mm.

The results obtained for magnet scanning at a distance of 1 cm from the sensor show an area of 0,25 x 9,25 mm where the in x component of the magnetic field is ≦10 Oe, value from which there is no change in the magnetization of the FL. However it is impossible to align the 28 sensors in this area.

The magnet placed at distance of 2 cm from the sensors allows to achieve an area of 2,75 x 20 mm with in plane fields ≦10 Oe, being possible to align more sensors, but not all of them.

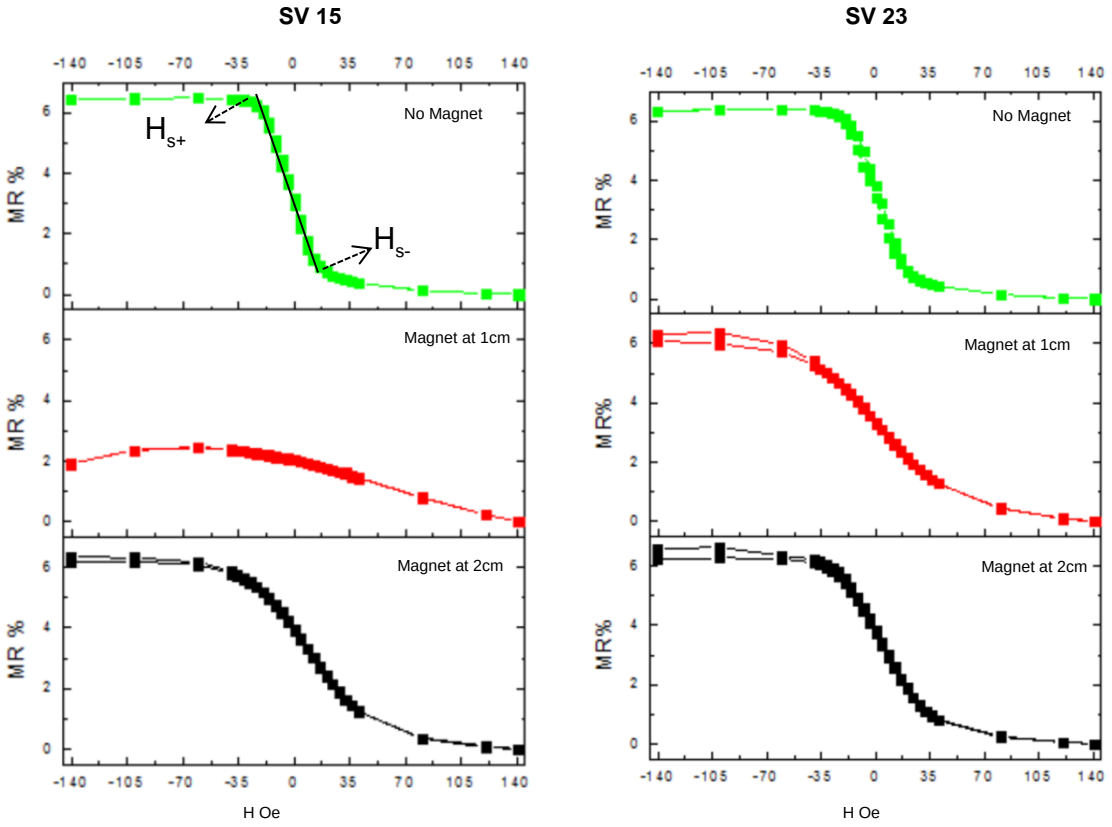

Figure 4.61 Tranfer curves of SV number 15 and 23 obtained when: a) there is no permanent magnet below; b) a permanent magnet is placed at 1 cm from the SVs; c) a permanent magnet is placed at 2cm below the SVs. The graphics show the influences on the tranfer curves caused by the permnent magnet presence below the sensors.

In fact, SV 23 is less affected by the in-plane fields, comparing to SV 15. This may be explained by the fact the SV 23 is located near the centre of the magnet, where there is an higher uniformity of the perpendicular field and lower values of in plane field. The analysis of saturation field (H_s) obtained for the same sensor when the magnet was placed at different distances and for different positions of the sensors in the chip is summarized in the Table 4.8.

H_S was calculated analysing the mean of H_{S+} and H_{S-} :

$$H_S = \frac{H_{S+} + H_{S-}}{2}. \qquad \text{Equation 8}$$

Table 4.8 Values obtain from the equation above, showing the impact of the contribution of the permanent magnet field components in saturation field sensors transfer curve.

Channel	Sv	Magnet distance [cm]	H_s[Oe]	$H^{external}$[Oe]
4	15	1	x	x
4	15	2	34	14
3	23	1	40	20
3	23	2	32	12

If there is no magnet placed below the sensors, $H_s = H_d^{FL}$ and its value is approximately 20 Oe. When the magnet is placed below the sensor, the value of H_s increased, and this may be explained by the fact that the permanent

magnet has a significant contribution for the total magnetization. This contribution can be determined by the equation:

$$\mathbf{H}^{\mathbf{external}} = \boldsymbol{H_s} - \mathbf{H}_{\mathbf{d}}^{\mathbf{FL}} \qquad \textbf{Equation 9}$$

For a permanent magnet placed at 1 cm (Figure 61B) the in-plane fields detected by sensors are higher than 20 Oe, but when the magnet is placed at 2 cm (Figure 61C) the in-plane field is less than 15 Oe, Table 4.8.

Analysing the effects of the permanent magnet in the new design mask, with the sensors positioned in line, it is clear that it causes an improvement in the impact of the magnet on sensors, Figure 4.64. For the analyses four SVs were chosen and their positioning in the chip is shown below.

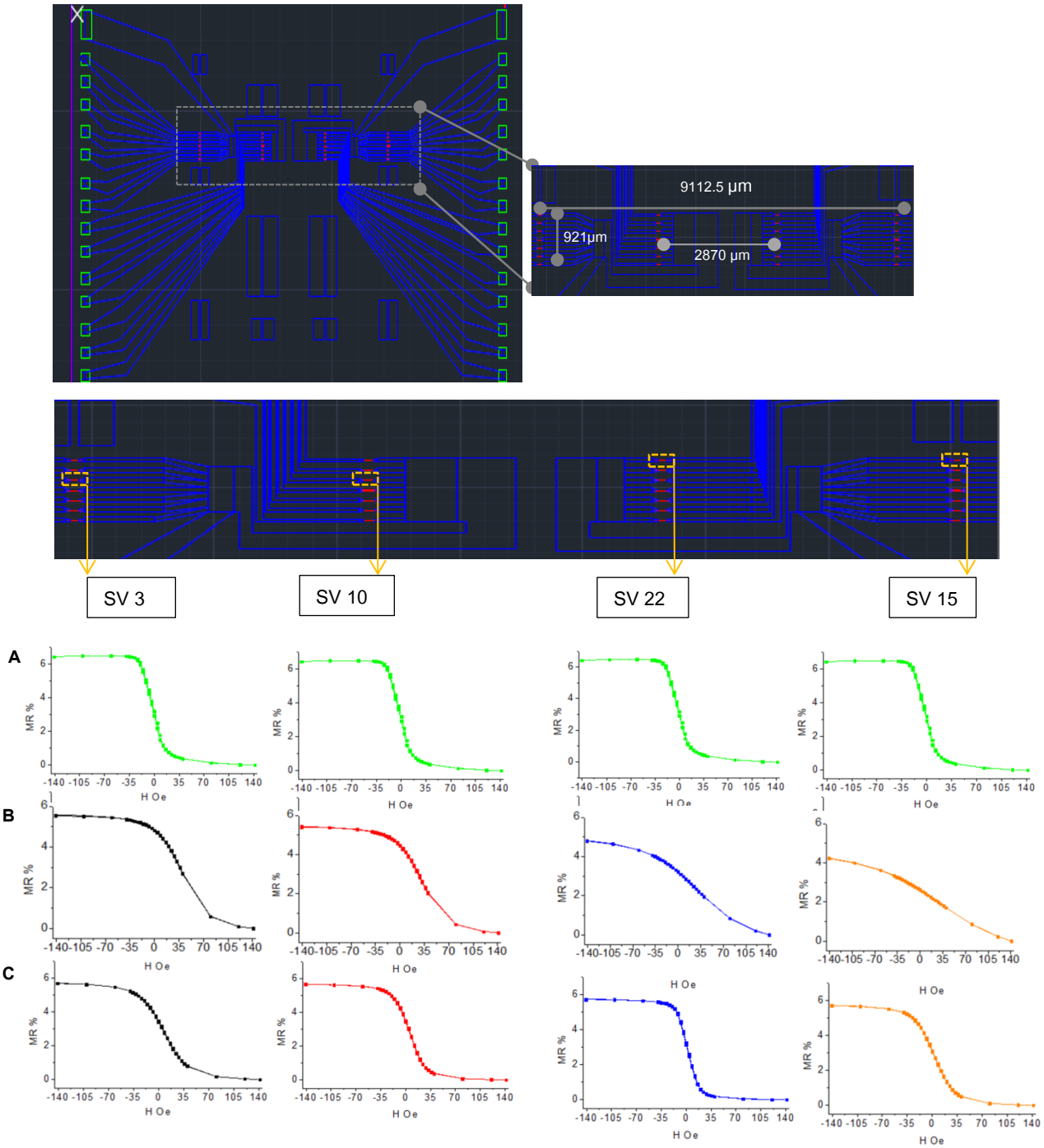

Figure 4.62 Tranfer curves of four SVs, localized in each one of microchanels, obtained when: a) there is no permanent magnet below; b) a permanent magnet is placed at 1 cm from the SVs; c) a permanent magnet is placed at 2cm below the SVs. The graphics show the influences on the tranfer curves caused by the permanent magnet presence below the sensors.

Table 4.9 Values obtained from the equation above, showing the impact of the positioning of the magnet below the sensors due to the contribution of the permanent magnet field components in saturation field sensors transfer curve.

Channel	Sv	Magnet distance [cm]	H_s [Oe]	$H^{external}$[Oe]
1	3	1	42	22
1	3	2	26	6
2	10	1	22	2
2	10	2	18	-2
3	22	1	54	34
3	22	2	16	-4
4	15	1	40	20
4	15	2	22	2

Observing the Table 4.9, for permanent magnet placed at 1 cm (Figure 4.62 B) the in-plane fields sensed by sensors are higher than 20 Oe, but when the magnet is placed at 2 cm (Figure 4.62 C) the in-plane field is less than 10 Oe. As can also be observed by the SVs transference curves of Figure 4.62 C, there are no significant changes in the transfer curves, which indicates that the SVs are well align with the area of the permanent magnet where the in-plane fields contributions are lower and do not affect the magnetization of the FL and PL.

In summary:

- Chip with the previous layout, Figure 4.60, integrated with the permanent magnet at 2cm distance allows for only 16 sensors in which the permanent magnet does not affect the sensors magnetizations.
- Chip fabricated with the improved layout, Figure 4.62, integrated with the permanent magnet at 2 cm distance does not affect the sensors transfer curves of all the 28 operational sensors, showing a considerable improvement towards the previous layout.

Chapter 5

Integration of the Biochip Platform with a portable electronic system

5.1 Electronic read-out of the sensors

Measurements of the biochip were acquired using a multi-channel PCB setup developed at INESC-ID, by Tiago Costa [19]. This system is composed by 15 channels for the parallel measurement of signals from 15 SV sensors. The sample frequency used was 50 KHz with an amplifier gain of 5000 and a bandwidth of 10 KHz, as reported by Tiago [19].

The platform is able to perform real-time signal processing for detecting variations in the resistance of MR sensors, when an external magnetic field is applied. The output is acquired on a computer through a commercial digital to analogue conversion board (Data Translation, 16 bit DAC). Then, the digital signals were post-processed using a program developed in MATLAB® by INESC-ID, that allows the user to observe voltage signals versus time.

Figure 5.63 represents the setup used in the experiments.

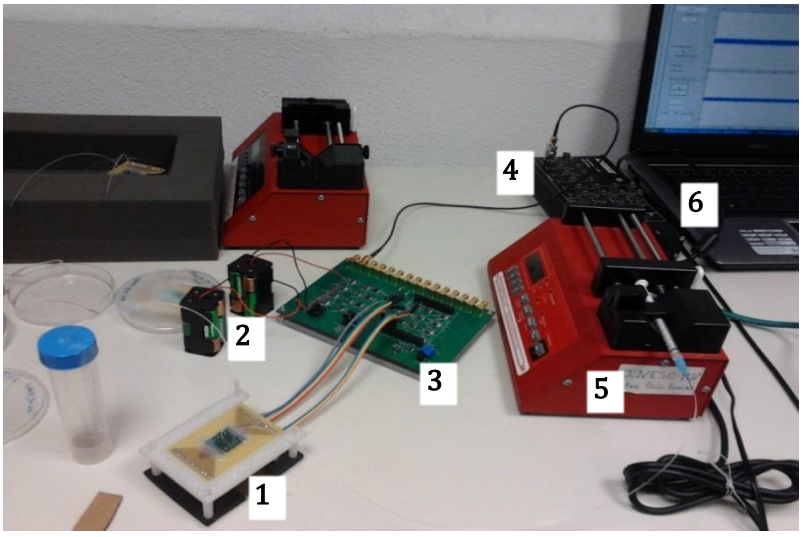

Figure 5.63 Setup used in the experiments: 1) Biochip platform; 2) batteries for power supply and portability; 3) acquisition board, which encrypts the data collected from sensors; 4) Digital to analogue converter (DAC), it is responsible for the data conversion and transition to the device for user interface (computer); 5) Syringe pump to impose flowrates; 6) User interface (computer).

The sensors were biased with 1 mA DC current. A more detailed description of this platform can be found at Tiago Costa thesis [19].

The PCB was connected to the acquisition setup by axon cables, as shown in Figure 5.63. However, all attempts failed to obtain a correct measurement because the base noise level of the SV (measured without no sample inside the michochannel) achieved high values, around 50 µV. This may be explained by a poor connectivity between the SV chip and the electronic board by the axon cables.

Consequently it was developed a third platform that could avoid the use of axon cables to circumvent the challenges faced by this platform.

5.2 Design and Development of the Third Platform

Having the goal of designing a new platform free of the use of axon cables, two PCBs were implemented in the overall setup, Figure 5.64, which allows the direct connection of the PCB to the main board, as shown in Figure 5.65.

The contacts follow inside this PCB top to bottom of the surface, where connectors were welded allowing the SV chip to interface and conduct the signals of every pad, Figure 5.64.

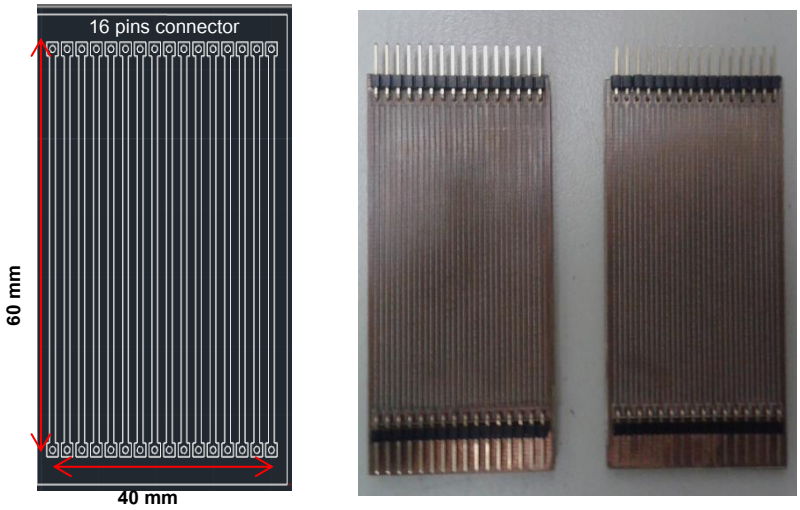

Figure 5.64 AutoCad® PCB design.

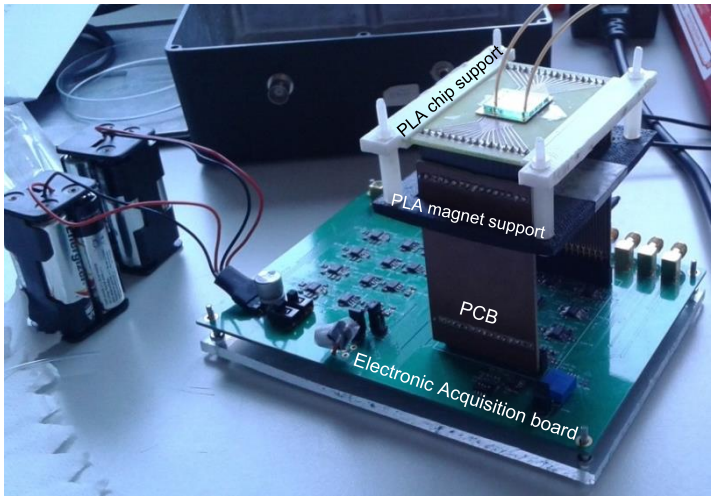

Figure 5.65 Assembly of the platform with the SV chip and permanent magnet to PCBs and data acquisition electronic platform.

5.3. Experimental Results

All experiment was performed using the experimental setup described in section 5.1 (Figure 5.63) and is showed below the new assembled between the biochip platform and the acquisition setup, Figure 5.66.

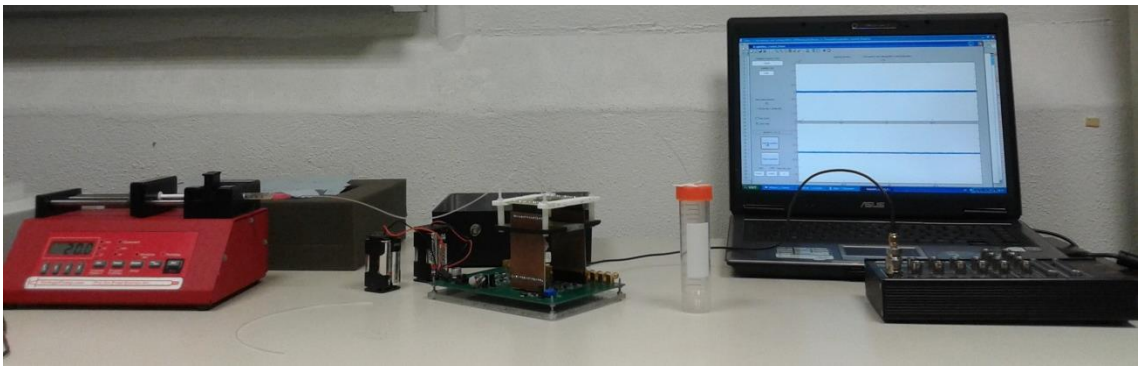

Figure 5.66 Acquisition setup assembly.

The experiment started by acquiring a baseline signal for the sensor. Then, a sample of phosphate buffer solution (PBS) without MNPs was read. This sample acts as a control as it does not have any magnetic material in its composition. Therefore it was possible to evaluate if the signal acquired with the other samples was effectively due to the presence of MNPs.

After that, a volume of magnetic particles was introduced inside the microchannels, in order to analyse different sets of samples, namely:

I. A sample consisting of 100 µL of 2800 µm MNPs in PBS with a concentration 7,00x10^6 particles/µL.

II. A sample consisting of 6 µL of 250 nm MNPs in PBS with a concentration of $4{,}9x10^{11}$ particles *per* mL.
III. A sample consisting of 6 µL of 130 nm MNPs in 40 µL PBS with a concentration of $3.5x10^{12}$ particles *per* mL.
IV. A sample consisting of 6 µL of 80 nm MNPs in 40 µL PBS with a concentration of 1.2×10^{13}particles *per* mL.
V. A sample consisting of 6 µL of 50 nm MNPs in 40 µL PBS with a concentration of $5.5x10^{13}$ particles *per* mL.

Finally, the chip was washed with deionized water until the signal returned to the baseline and also a microscope check was performed to confirm that the channel is clean and can be used in more experiments. This cleaning procedure is crucial otherwise false positives may mask the results.

In every experiment the permanent magnet was placed in the same position.

To validate the efficiency of this chip-magnet platform in the nanoparticles magnetization, some experiments with magnetic beads were performed:

i. To further validate the ability of the SVs to detect different dimension of MNPs;
ii. To attain the ability of the different sensors to detect passing magnetic particles;
iii. To detect of magnetically labelled cells.

An aspect to bear in mind deals with delivering the same flow to all microchannels in order to get reliable sensor measurement.

5.3.1 Counting

To count the magnetic events detected by MR sensors, an home-made software was developed using MATLAB, to post evaluate the signals and distinguish between noise and cell detection/counting.

The first thing to determine are the positive and negative thresholds, meaning that all data between these intervals is considered noise.

These values were obtained by checking the values of signal acquisition for the control sample that does not have any magnetic material in its composition. It means that values outside this interval are assumed to be caused by changes in the magnetic field due to MNPs flowing above the SV. Magnetic particles with signal near the noise background will be lost. The noise band is assumed to be in the interval $[-x\sigma, x\sigma]$ where the σ is the standard deviation calculated for each one of the experiments and x is the value obtained from the histogram of the signal acquisition of control sample.

An example is presented in Figure 5.67 and Table 5.10. In this case, considering the values of the background noise, should be considered an interval between $[-4\sigma, 4\sigma]$, meaning that all values outside this interval are assumed to be caused by changes in the magnetic field. It is important to notice that the more wider is the interval range, there is an higher probability to lost magnetic events detection which signal is near the noise background.

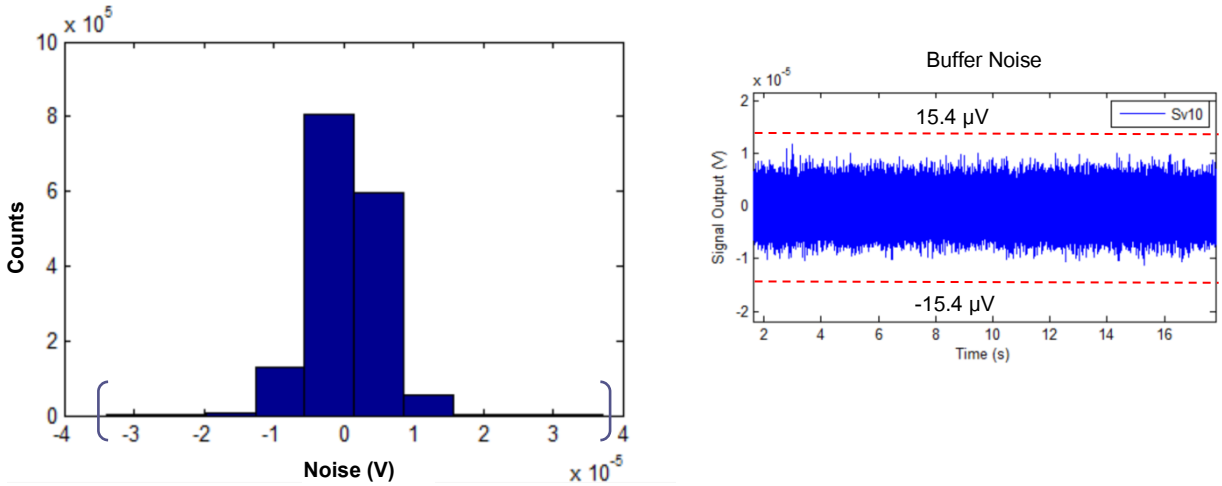

Figure 5.67 Statistical analysis of the noise measured from a sample containing non-magnetic material. The standard deviation is ~ 3.86 µV and for counting calculations (in this case) was considered to be between ± 4σ. So, in this case, the threshold should be 4 x (±3.86 x10^{-06}) = ± 1.54x10^{-05} V.

Table 5.10 Statistical analysis of the noise measured from a sample containing non-magnetic material.

Mean	STD	Maximum	Minimum
8.92x10^{-06} V	3.86x10^{-06} V	3.70x10^{-05} V	-3.39x10^{-05} V

The counting element works by finding the maxima and minima outside the noise interval and also, for the data points outside this window, Figure 5.68.

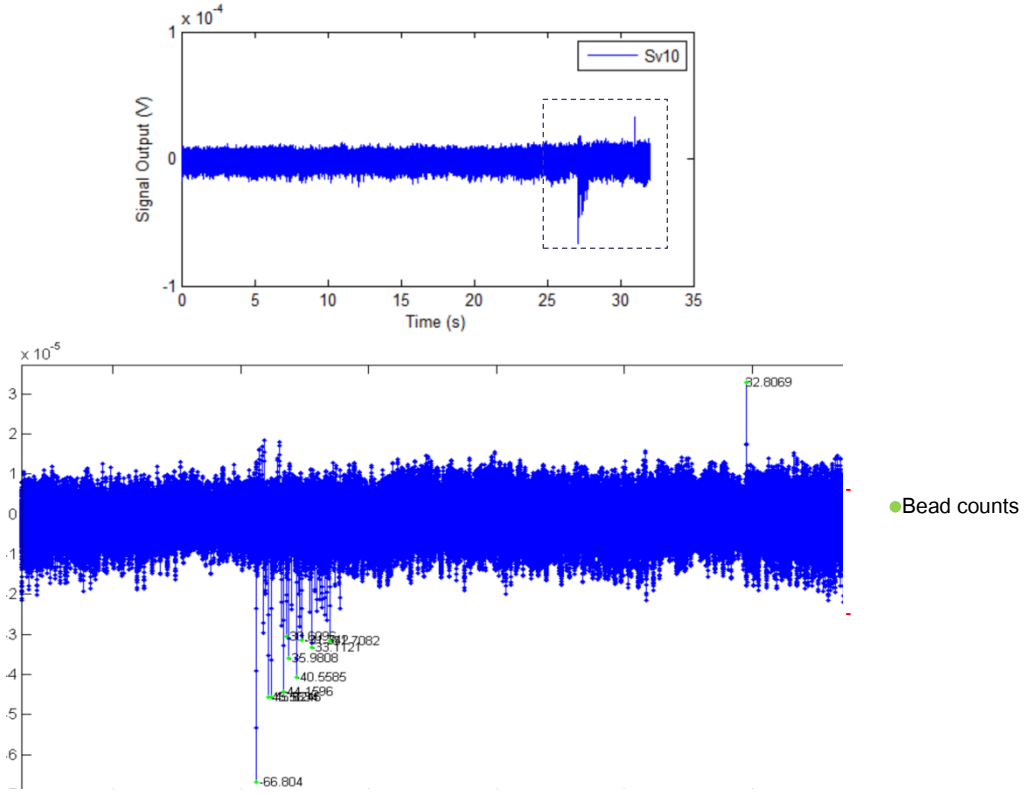

Figure 5.68 Example of data acquired (10^4 points) by one sensor when a buffer with magnetic particles flow inside the microchannel. The counting peaks software counts just the peaks above the threshold defined by the noise to the noise background.

5.3.1.1 Magnetic Particles Results

5.3.2 Validation of micro-sized and nanometer-sized magnetic particles detection

In the following batch of experiments, different sizes of nanoparticles (2800 nm - 50 nm) were tested in order to evaluate the detection sensitivity of this platform.

I. **Sample of 2800 µm MNPs in PBS**

For this validation 100µL of streptavidin coated magnetic nanoparticles (Dynabeads M-280) were diluted in 1 mL of phosphate buffered saline (PBS) solution and real time measurements were carried out at a constant flowrate of 50 µL/min. A total of 30 trials were performed.

These micro-sized particles were used in the preliminary detection experiments because they are easily observed under the microscope and their increased volume results in a higher magnetic moment *per* label under an applied magnetic field, allowing distinct detection signals at the single-label level.

Assays were performed to observe the basal noise of the sensor (SV 7) without having any sample inside the microchannel, Figure 5.69a), and control sample (PBS solution), Figure 5.69b).

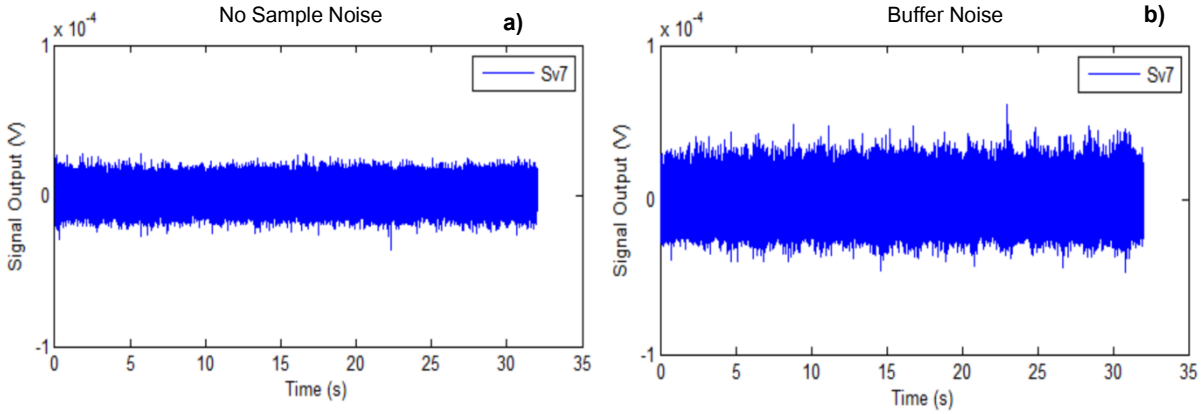

Figure 5.69 Data acquired by the SV 7: a) No sample inside the microchannel; b) When a buffer pass through the microchannel, corresponding to the noise background.

Figure 5.69b) shows that for control sample (PBS), no peak is observed and only the background noise of the sensor is expressed. According to the histogram obtained, an interval of [-5σ, 5σ] was considered, meaning that all values outside this interval are assumed to be caused by changes in the magnetic field.

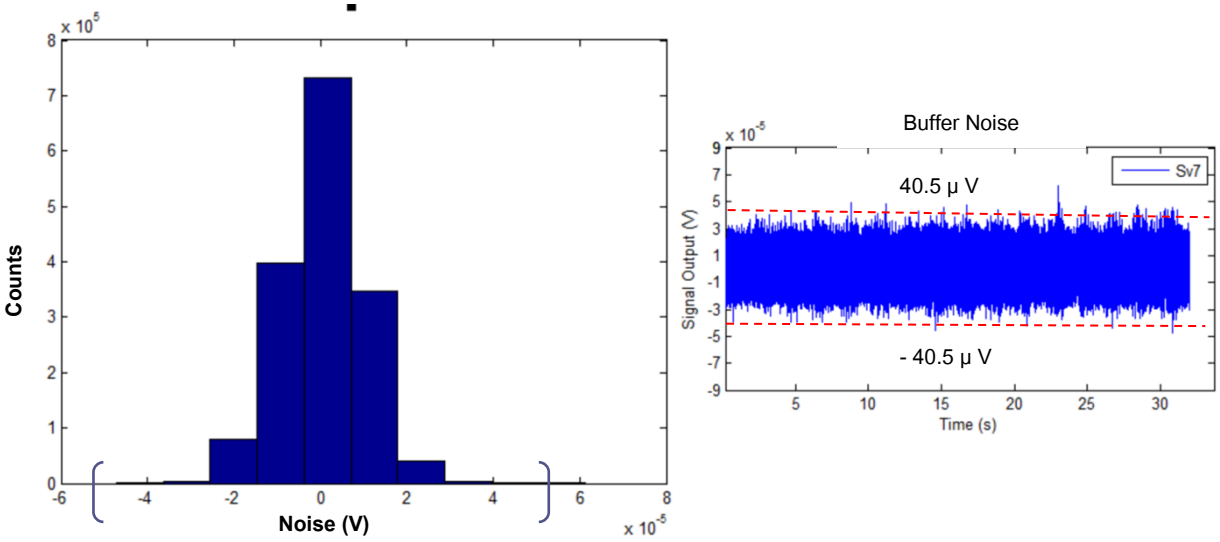

Figure 5.70 Statistical analysis of the noise measured from a sample containing non-magnetic material. The standard deviation is ~ 8 µV and for counting calculations (in this case – SV 7) was considered to be between ± 5σ. The threshold should be 5 x (±8.02 x10^{-06}) = ± 4.05x10^{-05} V.

Table 5.11 Statistical parameters of the SV 7 signal without sample flowing inside microchannel and from a sample containing no beads, only buffer.

Sample ID	Mean	STD
Noise	1.04x10^{-05} V	4.58x10^{-06} V
PBS	1.56x10^{-05} V	8.02x10^{-06} V

With the assistance of a developed counting program, it is possible to check the number of peaks above the noise level and also the amplitude of the peaks detected in µV. For this trial, the signal voltage varied between $|40\mu V - 260\mu V|$.

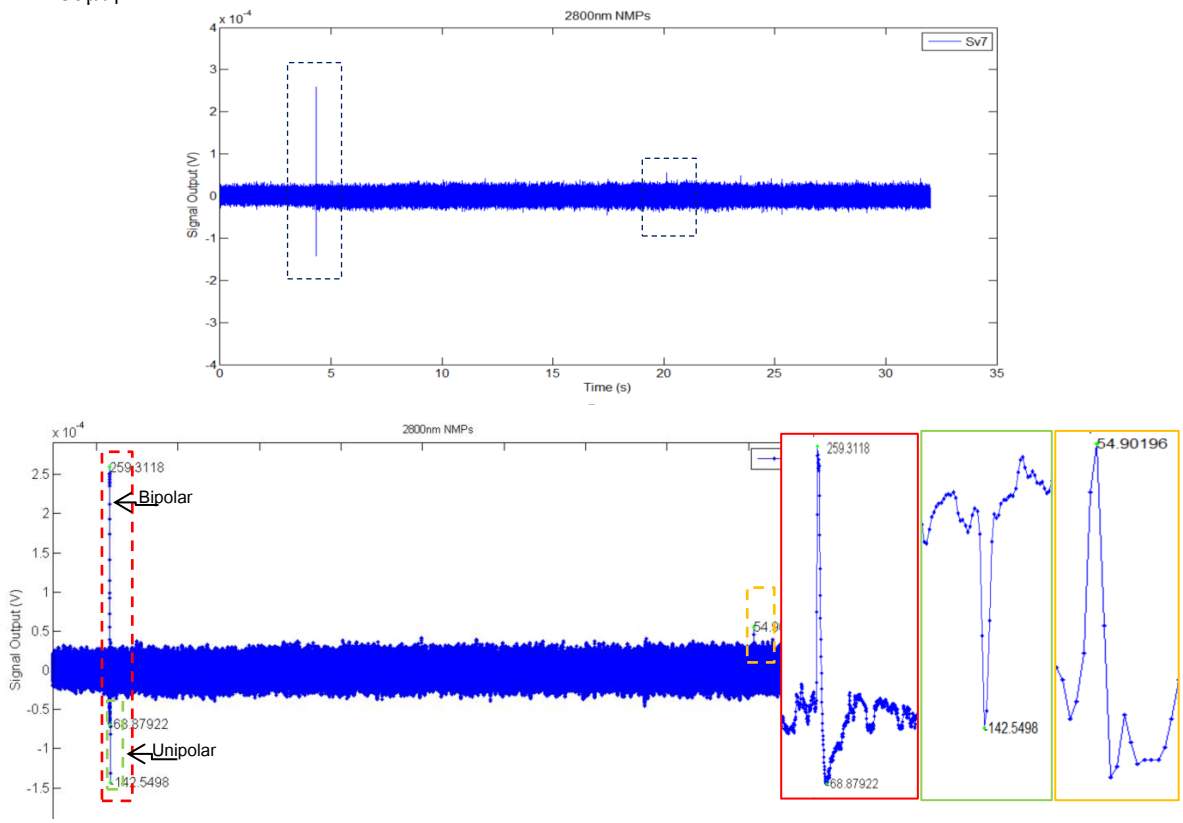

Figure 5.71 Representative figure of three single peak detection response of one sensor to one trial of 30 second run of the sample M-280 Streptavidin magnetic particles. The peak amplitude values are displayed in µV.

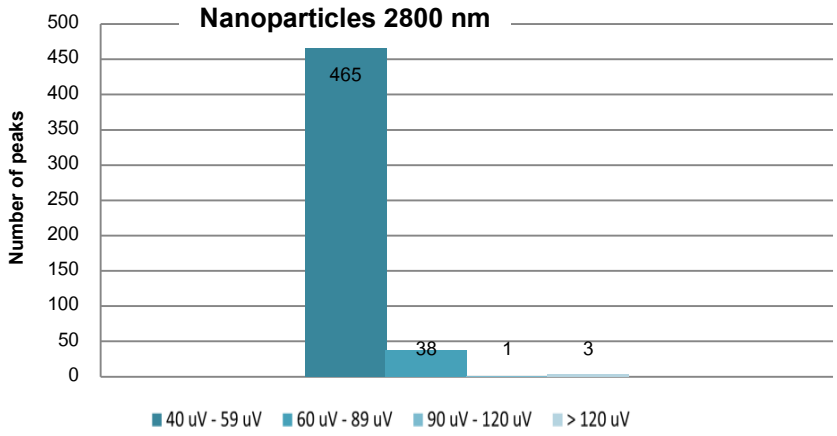

Figure 5.72 Number of peaks counted and their amplitude.

A total of 507 magnetic events were reported by the counting program, Figure 5.72.

As visible in Figure 5.71, different pulse shapes were observed – unipolar and bipolar– which are related with the magnetization direction of the particles. It is possible to observe several peaks with different intensities corresponding to particles flowing at different heights over the sensor or also if particles flow closer the sensor rotated instead of centred. This is translated in a decrease of the amplitude of peaks.

II. Sample of 250 nm MNPs in PBS

The disadvantages of micro-sized labels are the high mass and the large diameter of the label in relation to the biomolecules. Smaller nano-sized labels with high magnetic (iron-oxide) content (70-85%) offer a solution for these problems [15].

In this experiment, Nanomag®-D 250 nm particles assays were performed. The sensor selected was the Sv3

In the figure 5.73, the noise signals are screened over time.

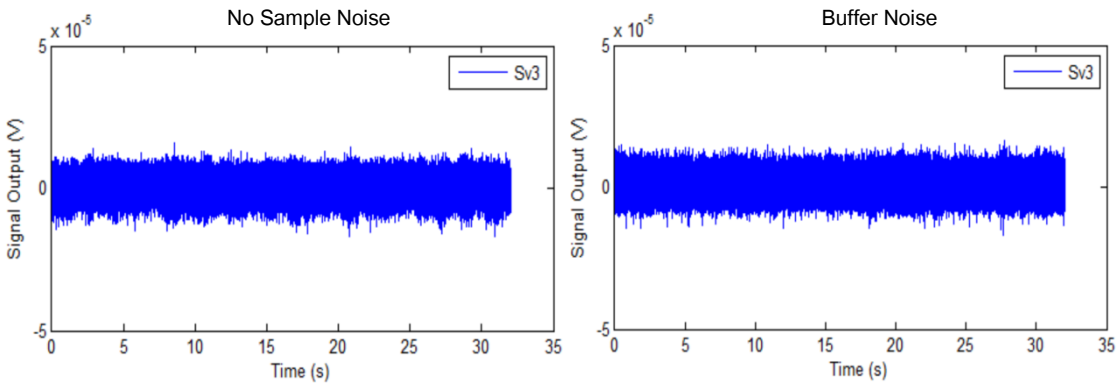

Figure 5.73 Data acquired by the SV 3: a) No sample inside the microchannel; b) When a buffer passes through the microchannel, corresponding to the noise background.

Similar to the results showed in Figure 5.69, it can be observed that PBS control sample did not result in significant variation of signal. According to the obtained histogram, an interval of [-5σ, 5σ] was considered, meaning that all values outside this interval are assumed to be caused by changes in the magnetic field.

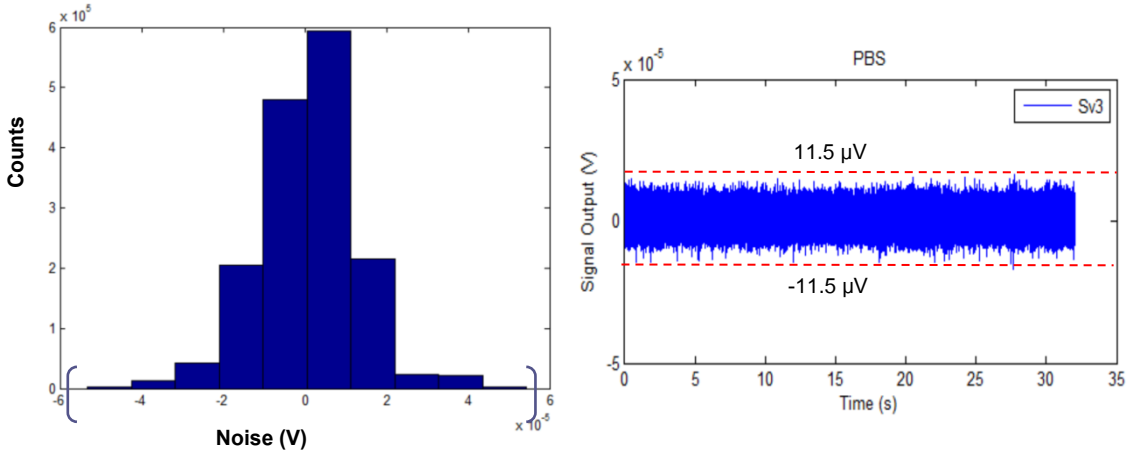

Figure 5.74 Statistical analysis of the noise measured from a sample containing non-magnetic material. The standard deviation is ~ 2 µV and for counting calculations (in this case – SV 3) was considered to be between ± 5σ. The threshold should be 5 x (±2.26 x10^{-06}) = ± 1.13x10^{-05} V.

Table 5.12 Statistical parameters of the SV 3 signal without sample flowing inside microchannel and from a sample containing no beads, only buffer.

Sample ID	Mean	STD
Noise	5.48x10^{-06} V	2.3x10^{-06} V
PBS	6.26x10^{-06} V	2.26x10^{-06} V

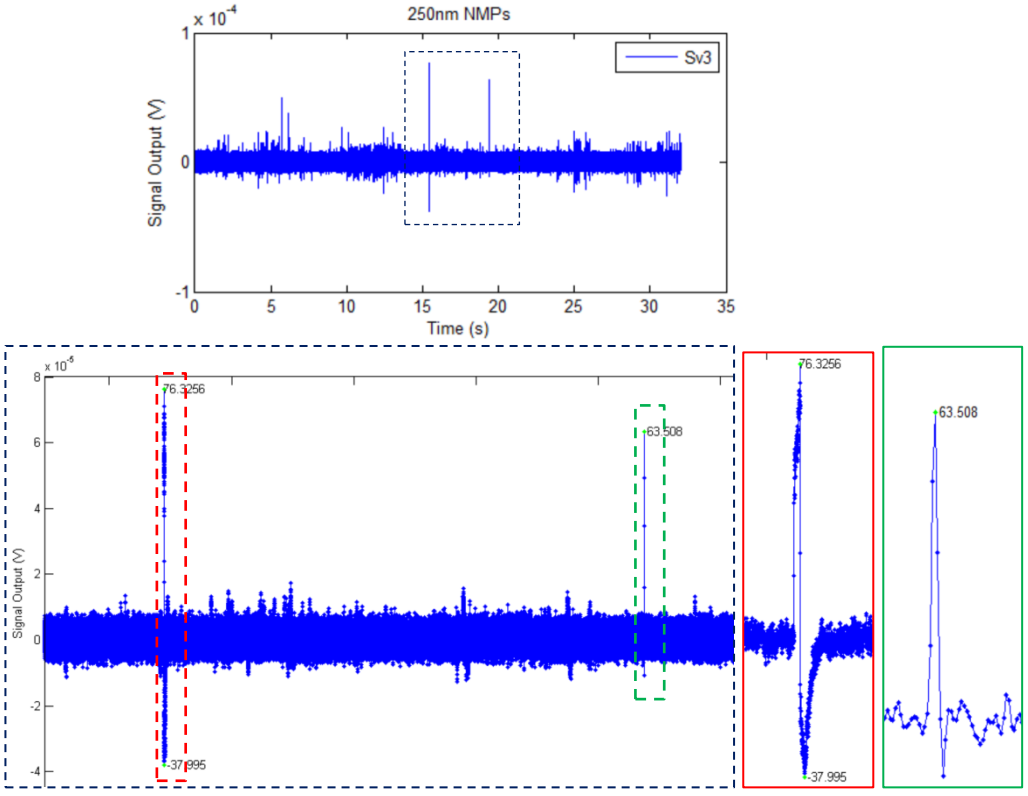

Figure 5.75 Representative figure of two single peak detection response of SV 3 to one trial of 30 second run of the sample 250nm magnetic particles. The peak amplitude values are displayed in µV.

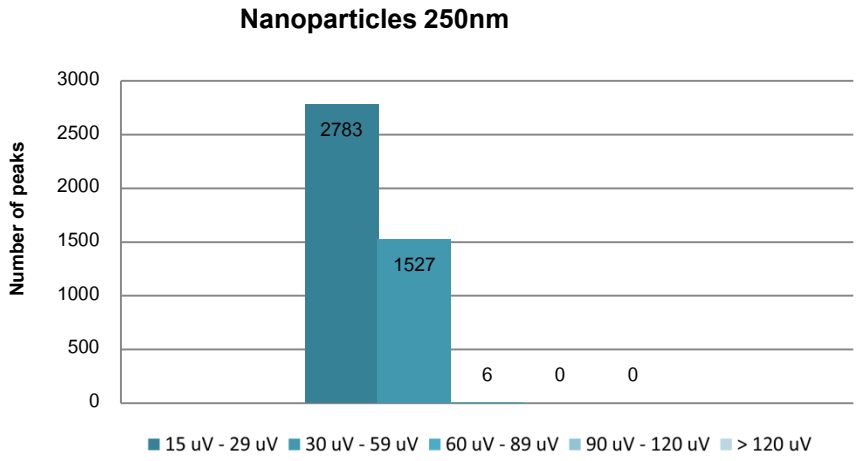

Figure 5.76 Number of peaks counted and their amplitude.

A total of 4316 magnetic events were reported by the counting software, Figure 5.76.

It is important to notice that the 250 nm superparamagnetic particles have a low individual moment and so they cannot be individually detected, meaning that the obtained peaks corresponds to an agglomeration of particles passing over the sensor at the same time.

III. Sample of 130 nm MNPs in PBS

In the next experiment, Nanomag®-D 130 nm particles were tested. In the Figure 5.77, the noise background signals are screened over time.

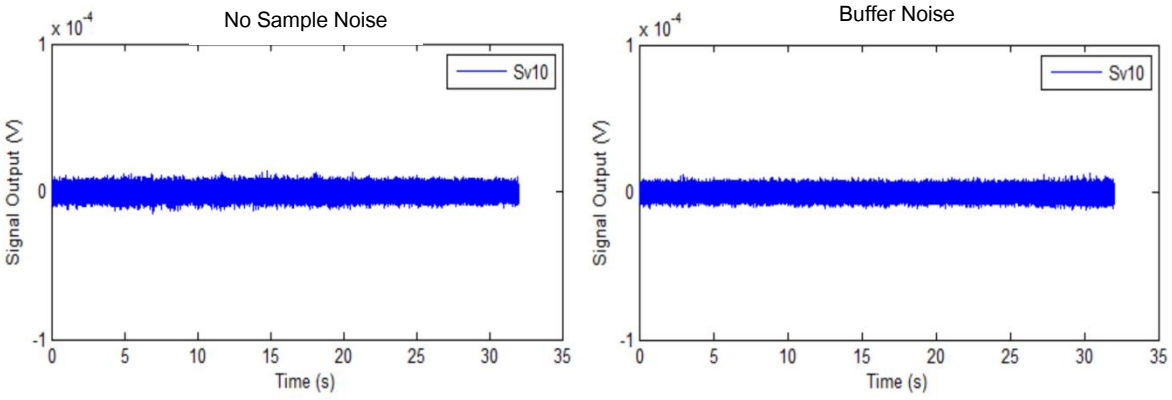

Figure 5.77 Data acquired by the SV 10: a) No sample inside the microchannel; b) When a buffer flow through the microchannel, corresponding to the noise background.

According to the obtained histogram, Figure 5.78, an interval of [-5σ, 5σ] was considered, meaning that all values outside this interval are assumed to be caused by changes in the magnetic field.

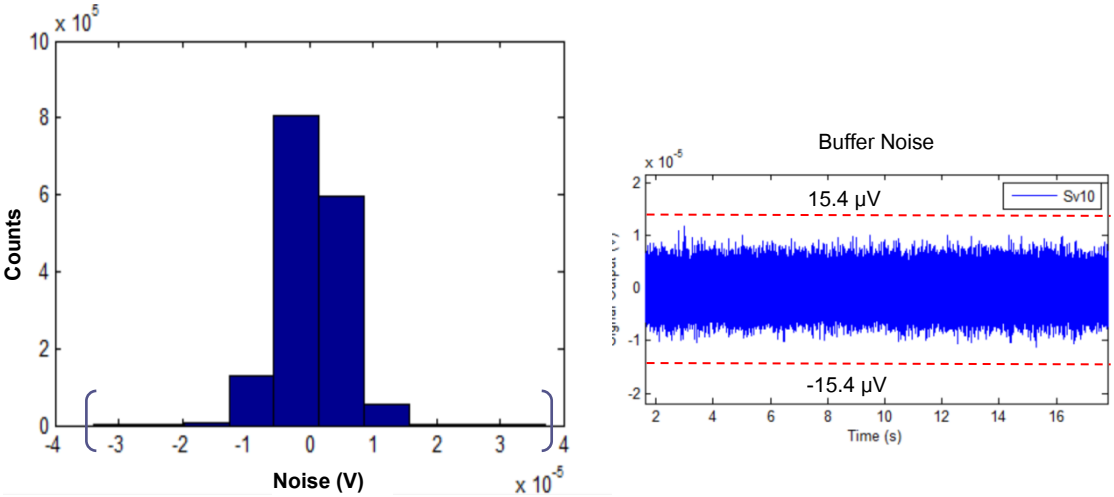

Figure 5.78 Statistical analysis of the noise measured from a sample containing non-magnetic material. The standard deviation is ~ 2 µV and for counting calculations (in this case – SV 10) was considered to be between ± 4σ. The threshold should be 4 x (±3.86 x10^{-06}) = ± 1.54x10^{-05} V.

Table 5.13 Statistical parameters of the SV 10 signal without sample flowing inside microchannel and from a sample containing no beads, only buffer.

Sample ID	Mean	STD
Noise	2.5410^{-06} V	1.74x10^{-06} V
PBS	8.92x10^{-06} V	3.86x10^{-06} V

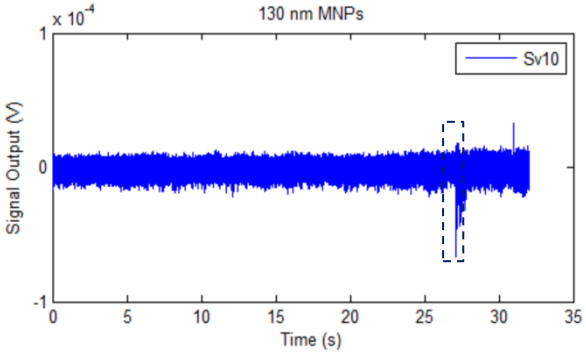

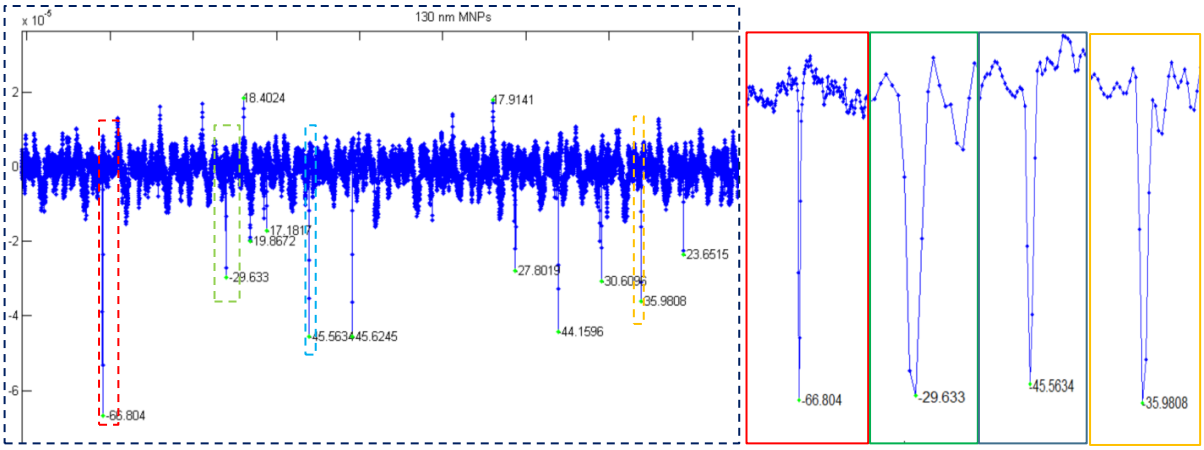

Figure 5.79 Representative figure of peak detection response of one sensor to one trial of 30 second run of the sample 130 nm magnetic particles. A zoom is applied to four single peaks. The peak amplitude values are displayed in µV.

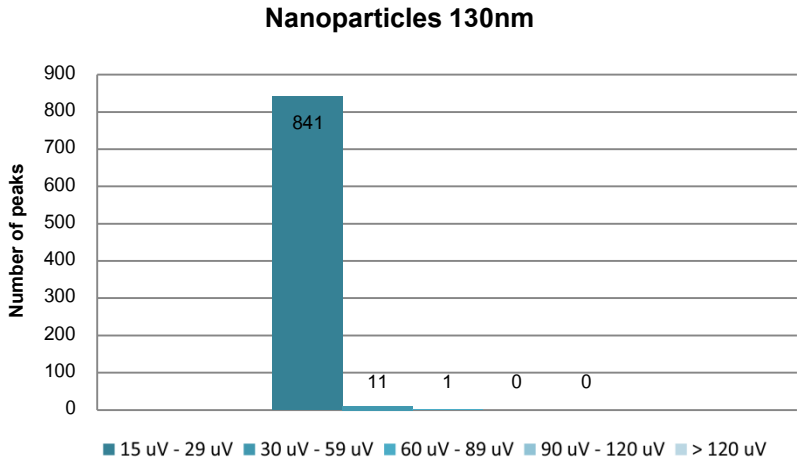

Figure 5.80 Number of counted peaks and their amplitude.

A total of 853 magnetic events were reported by the counting software, Figure 5.80.

IV. Sample of 80 nm MNPs in PBS

In the next experiment, Nanomag®-D 80 nm particles were tested. In the figure 5.81, the noise background signals are screened over time.

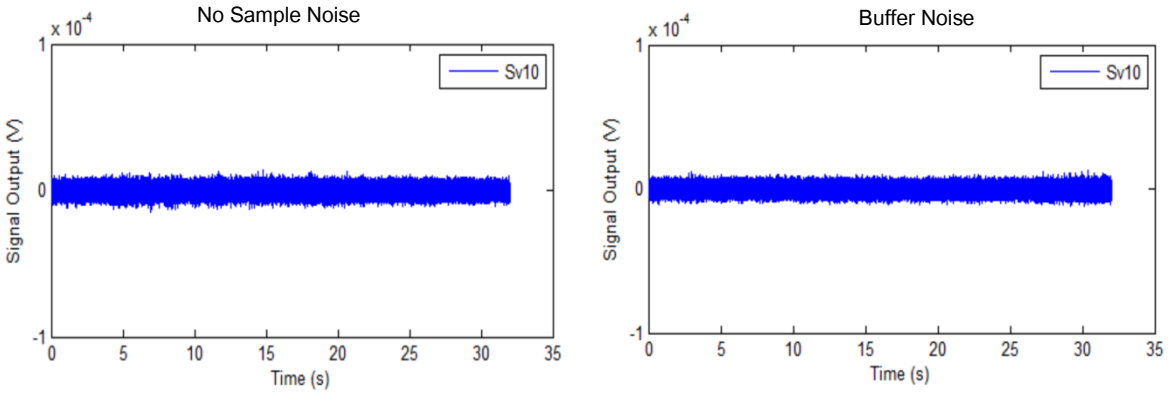

Figure 5.81 Data acquired by the SV 12: a) No sample inside the microchannel; b) When a buffer flow through the microchannel, corresponding to the noise background.

According to the obtained histogram, Figure 5.82, an interval of [-4σ, 4σ] was considered, meaning that all values outside this interval are assumed to be caused by changes in the magnetic field.

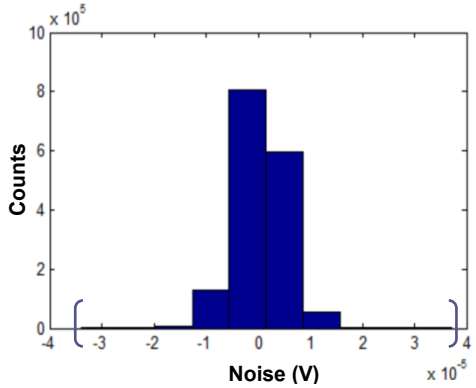

Figure 5.82 Statistical analysis of the noise measured from a sample containing non-magnetic material. The standard deviation is ~ 0.5 μV and for counting calculations (in this case – SV 12) was considered to be between ± 4σ. The threshold should be 4 x (±3.86 x10^{-06}) = ± 1.54x10^{-05} V.

Table 5.14 Statistical parameters of the SV 12 signal without sample flowing inside microchannel and from a sample containing no beads, only buffer

Sample ID	Mean	STD
Noise	2.5410^{-06} V	1.74x10^{-06} V
PBS	8.92x10^{-06} V	3.86x10^{-06} V

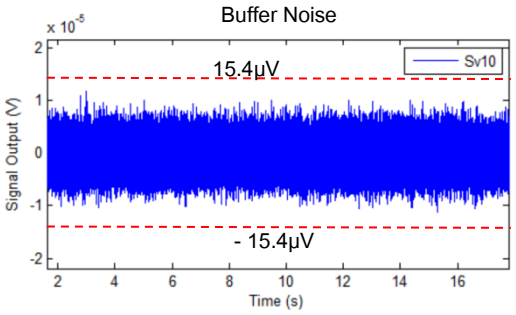

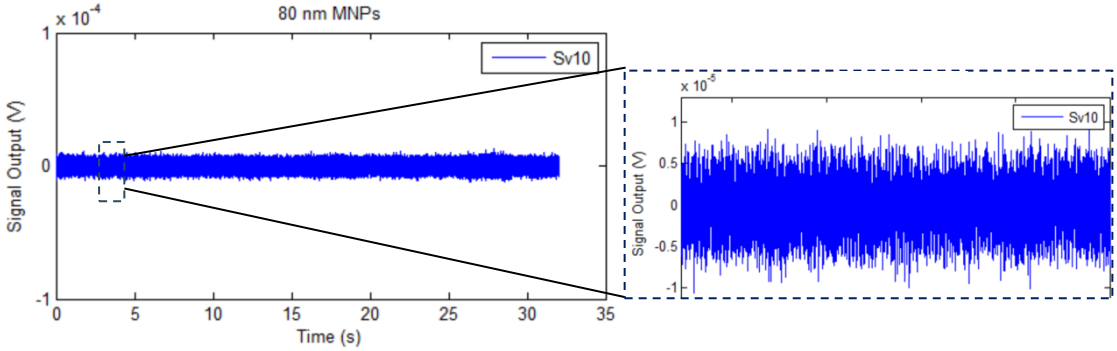

Figure 5.83 Representative figure of non-peak detection response of one sensor to one trial of the sample 80 nm magnetic particles. A zoom of the date showed that values are above the defined threshold.

In this test, no magnetic events were detected, Figure 5.83. This can be explained due to their small magnetic moment.

V. Sample of 50 nm MNPs in PBS

In this assay, Nanomag®-D 50 nm particles were measured by SV10. In the Figure 5.84, the noise signals are screened over time.

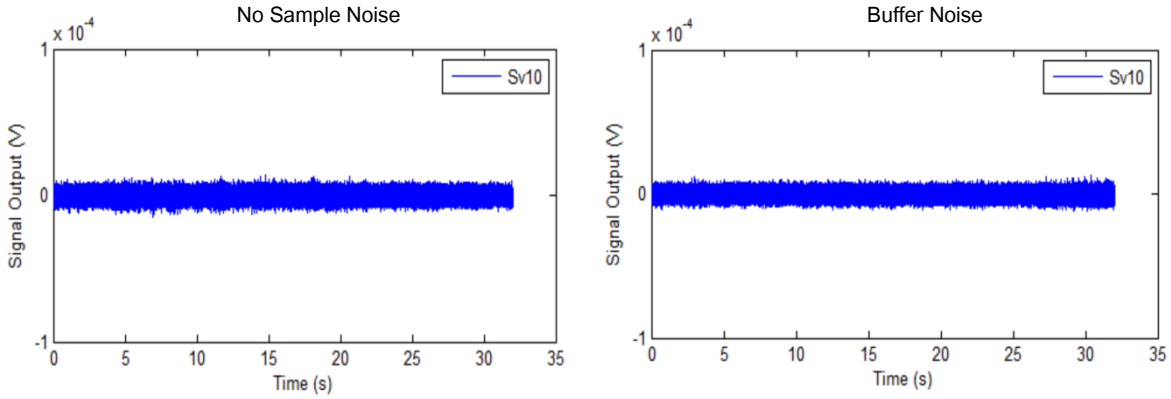

Figure 5.84 Data acquired by the SV 8: a) No sample inside the microchannel; b) When a buffer flow through the microchannel, corresponding to the noise background.

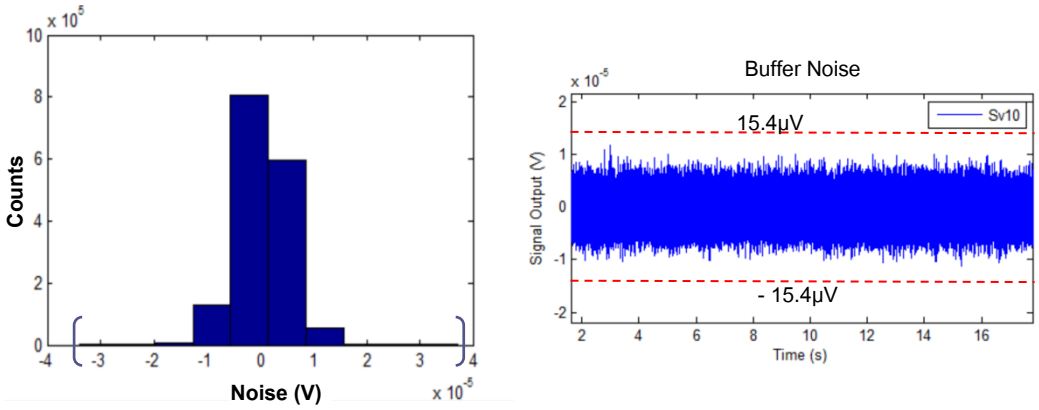

Figure 5.85 Statistical analysis of the noise measured from a sample containing non-magnetic material. The standard deviation is ~ 0.3 μV and for counting calculations (in this case – SV 8) was considered to be between ± 4σ. The threshold should be 4 x (±3.86 x10^{-06}) = ± 1.54x10^{-05} V.

Table 5.15 Statistical parameters of the SV 8 signal without sample flowing inside microchannel and from a sample containing no beads, only buffer.

Sample ID	Mean	STD
Noise	2.5410^{-06} V	1.74x10^{-06} V
PBS	8.92x10^{-06} V	3.86x10^{-06} V

Once more, and according to the obtained histogram, Figure 5.85, an interval of [-4σ, 4σ] was considered, meaning that all values outside this interval are assumed to be caused by changes in the magnetic field.

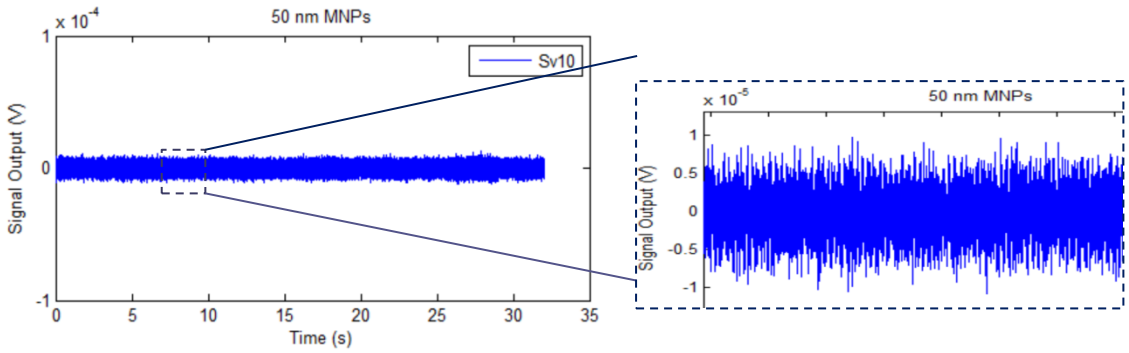

Figure 5.86 Representative figure of non-peak detection response of one sensor to one trial of 30 second run of the sample 50 nm magnetic particles.

Once more, no magnetic events were detected, Figure 5.86.

5.3.2.1 Discussion

Figures 5.69, 5.73, 5.77, 5.81 and 5.84 show that for the measurements of sensor basal noise (a) and control sample (PBS) basal noise (b), no magnetic events were observed.

On the other hand, on MNPs samples measurements, I, II and III peaks were observed (Figures 5.71, 5.75 and 5.79). This may be explained by the formation of small particles agglomerates or individual particles passing at the same time over the sensor. However, on MNPs samples measurements, IV and V, no peaks were observed,

Figure 5.83 and Figure 5.86, meaning that probably these magnetic particles do not have tendency to agglomerate or that their low magnetic moment it is not enough to be detected.

This could be explained by the fact that small particles do not tend to form clusters or their magnetic moment is too low or yet the magnetization induced by the permanent magnet is too small to induce a significant magnetic moment on the particles.

For bacteria detection, it is important not have false positives, meaning that it is not desirable to detect magnetic nanoparticles which are not linked to bacteria cells.

Thereby, according to the results shown above and the purpose of this application, it can be concluded that the probability to have false positives with 50 nm or 80 nm magnetic particles is lower than if 2800 nm, 250 nm or 130 nm particles were used.

5.3.3 Detection of Biomolecular Recognition

This dynamic detection is based on immunological recognition of *Staphylococcus aureus*, protein A negative *Staphylococcus aureus* and *Staphylococcus epidermidis spp.* cell wall peptidoglycan by a specific monoclonal antibody anti-Staphylococci spp.

The specificity of this monoclonal antibody was previously proved by Western Blotting (WB) trials [4].

Biological affinities between nanoparticle (a), surface protein A (b), IgM J chain (c) and the antibody *Staphylococci* spp. cell wall immunogenic proteins (e) are illustrated below, Figure 5.87

Particles are coated with mAb anti-staphylococci spp. IgM antibody and its J chain binds to Protein A. Protein A is expressed on *S aureus* cell wall and has a radius of ~12.5 Å.

Nanomag®-D-spio 50 nm particles were selected as labels of monoclonal antibodies anti-*Staphylococcus SPP,* because they have protein A on the surface and can bind J chain, which recognize (via biomolecular recognition) bacterial staphylococci in the sample.

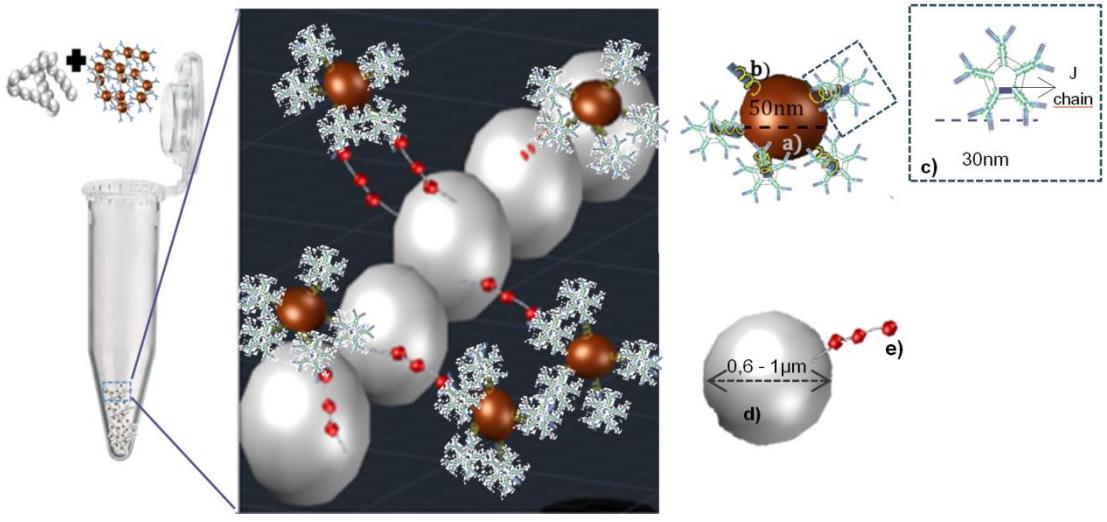

Figure 87 Schematics of immuno-magnetic functionalization of cells. a) 50 nm Superparamagnetic particle; b) Protein A; c) anti-staphylococci spp. monoclonal antibody; d) Staphylococcus Cell; e) Staphylococci immunogenic protein.

Raw milk for experiments was collected aseptically from a healthy cow. The cell culture and magnetic functionalization and labelling were performed by a colleague at Veterinary Faculty.

Each sample for sensor testing has 500 µL of volume:

- 2 µL of functionalized nanoparticles suspension;
- 98 µL of PBST;
- 400 µL of mastitic milk.

The acquisition tests were performed with the same flow rates used for the magnetic particle acquisition tests, 50 µL/min.

For the experiments, three samples were considered:

I. A blank sample of raw milk;
II. A control sample with raw milk and 2 µL of nanoparticles functionalized with anti-*staphylococci spp.*
III. A test sample with milk and 2 µL nanoparticles functionalized with anti-*staphylococci spp*. Antibody and 10 000 cfu of *Staphylococcus* cells.

In a previous work [4], a limit of 8 x 10^8 functionalized nanoparticles in 2 µL of buffer suspension was the concentration optimized in order to not have magnetic signal in milk control sample and magnetic signal in milk samples with known bacterial concentrations.

First step needed to be determined is the positive and negative threshold, Figure 5.89.

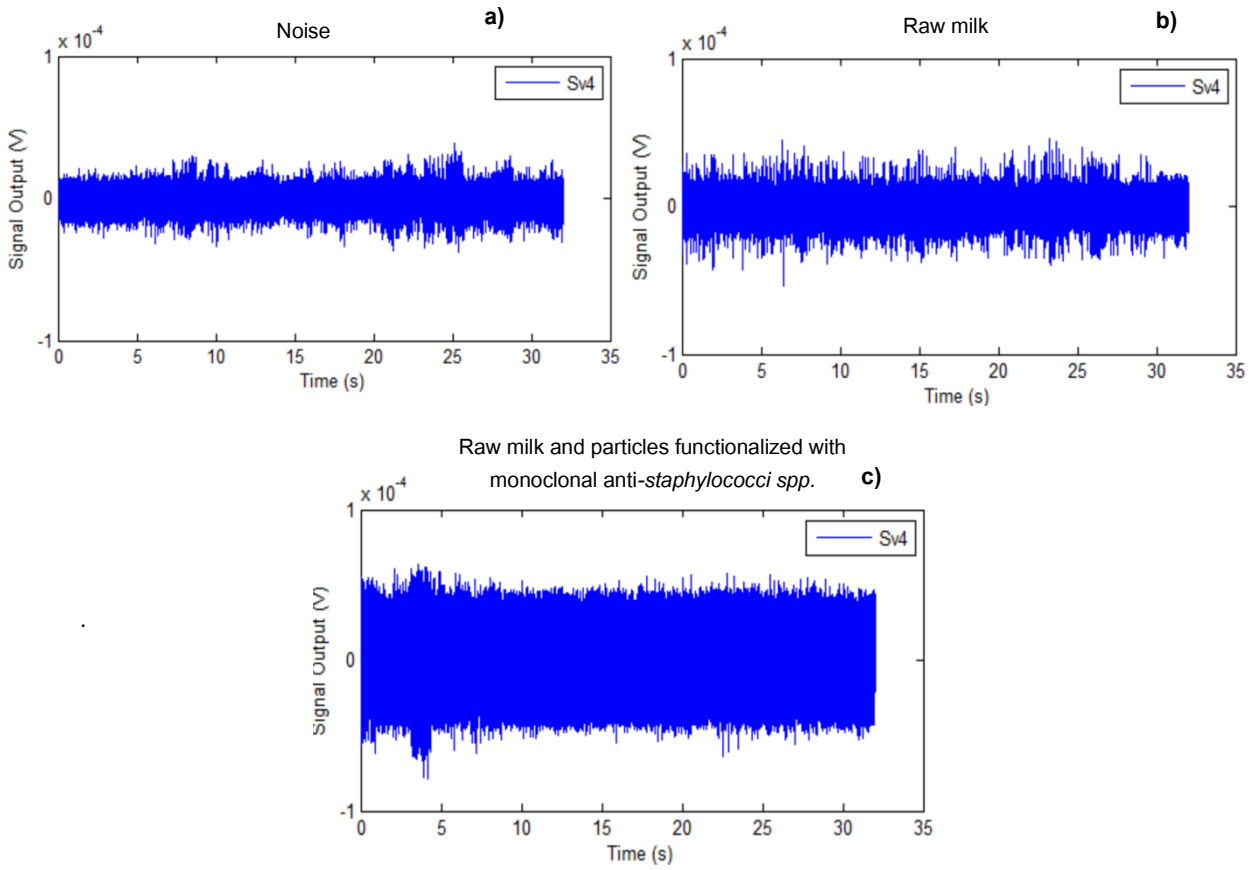

Figure 5.88 Acquired signal: a) sensor base noise level ; b) raw milk blank sample; c) raw milk with functionalized nanoparticles (control sample).

In Figure 5.88, it can be observed that the sensor output is noisier with the nanoparticles present c) than with just milk b).

In raw milk control sample, a noise level of 10 µV - 16 µV, Table 5.16, was observed. However, when nanoparticles are present, the sensor readout is affected by the fluctuations of the particles position, increasing signal fluctuations in the measured output.

According to the histogram obtained, Figure 5.89, an interval of [-6σ, 6σ] was considered, meaning that all values outside this interval are assumed to be caused by changes in the magnetic field.

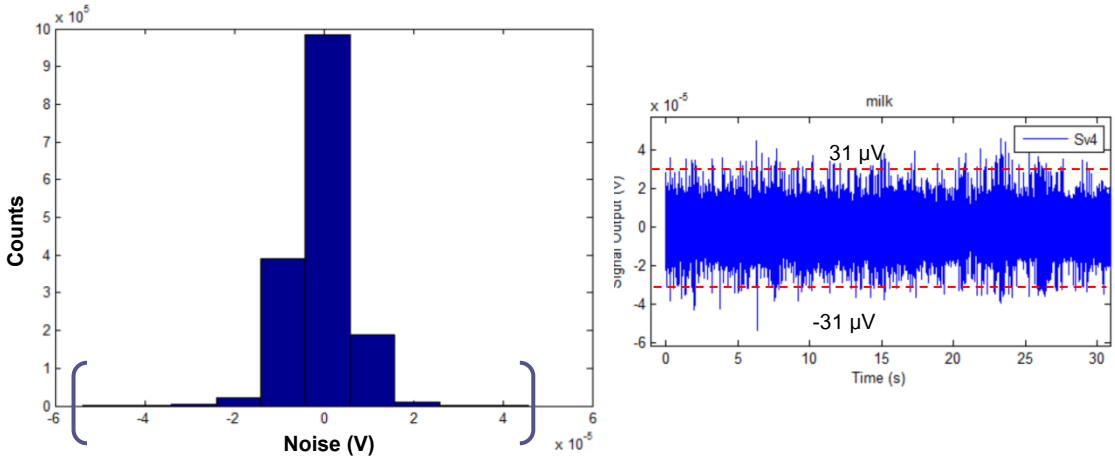

Figure 5.89 Statistical analysis of the noise measured from a sample containing non-magnetic material. The standard deviation is ~13 µV and for counting calculations (in this case – SV 4) was considered to be between ± 6σ. The threshold should be 6 x (±5.16 x10^{-06}) = ± 3.1x10^{-05} V.

Table 5.16 Statistical parameters of the SV 4 signal without sample flowing inside microchannel, from a milk sample, milk sample with functionalized MNPs and a milk sample with bacteria's labelled with functionalized MNPs.

Sample ID	Mean	STD
Noise	1.103x10^{-05} V	6.12x10^{-06} V
Milk	1.13x10^{-05} V	5.16x10^{-06} V
Milk + MNP	1.47x10^{-05} V	1.29x10^{-05} V

Figure 5.90 shows a representative detection response to one trial of 30 seconds of the sample raw milk with *Staphylococcus* cells.

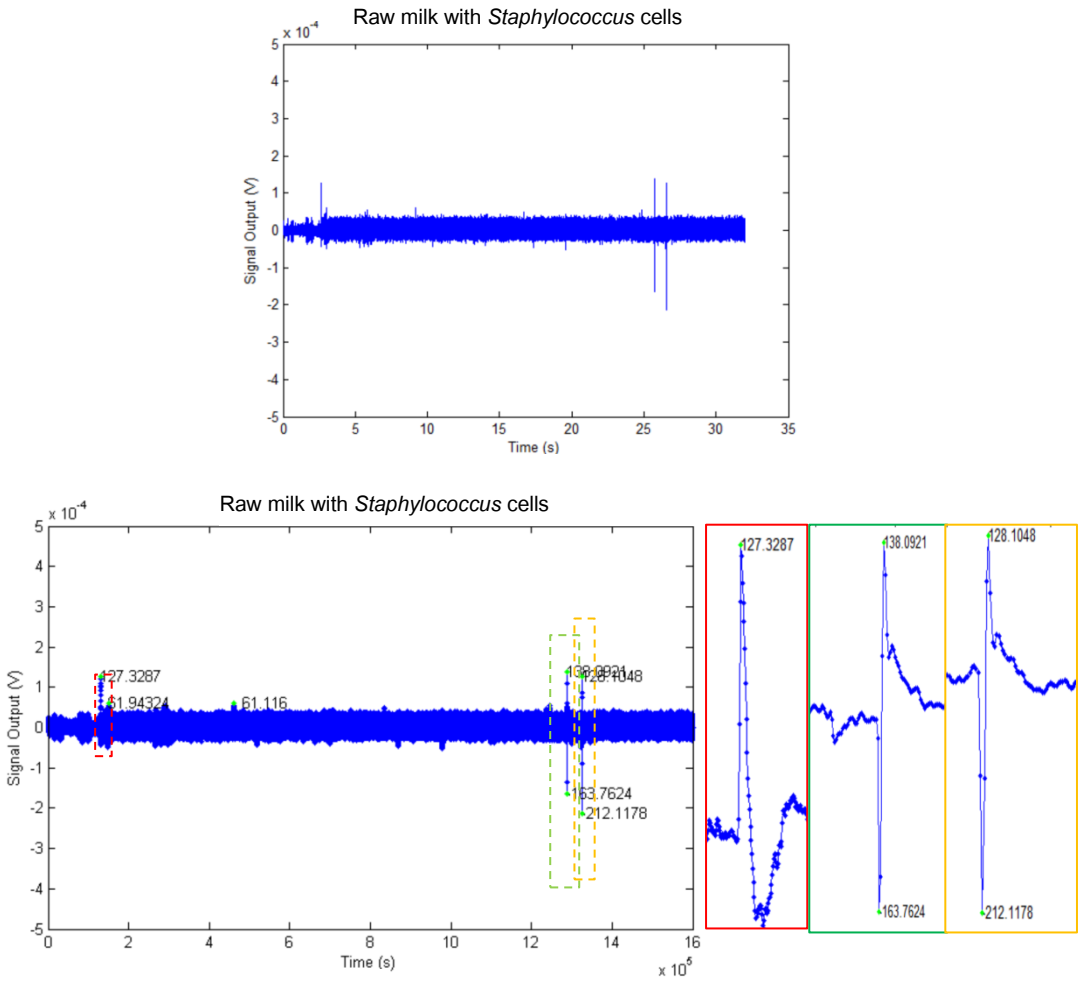

Figure 5.90 Raw milk sample with Staphylococcus cells. The peak amplitude values are displayed in µV.

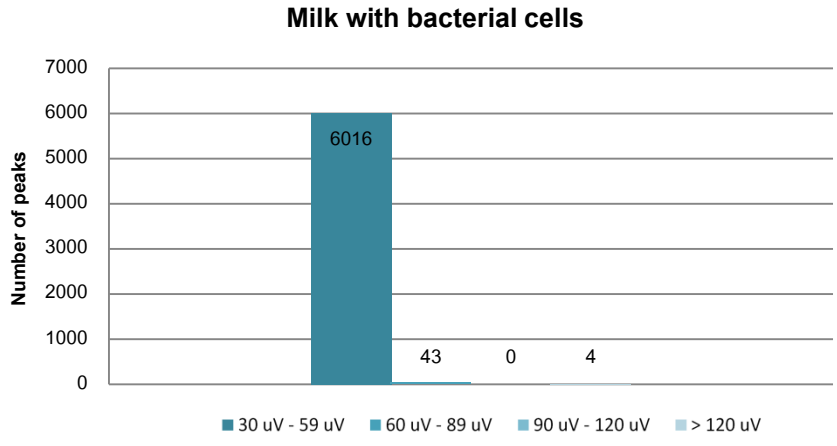

Figure 5.91 Number of peak counts of the sample measured and the amplitude.

Taking into consideration data points acquired in the 13 trials, the number of counts from noise outside the defined ±31 µV corresponds to 6063 SV counts matching cell events (Figure 5.91) and the amount of *Staphylococcus* spp. in the 500µL sample corresponds to 10 000 cfu .

5.3.3.1 Discussion

It was proved the ability of the device to detect magnetically labelled cells but it was not possible to quantify in an accurate way, as intended. Peaks with different intensities, an irregular shape and sometimes a longer time difference between the first and last point of the peak were observed.

In fact, *Staphylococcus* spp. lives in colonies, forming clusters, so assuming that each peak corresponds to magnetically labelled cells agglomeration, the large difference in peaks amplitude can be explained by cells number in each agglomerate. Furthermore, the size of the colonies can be higher than the sensors width, so when the cells pass over the sensor, the average of the fringe field may not correspond to a sphere and thus an irregular signal shape is observed, being misinterpreted as low intensity noise.

Another problem is related with the fact that it is not possible to know the number of beads that a cell can attach to its surface, which depends of the number of immunogenic proteins on the cell's surface and the amount of antibodies on the beads' surface. This means that it is possible to have a colony with just few cells and a lot of beads attached and the signal output will be higher than a colony with a lot of cells that flow over the sensor but that has just a few amount of beads attached.

On the other hand, these agglomerates can flow at different heights above the sensor which also influences peak amplitude.

In Figure 5.90, one of the represented peaks is unipolar, which can indicate that magnetic moment of the particle was not oriented in z direction. This does not contradicts the fact that a z field is applied during the experiment by the permanent magnet, because cells suffer rotation due to the flow.

Based on peak analysis, and comparing these results with those of magnetic nanoparticles, are observed peaks with higher amplitudes and with more regular shape.

At this stage, only qualitative analyses of the results can be performed. In fact, bacterial cells of *Staphyloc*occus are present and their presence can be correlated with peaks.

An improved signal analysis and better electronics control should be performed to obtain cells quantification. The system must be robust to allow portability and point of care uses in 'on farm' tests.

Chapter 6

Conclusions and Future work

This work addressed the optimization of permanent magnet integration on a biochip, which comprises MR sensors and microfluidics, as magnetic source for magnetic nanoparticles that flow inside the microchannels. The ultimate goal was to detect and count cells in milk samples, therefore prior to the assays using, in collaboration with a colleague at INESC-MN doing a PhD on veterinary.

After an introduction of the MR chip platform, the thesis describe fabrication steps of the biochip and its integration with microfluidics in a PCB, in order to obtain an integrated lab-on-chip device, whose advantages comprise sensitivity, portability, rapidity, low-cost and user-friendliness.

To optimize the integration of the chip with permanent magnet A magnet scanning platform was to measure the perpendicular and longitudinal fields of the permanent magnet surface at variable distances to the sensor.The objective was to find the area of the magnet where the perpendicular fields are high and the longitudinal fields are as low as possible so that the sensor's behaviour is not affected. The measurements performed at different distances between sensor and magnet led to the conclusion that the magnet placed at 2 cm from the sensor allows for all twenty eight sensors to be functional. Using a 3D printer, a PLA support was constructed so that the referred distance between the chip and the magnet, could be permanently maintained in the portable platform Lab-on-Chip.The electrical characterization of the sensors using this optimized platform, confirmed that at a 2 cm distance of the chip, the permanent magnet does not affect the sensors transfer curves.

MR-chip platform measurements were conducted after its integration with an electronic platform developed by INESC-ID 2 years ago. For the data analysis, a home-made software was developed in this thesis to count magnetic events. The validation of the platform optimized in this study involved measurements of magnetic particles and detection of labelled cells.

To validate the efficiency of the magnet in the nanoparticle magnetization, several tests with magnetic nanoparticles of different dimensions were performed and magnetic detection was successfully confirmed in nearly all assays. This is probably associated with the formation of clusters, as a single particle cannot be detected by the sensor, as shown by the reported simulations. In fact, for the smaller particles used in the analysis, 80 nm and 50 nm, no magnetic events were detected. This could be explained by the fact that smaller particles do not tend to form clusters or because the magnetic moment is too low or the magnetization is too small to induce significant magnetic moment on the particles. However, for biological detection it is important to minimize the occurrence of false positives, therefore the detection of magnetic particles not linked to the target is not desirable. As such, the results here reported suggest that the probability to have false positives would be lower with 80 nm or 50 nm particles.

The last step of the study was done in collaboration with Veterinary Faculty and involved assays using milk samples with a known concentration of *Staphylococcus* spp. cells that successfully confirmed the presence of the bacterial cells. In particular, 500 μL of milk sample with 10 000 cfu of *Staphylococcus* spp. was positively detected and 6063 magnetic events were identified using the Matlab® counting software.

Overall, the main goals of this work were achieved:

-Improved uniformity of magnetic field created by the permanent magnet

-Integration platform for the system chip-magnet at controlled separations

For a better accuracy of the results, it would be positive to have several sensors detecting at same time. This hardware was already started to be developed (Tiago Costa, at INESC-ID) however, currently the electronic platform does not read more than one sensor A key improvement would be to optimize the electronic so that the sensors could function in parallel during measurements.

In addition to improvements in the electronic platform, future perspectives include further optimization on PDMS microchannels design in order to create a separation module. The idea is to have a system of microchannels integrated with magnets during assays to allow the separation of magnetic particles from the other components of the sample, so that cleaner signals can be achieved.

The development of a Lab-on-Chip platform for biological quantification needs time and work from many different people combining different types of know-how. This thesis represents one step accomplished towards a portable and reliable biomedical platform.

Bibliography

[1] C. Viguier, S. Arora, N. Gilmartin, K. Welbeck, and R. O'Kennedy, "Mastitis detection: current trends and future perspectives," *Trends Biotechnol.*, vol. 27, no. 8, pp. 486–493, 2009.

[2] U. S. and S. K. Rajib Deb, "Trends in Diagnosis and Control of Bovine Mastitis: A Review," vol. 16, no. 23, pp. 1653–1661, 2013.

[3] A. J. Bradley, "Bovine Mastitis: An Evolving Disease," *Vet. J.*, vol. 164, no. 2, pp. 116–128, 2002.particles and magnetic force microscopy," *J. Biotechnol.*, vol. 120, no. 3, pp. 308–314, 2005.

[4] A. Fernandes, C. Duarte, F. Cardoso, R. Bexiga, S. Cardoso, and P. Freitas, "Lab-on-Chip Cytometry Based on Magnetoresistive Sensors for Bacteria Detection in Milk," *Sensors*, vol. 14, no. 8, pp. 15496–15524, 2014.

[5] J. B. Haun, T. J. Yoon, H. Lee, and R. Weissleder, "Magnetic nanoparticle biosensors," *Wiley Interdiscip. Rev. Nanomedicine Nanobiotechnology*, vol. 2, no. 3, pp. 291–304, 2010.

[6] A. V. Silva, D. C. Leitao, J. Valadeiro, J. Amaral, P. P. Freitas, and S. Cardoso, "Linearization strategies for high sensitivity magnetoresistive sensors," *Eur. Phys. J. Appl. Phys.*, vol. 72, no. 1, p. 10601, 2015.

[7] M. M. Ã and M. Prins, "Magnetic biochips : a new option for sensitive diagnostics," vol. 293, pp. 702–708, 2005.

[8] D A. D. Henriksen, S. X. Wang, and M. F. Hansen, "On the importance of sensor height variation for detection of magnetic labels by magnetoresistive sensors," *Nat. Publ. Gr.*, no. April, pp. 1–11, 2015.

[9] T. Hung, D. Kim, B. Rao, and C. Kim, "Novel Planar Hall Sensor for Biomedical Diagnosing Lab-on-a-Chip," *State Art Biosens. - Gen. Asp.*, pp. 197–239, 2013.

[10] J. Loureiro, P. Z. Andrade, S. Cardoso, C. L. Da Silva, J. M. Cabral, and P. P. Freitas, "Spintronic chip cytometer," *J. Appl. Phys.*, vol. 109, pp. 2255–2261, 2011.

[11] P. P. Freitas, R. Ferreira, S. Cardoso, and F. Cardoso, "Magnetoresistive sensors," J. Phys. Condens. Matter, vol. 19, no. 16, p. 165221, 2007.

[12] Y. W. Jun, J. W. Seo, and J. Cheon, "Nanoscaling laws of magnetic nanoparticles and their applicabilities in biomedical sciences," Acc. Chem. Res., vol. 41, no. 2, pp. 179–189, 2008.

[13] H.-L. Hsiao, "Magnetic Properties," *Handb. Semicond. Nanostructures Devices*, pp. W19–W56, 2005.

[14] D. R. Baselt, G. U. Lee, M. Natesan, S. W. Metzger, P. E. Sheehan, and R. J. Colton, "A biosensor based on magnetoresistance technology," *Biosens. Bioelectron.*, vol. 13, no. 7–8, pp. 731–739, 1998.

[15] D. L. Graham, H. a. Ferreira, and P. P. Freitas, "Magnetoresistive-based biosensors and biochips," *Trends Biotechnol.*, vol. 22, no. 9, pp. 455–462, 2004.

[16] J. Jezný and M. Čurilla, "Position Measurement with Hall Effect Sensors," *Am. J. Mech. Eng.*, vol. 1, no. 7, pp. 231–235, 2013.

[17] R. L. H. Sensor and P. Applications, "Ss495a."

[18] V. K. Pamula, "Heterogeneous Immunoassays Using Magnetic beads On a Digital Microfluidic Platform," *Lab Chip*, vol. 8, no. 12, pp. 2188–2196, 2008.

[19] T. Miguel and L. Marta, "INSTITUTO SUPERIOR T ECNICO Integrated Circuits for Interfacing Magnetoresistive Sensors."

[20] V. C. Martins, F. a. Cardoso, J. Germano, S. Cardoso, L. Sousa, M. Piedade, P. P. Freitas, and L. P. Fonseca, "Femtomolar limit of detection with a magnetoresistive biochip," *Biosens. Bioelectron.*, vol. 24, no. 8, pp. 2690–2695, 2009.

[21] http://rsta.royalsocietypublishing.org/content/369/1948/3198

[22] J. Loureiro, C. Fermon, M. Pannetier-Lecoeur, G. Arrias, R. Ferreira, S. Cardoso, and P. P. Freitas, "Magnetoresistive detection of magnetic beads flowing at high speed in microfluidic channels," *IEEE Trans. Magn.*, vol. 45, no. 10, pp. 4873–4876, 2009.

[23] P. P. Freitas, H. a. Ferreira, D. L. Graham, L. a. Clarke, M. D. Amaral, V. Martins, L. Fonseca, and J. S. Cabral, "Magnetoresistive DNA chips," *Magnetoelectronics*, no. 1, pp. 331–373, 2004.

[24] a Munir, J. Wang, and H. S. Zhou, "Dynamics of capturing process of multiple magnetic nanoparticles in a flow through microfluidic bioseparation system.," *IET Nanobiotechnol.*, vol. 3, no. 3, pp. 55–64, 2009.

[25] N.-T. Nguyen, S. A. M. Shaegh, N. Kashaninejad, and D.-T. Phan, "Design, fabrication and characterization of drug delivery systems based on lab-on-a-chip technology.," *Adv. Drug Deliv. Rev.*, vol. 65, no. 11–12, pp. 1403–19, 2013.

[26] N. Pamme, "Continuous flow separations in microfluidic devices," *Lab Chip*, vol. 7, no. 12, p. 1644, 2007.

[27] N. Pamme, "Magnetism and microfluidics," *Lab Chip*, vol. 6, no. 1, pp. 24–38, 2006.

[28] N. Pamme and A. Manz, "On-chip free-flow magnetophoresis: Continuous flow separation of magnetic particles and agglomerates," *Anal. Chem.*, vol. 76, no. 24, pp. 7250–7256, 2004.

[29] P. P. Freitas, F. A. Cardoso, V. C. Martins, S. A. M. Martins, J. Loureiro, J. Amaral, R. C. Chaves, S. Cardoso, L. P. Fonseca, A. M. Sebastião, M. Pannetier-Lecoeur, and C. Fermon, "Spintronic platforms for biomedical applications," *Lab Chip*, vol. 12, no. 3, pp. 546–557, 2012.

[30] http://www.doitpoms.ac.uk/tlplib/ferromagnetic/printall.php.

[31] Q. Ramadan and M. A. M. Gijs, "Simultaneous sample washing and concentration using a 'trapping-and-releasing' mechanism of magnetic beads on a microfluidic chip," *Analyst*, vol. 136, no. 6, p. 1157, 2011.

[32] S. P. Ravindranath, L. J. Mauer, C. Deb-Roy, and J. Irudayaraj, "Biofunctionalized magnetic nanoparticle integrated mid-infrared pathogen sensor for food matrixes," *Anal. Chem.*, vol. 81, no. 8, pp. 2840–2846, 2009.

[33] J. C. Rife, M. M. Miller, P. E. Sheehan, C. R. Tamanaha, M. Tondra, and L. J. Whitman, "Design and performance of GMR sensors for the detection of magnetic microbeads in biosensors," *Sensors Actuators, A Phys.*, vol. 107, no. 3, pp. 209–218, 2003.

[34] D. Huh, W. Gu, Y. Kamotani, J. B. Grotberg, and S. Takayama, "Microfluidics for flow cytometric analysis of cells and particles.," *Physiol. Meas.*, vol. 26, no. 3, pp. R73–R98, 2005.

[35] L. Draghiciu, M. Carp, L. Eftime, I. Stanciu, and R. Müller, “Manipulation of nanoparticles within a microfluidic system based on SU-8 polymer for bio-applications,” *Mater. Sci. Eng. B*, vol. 169, no. 1–3, pp. 186–192, 2010.

[36] B. Sinha, S. Anandakumar, S. Oh, and C. Kim, “Micro-magnetometry for susceptibility measurement of superparamagnetic single bead,” *Sensors Actuators, A Phys.*, vol. 182, pp. 34–40, 2012.

[37] R. Sista, “Development of a Digital Microfluidic Lab-on-a-Chip for Automated Immunoassay with Magnetically …,” *Etd.Lib.Fsu.Edu*, 2007.

[38] K. Smistrup, O. Hansen, H. Bruus, and M. F. Hansen, “Magnetic separation in microfluidic systems using microfabricated electromagnets—experiments and simulations,” *J. Magn. Magn. Mater.*, vol. 293, no. 1, pp. 597–604, 2005.

[39] C. L. Stoffel and K. L. Rowlen, “Data analysis for a dual-channel virus counter.,” *Anal. Chem.*, vol. 77, no. 7, pp. 2243–6, 2005.

[40] N. Yamaguchi, H. Ohba, and M. Nasu, “Simple detection of small amounts of Pseudomonas cells in milk by using a microfluidic device,” *Lett. Appl. Microbiol.*, vol. 43, no. 6, pp. 631–636, 2006.

[41] C. Zhao and X. Cheng, “Microfluidic separation of viruses from blood cells based on intrinsic transport processes.,” *Biomicrofluidics*, vol. 5, no. 3, pp. 32004–3200410, 2011.

[42] M. Mujika, S. Arana, E. Castaño, M. Tijero, R. Vilares, J. M. Ruano-López, a. Cruz, L. Sainz, and J. Berganza, “Magnetoresistive immunosensor for the detection of Escherichia coli O157:H7 including a microfluidic network,” *Biosens. Bioelectron.*, vol. 24, no. 5, pp. 1253–1258, 2009.

[43] A. Sandhu, H. Handa, and M. Abe, “Synthesis and applications of magnetic nanoparticles for biorecognition and point of care medical diagnostics,” vol. 442001.

[44] M. Tondra, M. Granger, R. Fuerst, M. Porter, C. Nordman, J. Taylor, and S. Akou, “Design of Integrated Microfluidic Device for Sorting Magnetic Beads in Biological Assays,” no. 1.

[45] E. Mirowski, J. Moreland, S. Russek, and M. Donahue, “Manipulation of magnetic particles by patterned arrays of magnetic spin-valve traps,” vol. 311, pp. 401–404, 2007.

[46] M. F. Cytometry, “Shapeable Magnetoelectronics in Research and Technology,” vol. 7436, no. 306277, pp. 1–2, 2013.

[47] S. S. Shevkoplyas, A. C. Siegel, R. M. Westervelt, G. Prentiss, and G. M. Whitesides, “The force acting on a superparamagnetic bead due to an applied magnetic field,” vol. 17, pp. 1294–1302, 2007.

[48] D. C. Jiles, “Recent advances and future directions in magnetic materials,” vol. 51, pp. 5907–5939, 2003.

[49] I. Transactions and O. N. Magnetics, “Hard Magnetic Materials : A Perspective Advances in Magnetics Hard Magnetic Materials : A Perspective,” no. DECEMBER 2011, 2015.

[50] M. Tijero, R. Vilares, J. M. Ruano-lópez, A. Cruz, L. Sainz, and J. Berganza, “Biosensors and Bioelectronics Magnetoresistive immunosensor for the detection of Escherichia coli O157 : H7 including a microfluidic network,” vol. 24, pp. 1253–1258, 2009.

[51] P. Poulichet, A. Fakri, and B. D. B. Pascal, “Simulation and optimisation of homogeneous permanent magnet for portable NMR applications,” pp. 2–4, 2014.

[52] A. E. Marble, I. V Mastikhin, B. G. Colpitts, and B. J. Balcom, “A compact permanent magnet array with a remote homogeneous field,” vol. 186, pp. 100–104, 2007.

[53] B. Manz, M. Benecke, and F. Volke, “A simple , small and low cost permanent magnet design to produce homogeneous magnetic fields,” vol. 192, pp. 131–138, 2008.

[54] C. Liu, T. Stakenborg, S. Peeters, L. Lagae, C. Liu, T. Stakenborg, S. Peeters, and L. Lagae, “Cell manipulation with magnetic particles toward microfluidic cytometry Cell manipulation with magnetic particles toward microfluidic cytometry,” vol. 102014, no. 2009, 2014.

[55] I. K. Schuller, “Exchange bias,” vol. 192, 1999.

[56] W. Ku, F. Silva, J. Bernardo, P. P. Freitas, W. Ku, F. Silva, J. Bernardo, and P. P. Freitas, “Integrated giant magnetoresistance bridge sensors with transverse permanent magnet biasing Integrated giant magnetoresistance bridge sensors with transverse permanent magnet biasing,” vol. 5353, no. 2000, pp. 2–5, 2005.

[57] C. H. Smith, R. W. Schneider, and N. Electronics, “Low-Field Magnetic Sensing with GMR Sensors,” 1999.

[58] M. A. M. Gijs, “Magnetic bead handling on-chip : new opportunities for analytical applications,” pp. 22–40, 2004.

[59] F. Fahrni, M. W. J. Prins, and L. J. van IJzendoorn, “Magnetization and actuation of polymeric microstructures with magnetic nanoparticles for application in microfluidics,” *J. Magn. Magn. Mater.*, vol. 321, pp. 1843–1850, 2009.

[60] L. J. Whitman, “Magnetic labeling , detection , and system integration,” no. OCTOBER 2008, 2015.

[62] Y. Ding, J. H. Judy, and J. Wang, “Magnetoresistive sensors with perpendicular magnetic anisotropy,” vol. 704, no. 2005, pp. 1–4, 2008.

[63] J. Of and M. Materials, “Permanent Magnet Applications,” vol. 8853, no. AUGUST 2002, 2015.

[64] A. Manuscript, “NIH Public Access,” vol. 126, no. 1, pp. 98–106, 2008.

[65] K. C. Cheung, M. Di Berardino, G. Schade-Kampmann, M. Hebeisen, A. Pierzchalski, J. Bocsi, A. Mittag, and A. Tárnok, “Microfluidic impedance-based flow cytometry,” *Cytom. Part A*, vol. 77A, no. 7, pp. 648–666, 2010.

[66] S.-C. Lin, P.-W. Yen, C.-C. Peng, and Y.-C. Tung, “Single channel layer, single sheath-flow inlet microfluidic flow cytometer with three-dimensional hydrodynamic focusing,” Lab Chip, vol. 12, no. 17, p. 3135, 2012.

[67] O. Hofmann, P. Niedermann, and a Manz, “Modular approach to fabrication of three-dimensional microchannel systems in PDMS-application to sheath flow microchips.,” *Lab Chip*, vol. 1, pp. 108–114, 2001.

[68] P. P. Freitas, F. Silva, N. J. Oliveira, L. V. Melo, L. Costa, and N. Almeida, “Spin valve sensors,” Sensors Actuators, A Phys., vol. 81, no. 1, pp. 2–8, 2000.

[69] M. Megens and M. Prins, “Magnetic biochips: A new option for sensitive diagnostics,” *J. Magn. Magn. Mater.*, vol. 293, no. 1, pp. 702–708, 2005.

[70] H. a. Ferreira, D. L. Graham, P. P. Freitas, and J. M. S. Cabral, “Biodetection using magnetically labeled biomolecules and arrays of spin valve sensors (invited),” *J. Appl. Phys.*, vol. 93, no. 10 2, pp. 7281–7286, 2003.

[71] Y. Amemiya, T. Tanaka, B. Yoza, and T. Matsunaga, “Novel detection system for biomolecules using nano-sized bacterial magnetic

[73] https://pt.wikipedia.org/wiki/Sensor_de_efeito_Hall

[74] G. Guidelines, P. Contents, R. Materials, and P. Description, “Dynabeads M-280 Streptavidin.”

[75] D. J. B. Bechstein, J.-R. Lee, C. C. Ooi, A. W. Gani, K. Kim, R. J. Wilson, and S. X. Wang, “High performance wash-free magnetic bioassays through microfluidically enhanced particle specificity,” *Sci. Rep.*, vol. 5, no. February, p. 11693, 2015.

[76] A. Mortari and L. Lorenzelli, “Recent sensing technologies for pathogen detection in milk: A review,” *Biosens. Bioelectron.*, vol. 60, pp. 8–21, 2014.

[77] R. S. Lakshmanan, R. Guntupalli, J. Hu, V. A. Petrenko, J. M. Barbaree, and B. A. Chin, “Detection of Salmonella typhimurium in fat free milk using a phage immobilized magnetoelastic sensor,” *Sensors Actuators B Chem.*, vol. 126, no. 2, pp. 544–550, 2007.

[78] B. D. Piorek, S. J. Lee, J. G. Santiago, M. Moskovits, S. Banerjee, and C. D. Meinhart, “Free-surface microfluidic control of surface-enhanced Raman spectroscopy for the optimized detection of airborne molecules.,” *Proc. Natl. Acad. Sci. U. S. A.*, vol. 104, no. 48, pp. 18898–18901, 2007.

APPENDIX

A. Run Sheet: Magnetic Counter

Sample ID: # 36SV175

Process start: 20.04.2015 Process end: 15.05.2015

Step 1: Deposition of Alumina (Al_2O_3)

Date: xxx	Operator: Susana Cardoso

Substrate: Silicon (Si) substrate

Equipment: UHVII

Expected thickness: 1000 Å

Deposition conditions:

Deposition of Al2O3 layer of around 1000 Å thickness is accomplished on the UHVII, an oxide sputtering system. This prevents current leakage from the device, as Si wafer is a semi-conductor.

Base pressure (Pa)	Power (W)	Pressure (mTorr)	Ar Flux (sccm)	Rate (nm/min)
3x10-7	200 (RF)	1,2	45	1,3

Step 2: Spin-valve deposition

Date: xxx	Operator: Susana Cardoso

Substrate: Si substrate with 1000 Å of Al2O3

Equipment: Nordiko 3000 Ion beam deposition and milling system.

SV structure:

Ta 15 / NiFe 25 / CoFe 20 / Cu 21 / CoFe 20 / MnIr 60 / Ta 20 (Å)

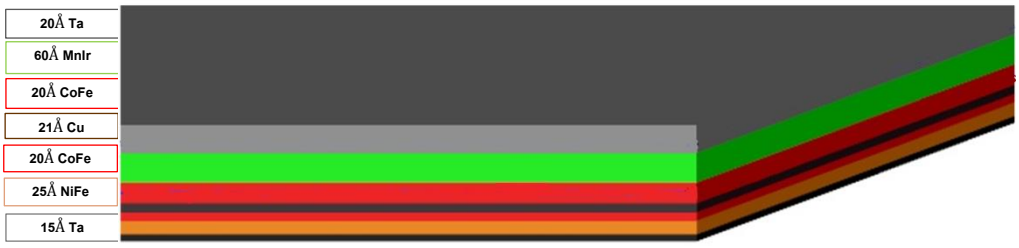

Figure A92 Spin Valve layers.

Expected thickness: 293 Å

Deposition conditions:

Power	Xe Flux (sccm)	Table	Magnetic field (mT)
150W (RF); +1200V/-275V; 171mA	4	80° pan; 30 rpm	3

Magnetic anisotropy axis of the pinned and the free layer defined by a magnetic field of 40 Oe during the deposition

Electric transport characterization of the unpatterned sample
Measured parameters: [-140 Oe, 140 Oe]

MR (%)	Hf (Oe)	Hc (Oe)
9,17	17	2,85

Step 3: SV sensors definition

Date: 20.04.2015	Operator: Engº José Bernardo / Ana Rita

Substrate: Si substrate with 1000 Å of Al2O3 and passivated SV
Equipment: DWL 2.0

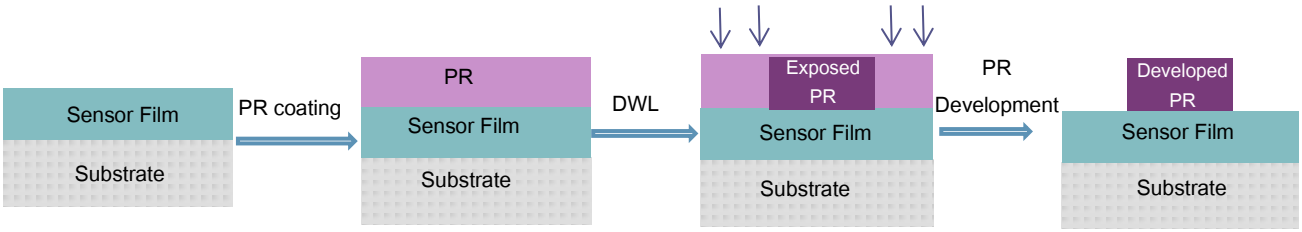

Figure A93 Overall Process of the third step.

Pre-treatment:

i. Vapor Prime for 30 minutes of an organic compound (Hexamethyldisilane, C6H18Si2) onto the substrate under a temperature of 130 ºC, in vacuum- This step promotes the PR coating adhesion. [Program 0]

Step description	Conditions (Program 0)
Wafer dehydration	Vacuum, 10 Torr, 2 min. N2 inlet, 760 Torr, 3 min. Heating to 130ºC
Priming	Vacuum, 1 Torr, 3 min. HDMS, 6 Torr, 5 min.
Purge prime exhaust	Vacuum, 4 Torr, 1 min.

	N2 inlet, 500 Torr, 2 min. Vacuum, 4 Torr, 2 min.
Return to atmosphere	N2 inlet, 3 min.

ii. Coating of 1.5 µm thickness of positive photoresist (PFR7790G27cP - JSR Electronics) cover the sample. [Program 6 / 2].

Coating Parameters	
First Step	Dispense photoresist on the sample and spinning at 800 rpm for 5 sec.
Second step	Spin at 2500 rpm for 30 sec. to obtain ~1.45 µm thickness.
Third step	Soft bake at 85ºC for 60 seconds.

Exposure conditions:

During the exposure, the laser in the DWL sweeps the sample according to the designed mask, scanning the ample in stripes of 200 µm wide composed of a pixel grid of 200 nm.

Map: CIT_IN
Mask name: h3\inesccitL1
Die dimensions: [x: 20900 µm y: 19000 µm]
Alignment marks:
[x: 162.06 , Y: 570.42 ; x: 18830.06 , y: 570.42]
Power: 100 mW
Focus: -20; Energy: 55

Mask:

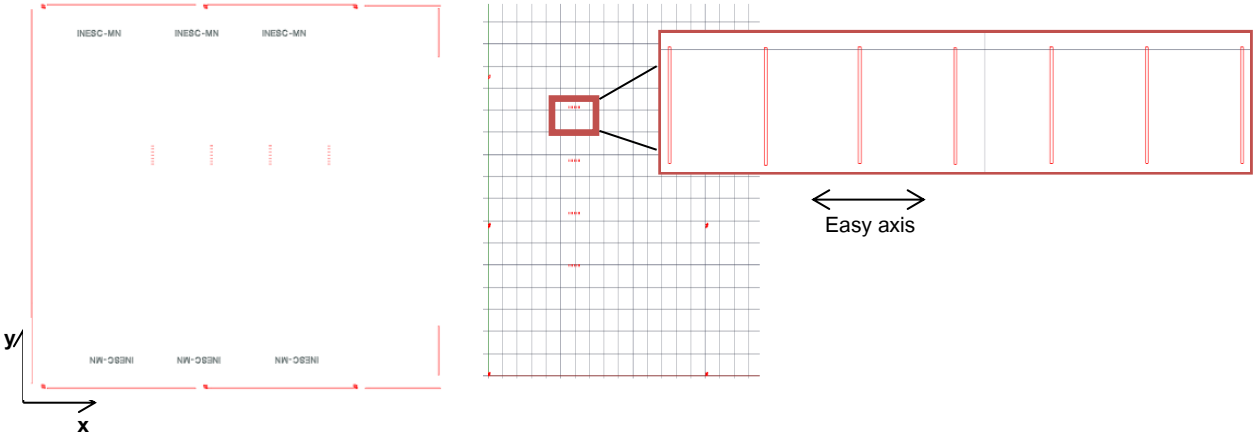

Figure A94 AutoCad® Mask for first lithography: sensor's definition. Chip with array of 28 SVs in red displayed vertically in the centre of the chip.

Development conditions:

The sample is baked at 110 °C for 1min, followed by cooling for 30 s and then development during 1min. [Program 6 / 2]

Development parameters:
Bake at 110°C for 60s
Cool for 30s
Developer for 60s

Optical Inspection:

Verification under microscope of the sample showed the correct coating, exposure and development.

Step 4: Spin Valve Etch

Date: 21.04.2015	Operator: Engº José Amaral

Substrate: Si substrate with 1000 Å of Al2O3 and passivated SV
Equipment: Nordiko 3600 Ion beam deposition and milling system

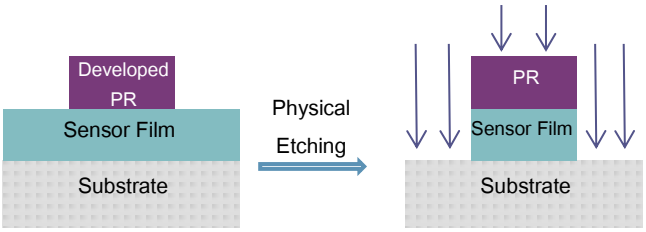

Figure A95 Schematics of physical etching.

Total thickness to etch: 345 Å
Etch rate: ~ 1 Å/s ⟹ Required time: 400 s

Etching conditions:

Assist Gun	Power (W)	V+ (V)	I+ (mA)	V- (V)	I- (mA)	Ar Flux (sccm)	Pan (deg)	Rotation
Read Values	195	724	105	345	2.9	10.2	60º	30 rpm

Step 5: Resist stripping

Date: 21.04.15	Operator: Rita Soares

Equipment: Wet bench

Conditions:

The removal of PR was done with Microstrip® at 65ºC and exposed to ultrasounds. Then the sample was rinsed with IPA, water and dried with a compressed air gun.

Started: 17h (21.04.15) Stopped: 10h (22.04.15)

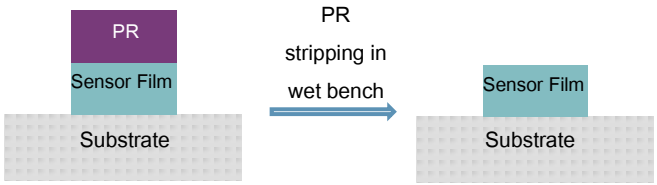

Figure A96 Schematics of resist stripping.

Observations:

Verification under the microscope of the sample showed that the etched resist was removed

---

Step 6: Contacts definition

Date: 22.04.15	Operator: Eng. Bernardo

Equipment: DWL 2.0

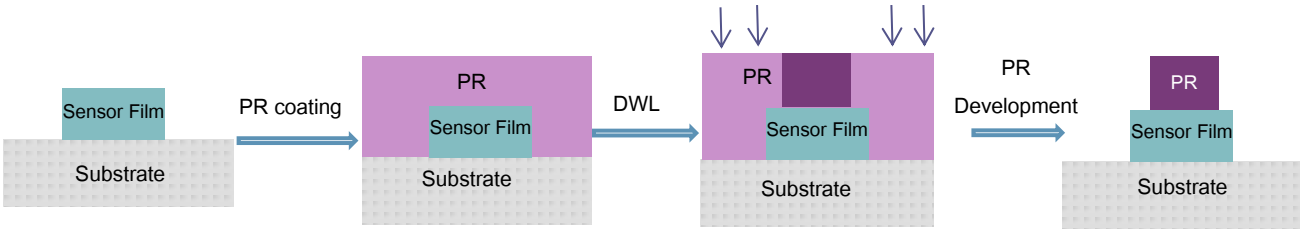

Figure A97 Second lithography process.

Pre-treatment:

i. Vapor Prime for 30 minutes of an organic compound (Hexamethyldisilane, C6H18Si2) onto the substrate under a temperature of 130 ºC, in vacuum- This step promotes the PR coating adhesion. [Program 0]

Step description	Conditions (Program 0)
Wafer dehydration	Vacuum, 10 Torr, 2 min. N2 inlet, 760 Torr, 3 min.

	Heating to 130ºC
Priming	Vacuum, 1 Torr, 3 min. HDMS, 6 Torr, 5 min.
Purge prime exhaust	Vacuum, 4 Torr, 1 min. N2 inlet, 500 Torr, 2 min. Vacuum, 4 Torr, 2 min.
Return to atmosphere	N2 inlet, 3 min.

ii. Coating of 1.5 µm thickness of positive photoresist (PFR7790G27cP - JSR Electronics) cover the sample. [Program 6 / 2].

Coating Parameters	
First Step	Dispense photoresist on the sample and spinning at 800 rpm for 5 sec.
Second step	Spin at 2500 rpm for 30 sec. to obtain ~1.45 µm thickness.
Third step	Soft bake at 85ºC for 60 seconds.

Exposure conditions:

A correct alignment of the substrate in the DWL is required, thus alignment marks on the design of the chip were imprinted on the sample in Step 2. These alignment marks are detected in the DWL system with a CCD camera system.

Map: CIT_IN
Mask name: h3\inesccitL2
Mask: non-inverted
Die dimensions: [x: 20900 µm y: 19000 µm]
Power: 120 mW; Focus: -20; Energy: 55

Alignment marks:

[X: 162.06 , Y: 570.42 ; X: 18830.06 , Y: 570.42]

Mask:

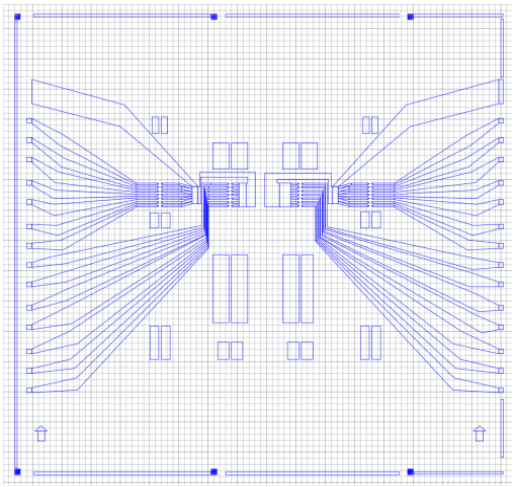

Figure A98 AutoCad® mask for second lithography: contact leads definition. The contact leads are presented in blue.

Development conditions:

The sample is baked at 110 °C for 1min, followed by cooling for 30 s and then development during 1min. [Program 6 / 2]

Development parameters:
Bake at 110°C for 60s
Cool for 30s
Developer for 60s

Optical Inspection:

Verification under microscope of the sample showed some dies were not completely developed, thus required an extra time of development (15 s)

Step 7: Deposition of Aluminium (3000 Å)

Date: 06.11.14	Operator: Engº João Valadeiro

Equipment: Nordiko 7000 magnetron sputtering system
Expected thickness: 3000 Å (Al) + 150 Å ($TiWN_2$)

Conditions:

Program: Seq.Metalization

Mod2 F9 *soft etch* 1'; P: RF1: 60W, RF2: 40W; p=3mTorr; 50 sccm Ar
Mod4 F1 *metalization* [3000 Å (Al)] 1'20''; P=2 kW; p= 3mTorr; 50 sccm Ar
Mod 3 F19 *passivation* [150 Å (TiW)] 27''; P=0.5 kW; p= 3mTorr; 50sccm Ar + 10 sccm N_2

Readings – Module 2				
Power1	**Power2**	**Gas flux**	**Pressure**	
60 W	39 W	50.0 sccm	3 mT	
Readings – Module 4				
Power	**Voltage**	**Current**	**Gas flux**	**Pressure**
2 KW	396 V	5.12 A	50.0 sccm	3 mT
Readings – Module 3				
Power	**Voltage**	**Current**	**Gas flux**	**Pressure**
0.50 KW	423 V	1 A	49.955 sccm Ar 9.6 sccm N_2	3.0 mT

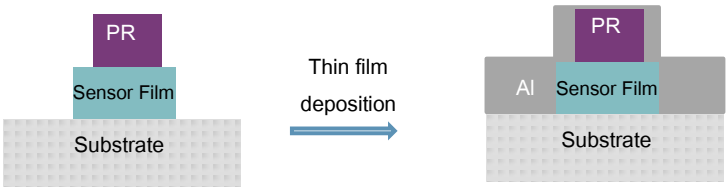

Figure A99 Schematics of Thin film deposition process.

Step 8: Lift-off of Aluminium

Date: 23.04.15	Operator: Rita Soares

Equipment: *Wet bench*

Conditions:

The removal of PR was done with Microstrip® at 65ºC and exposed to ultrasounds. Then the sample was rinsed with IPA, water and dried with a compressed air gun.

Started: 12h Stopped: 19h

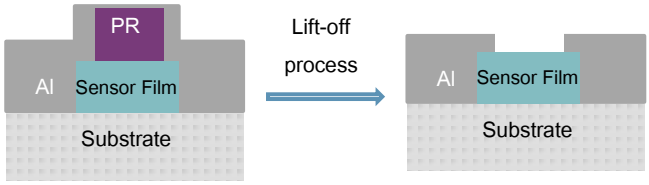

Figure A100 Photoresist and metal litf-off process.

Observations:

Verification under microscope showed a correct alignment of the mask and a clean lift-off process.

Step9: Deposition of Alumina (Si_3N_4)

Date: 11.05.15	Operator: Engº Fernando Silva

Equipment: Electrotech Delta Chemical Vapor Deposition System
Expected thickness: 3000 Å
Time: 1min e 14 s

Deposition conditions:

Deposition time (s)	Power Source RF (W)	Pressure (mTorr)	SiH_4 gas flux (sccm)	NH_3 gas flux (sccm)	N_2 gas flux (sccm)	Rate (Å/s)
1 min	502	848	298	496	3460	50

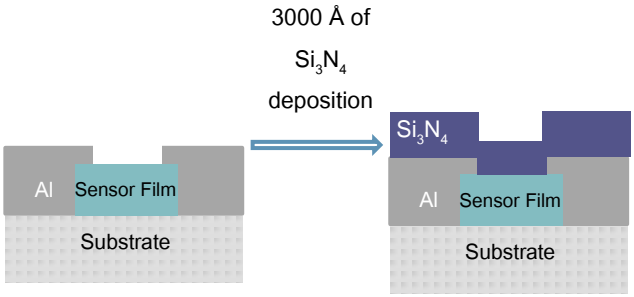

Figure A101 Schematics of Si_3N_4 deposition: passivation layer.

Step 10: Contact leads frame definition

Date: 11.05.15	Operator: Engº Bernardo

Equipment: DWL 2.0

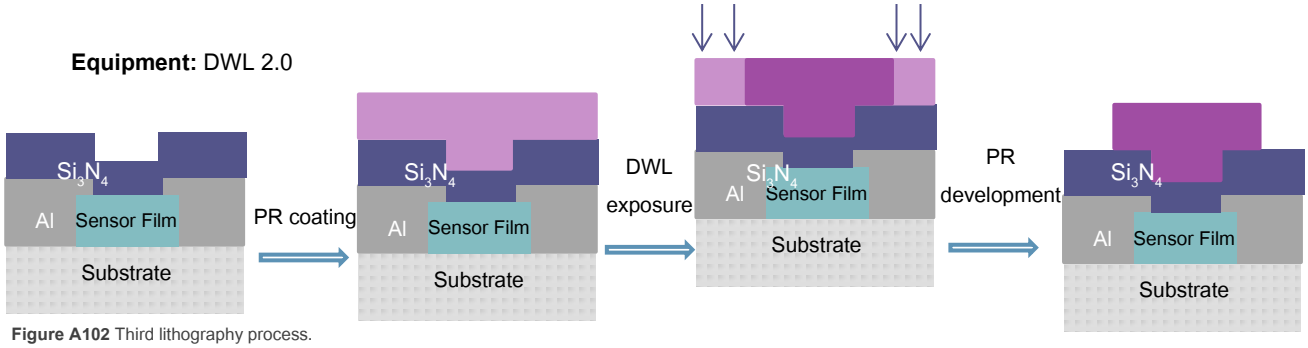

Figure A102 Third lithography process.

Pre-treatment:

i. Vapor Prime for 30 minutes of an organic compound (Hexamethyldisilane, C6H18Si2) onto the substrate under a temperature of 130 ºC, in vacuum- This step promotes the PR coating adhesion. [Program 0]

Step description	Conditions (Program 0)
Wafer dehydration	Vacuum, 10 Torr, 2 min. N2 inlet, 760 Torr, 3 min. Heating to 130ºC
Priming	Vacuum, 1 Torr, 3 min. HDMS, 6 Torr, 5 min.
Purge prime exhaust	Vacuum, 4 Torr, 1 min. N2 inlet, 500 Torr, 2 min. Vacuum, 4 Torr, 2 min.
Return to atmosphere	N2 inlet, 3 min.

ii. Coating of 1.5 µm thickness of positive photoresist (PFR7790G27cP - JSR Electronics) cover the sample. [Program 6 / 2].

Coating Parameters	
First Step	Dispense photoresist on the sample and

	spinning at 800 rpm for 5 sec.
Second step	Spin at 2500 rpm for 30 sec. to obtain ~1.45 µm thickness.
Third step	Soft bake at 85ºC for 60 seconds.

Exposure conditions:

Map: CIT_IN
Mask name: h3\inesccitL3
Mask: non-inverted
Die dimensions: [x: 20900 µm y: 19000 µm]
Power: 100 mW; Focus: -20; Energy: 55

Alignment marks:
[X: 162.00 , Y: 54.00 ; X: 18838.00 , Y: 54.00]

Mask:

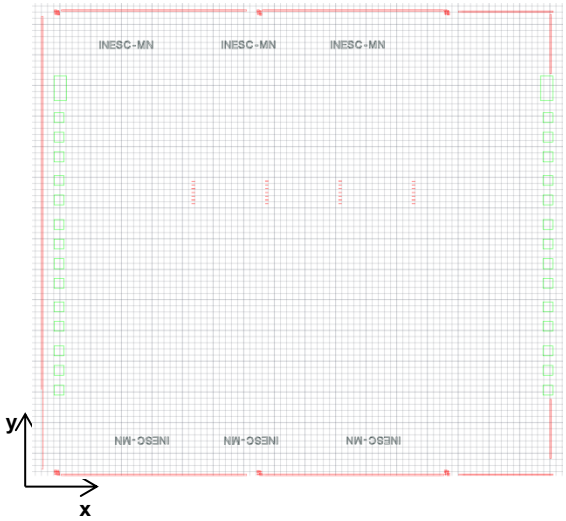

Figure A103 Design AutoCad® of the chip with the SV displayed in red. The frame for electrical contact at the end of each contact lead is displayed in green.

Development conditions:

The sample is baked at 110 °C for 1min, followed by cooling for 30 s and then development during 1min. [Program 6 / 2]

Development parameters:
Bake at 110°C for 60s
Cool for 30s

Developer for 60s

Observations:

Verification under microscope of the sample showed correct coating, exposure and development.

Step 11: Reactive ion etching – pads opening

Date: 13.05.2015	Operator: Engª Virgínia Soares

Pre-treatment:

- PR coating [program 6 / 29 for wafer protection

Equipment: LAM Rainbow Plasma Etcher 4520
Process recipe: Low power - no O_2
Thickness to etch: 3000 Å
Etch rate: ~ 10-13 Å/s

Etching conditions:

Pressure (Torr)	Etch time (s)	Power (RF)	Ar Flux (sccm)	CF_4 Flux (sccm)	O_2 (sccm)
140.2 mTorr	-3x150 s *-over-etch*: 100s	100 W	200	100	0

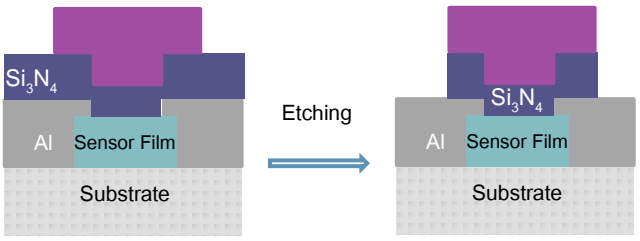

Figure A104 Schematics of reactive ion etching for pads opening.

Observations: To confirm spin-valve etch is complete measure the resistance of the sample; if the resistance is low etch is not complete.

Step 12: Wafer Dicing

Date: 14.05.2015	Operator: Engª Virgínia Soares

Equipment: Disco DAD 321
Die dimensions: x: 209000 µm ; y: 19000 µm

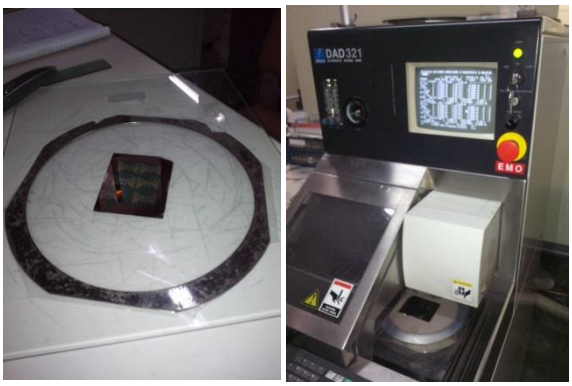

Figure A105 Sample was cut into individual dies.

When the dicing process finish, the sample is places under UV exposure during 2 min to help film “Adwlle tape” glue to melt and allow dies to be removed.

Step 13: *Resist stripping*

Date: 14.05.2015	Operator: Rita Soares

Equipment: Wet bench

Conditions: The removal of PR was done with Microstrip® at 65ºC and exposed to ultrasounds. Then the sample was rinsed with IPA, water and dried with a compressed air gun.

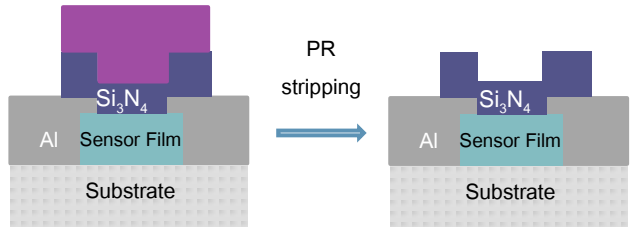

Figure A106 Resist stripping.

Step 14: Annealing

Date: 15.05.2015	Operator: Rita Soares

Equipment: 21100 Tube Furnace (BL Barnstead Thermolyne)

Annealing conditions:

Step 13.1: The dies are inserted in a vacuum chamber.

Step 13.2: Heating the dies until reach 250°C and then leave it for 15min at this temperature.

Step 13.3: Dies cooling down until room temperature, in the presence of 1T magnetic field aligned with the easy axis of the pinned layer.

B. Run Sheet: PDMS Microchannels

Sample ID: # 36SV175
Process start: 20.04.2015 Process end: 15.05.2015

Step 1: PDMS mixture

Date: -	Operator: Ana Rita Soares

Conditions:

Step 1.1: Mix PDMS and currant agent in 10:1 weight ratio and mix well
Step 1.2: Degass for 1h, using the excicator

Step 2: PDMS casting

Date: -	Operator: Ana Rita Soares

Conditions:

Step 2.1: Place the mold in the respective PMMA holders
Step 2.2: Hold the PMMA plates together using strong springs. The plates are presses against the mold and between each other, in order to avoid PDMS leaks.
Step 2.3: Inject the PDMS through the PMMA holes using a Luer Lock syringe and a blunt needle.
Step 2.4: Cure the mixture inside the oven for 1h at 70ºC.
Step 2.5: Wait ~ 15min before removing the PDMS from the mold.

Observations: Check the channels with the microscope.

C. Run Sheet: PDMS permanent bonding

Process start: - Process end: -

Step 1: **PDMS and Chips cleaning**

Date: -	Operator: Ana Rita Soares

Substrate: Chip and PDMS

Equipment:

Conditions: Wash the units with IPA and rinse with deionized water and dry with nitrogen.

Step 2: **Ultraviolet / Ozone (UVO)**

Date: -	Operator: Ana Rita Soares

Substrate: Chip and PDMS

Equipment: UVO Cleaner (Model 144AX-220, Jelight Company, Inc.)

Conditions:

Plasma	Time
28mW/cm^2	10 min + 5 min exhaustion step

Observations: Immerse the PDMS bonded with chip in water after this process.

Step 3: Alignment

Date: -	Operator: Ana Rita Soares

Substrate: Chip and PDMS

Equipment: Microchannels aligner

Conditions:

Step 3.1: Fix the chip to micropositioner and then place the PDMS on top of it.
Step 3.2: Add ethanol on the surfaces, during the alignment, enabling them to slip relatively each other and to maintain the activation as long as possible.
Step 3.3 Leave it to dry overnight.

Observations: Process is made under the microscope (160x amplification).

Step 4: Wirebonding

Date: -	Operator: Ana Rita Soares

Substrate: Chip and PDMS

Conditions:

Step 4.1: Drill holes in the PCB
Step 4.2: Glue the die on a PCB.
Step 4.3: Mount the die (chip and microfluidics) on a PCB by wirebonding
Step 4.5: Wirebonding is covered with silicon gel.